

Award Number: W81XWH-11-1-0100

TITLE: Modeling the Anisotropic Resolution and Noise Properties of Digital Breast Tomosynthesis Image Reconstructions

PRINCIPAL INVESTIGATOR: Raymond J. Acciavatti, B.S.

CONTRACTING ORGANIZATION: University of Pennsylvania  
Philadelphia, PA 19104

REPORT DATE: January 2012

TYPE OF REPORT: Annual Summary

PREPARED FOR: U.S. Army Medical Research and Materiel Command  
Fort Detrick, Maryland 21702-5012

DISTRIBUTION STATEMENT: Approved for Public Release;  
Distribution Unlimited

The views, opinions and/or findings contained in this report are those of the author(s) and should not be construed as an official Department of the Army position, policy or decision unless so designated by other documentation.

REPORT DOCUMENTATION PAGE				Form Approved OMB No. 0704-0188	
Public reporting burden for this collection of information is estimated to average 1 hour per response, including the time for reviewing instructions, searching existing data sources, gathering and maintaining the data needed, and completing and reviewing this collection of information. Send comments regarding this burden estimate or any other aspect of this collection of information, including suggestions for reducing this burden to Department of Defense, Washington Headquarters Services, Directorate for Information Operations and Reports (0704-0188), 1215 Jefferson Davis Highway, Suite 1204, Arlington, VA 22202-4302. Respondents should be aware that notwithstanding any other provision of law, no person shall be subject to any penalty for failing to comply with a collection of information if it does not display a currently valid OMB control number. <b>PLEASE DO NOT RETURN YOUR FORM TO THE ABOVE ADDRESS.</b>					
1. REPORT DATE January 2012		2. REPORT TYPE Annual Summary		3. DATES COVERED 1 January 2011 – 31 December 2011	
4. TITLE AND SUBTITLE  Modeling the Anisotropic Resolution and Noise Properties of Digital Breast Tomosynthesis Image Reconstructions				5a. CONTRACT NUMBER	
				5b. GRANT NUMBER W81XWH-11-1-0100	
				5c. PROGRAM ELEMENT NUMBER	
6. AUTHOR(S)  Raymond J. Acciavatti  E-Mail: racc@seas.upenn.edu				5d. PROJECT NUMBER	
				5e. TASK NUMBER	
				5f. WORK UNIT NUMBER	
7. PERFORMING ORGANIZATION NAME(S) AND ADDRESS(ES)  University of Pennsylvania Philadelphia, PA 19104				8. PERFORMING ORGANIZATION REPORT NUMBER	
9. SPONSORING / MONITORING AGENCY NAME(S) AND ADDRESS(ES) U.S. Army Medical Research and Materiel Command Fort Detrick, Maryland 21702-5012				10. SPONSOR/MONITOR'S ACRONYM(S)	
				11. SPONSOR/MONITOR'S REPORT NUMBER(S)	
12. DISTRIBUTION / AVAILABILITY STATEMENT Approved for Public Release; Distribution Unlimited					
13. SUPPLEMENTARY NOTES					
14. ABSTRACT In tomosynthesis, a 3D image of the breast is generated from multiple x-ray projections. Although prior authors have modeled image quality in tomosynthesis, their work is limited in approximating the incident angle as normal to the detector. This research studies the consequences of carefully modeling the incident angle. From first principles, an analytical model of the transfer functions for oblique incidence is derived in individual projections. The anisotropy of the transfer functions over the detector area is then demonstrated, and a technique for optimizing detector thickness at various incident angles is developed. In addition to modeling the effect of non-normal incidence on transfer functions, it is shown that oblique incidence yields sub-pixel translational shifts in the image of the object with each projection angle. By calculating the reconstruction of a high frequency sine input, the potential for super-resolution (i.e., sub-pixel resolution) is established from this property. Super-resolution is demonstrated in experimental images of bar patterns and select clinical examples of microcalcifications. The feasibility of super-resolution is also verified in a broad range of multi-planar reconstructions. Finally, from the analytical modeling of the sine input, the scan time which optimizes modulation in the reconstruction is calculated in systems with patient motion.					
15. SUBJECT TERMS Digital breast tomosynthesis (DBT), oblique x-ray incidence, phosphor, modulation transfer function (MTF), detective quantum efficiency (DQE), super-resolution, aliasing, image reconstruction, bar pattern phantom, microcalcification, patient motion, continuous tube motion, step-and-shoot motion, optimization.					
16. SECURITY CLASSIFICATION OF:			17. LIMITATION OF ABSTRACT	18. NUMBER OF PAGES	19a. NAME OF RESPONSIBLE PERSON
a. REPORT	b. ABSTRACT	c. THIS PAGE			USAMRMC
U	U	U	UU	41	19b. TELEPHONE NUMBER (include area code)

## Table of Contents

	<u>Page</u>
Introduction .....	5
Body .....	5
Key Research Accomplishments .....	9
Reportable Outcomes .....	10
Conclusion .....	10
References .....	11
Appendices.....	13

## I. INTRODUCTION

Digital breast tomosynthesis (DBT) is a 3D imaging modality in which tomographic sections of the breast are generated from a limited range of x-ray projections. Preliminary studies have indicated that DBT has improved sensitivity and specificity for early cancer detection relative to conventional 2D digital mammography (DM).<sup>1, 2</sup> In my dissertation research in Dr. Andrew Maidment's lab at the University of Pennsylvania, I have worked to develop analytical models of the transfer functions of DBT for assessment of image quality. Although the transfer functions of DBT have been modeled by other researchers, their approach is limited by approximating the angle of incidence as normal to the detector at all points in the projection images.<sup>3</sup> In modeling the anisotropy of the incident angle at each point of the detector, I have developed rigorous models of image quality in DBT that would not be possible under the formulation of previous authors.

## II. BODY

### II. A. Resolution Loss Due to Oblique X-Ray Incidence

In the winter and early spring of 2011, much of my research effort was devoted to writing a peer-reviewed publication analyzing the effect of oblique x-ray incidence on the resolution and noise properties of projection images in DBT. It ultimately felt rewarding to see this work published in the November 2011 issue of the journal *Medical Physics*.<sup>4</sup>

In my *Medical Physics* publication, I have extended Swank's calculations of the transfer functions of turbid granular phosphors<sup>5</sup> to oblique x-ray incidence using the diffusion equation<sup>6</sup> to model the spread of visible light in a scintillator. My work successfully demonstrated degradation in the modulation transfer function (MTF) and detective quantum efficiency (DQE) with oblique x-ray incidence. The model is set apart from prior studies<sup>7-9</sup> on oblique x-ray incidence in being derived from first principles and in closed form without making the simplifying assumption that the point spread function (PSF) of normal incidence is a delta function.<sup>10</sup>

In the first specific aim (SA1) of my predoctoral training grant through the Department of Defense (DOD) Breast Cancer Research Program, I proposed to demonstrate the spatial anisotropy of the transfer functions of DBT by carefully modeling the incident angle at each point on the detector. To illustrate the anisotropy of one of the transfer functions in an individual projection, DQE was plotted versus position on the detector at a fixed spatial frequency in my *Medical Physics* publication (Figure 7, p. 6195).<sup>4</sup> I showed that an oblique projection has greater spatial variation in DQE than the central projection.

In addition, in SA2 of my predoctoral DOD grant, I proposed to investigate strategies for optimization of image quality in DBT. One important result published in my *Medical Physics* paper was the calculation of the projection angle dependence of the optimal phosphor thickness which maximizes DQE (Figures 8-9, p. 6196).<sup>4</sup> My work demonstrated that the optimal phosphor thickness is projection angle dependent, favoring smaller thicknesses with higher incident angles.

### II. B. Super-Resolution in DBT Image Reconstructions

Throughout the past year, I have also pursued a project investigating the existence of super-resolution in DBT. A full draft of a paper on super-resolution will soon be sent to the journal *Medical Physics* for consideration as a peer-reviewed research publication.<sup>11</sup> This work expands upon a proceedings manuscript presented in the 2011 Physics of Medical Imaging Conference of the Society of Photo-optical Instrumentation Engineers (SPIE).<sup>12</sup> The proceedings manuscript, which was supported by a different funding mechanism than my predoctoral DOD grant, earned the Best Student Paper Award at the conference in February of 2011 in Lake

Buena Vista, Florida. My award ultimately received coverage in an article written in March of 2011 on the website [medicalphysicsweb.org](http://medicalphysicsweb.org).<sup>13</sup>

In DBT, the image of an object is translated in sub-pixel detector element increments with each increasing projection angle. To my knowledge, my work is the first to demonstrate the potential for super-resolution (*i.e.*, sub-pixel resolution) in DBT reconstructions as a result of this property. In order to develop an analytical model of super-resolution, I calculate the reconstruction of a thin input object whose attenuation coefficient varies sinusoidally with position within a rectangular prism parallel to the breast support. This input object is termed a “sine plate” in my manuscript submission for the journal *Medical Physics*.<sup>11</sup> To investigate super-resolution, the frequency of the sinusoidal attenuation coefficient is specified to be higher than the alias frequency of the detector. Using analytical modeling, I demonstrate that the central projection represents this high frequency input as if it were a lower frequency, and that its Fourier transform is maximized at a lower frequency than the input as evidence of aliasing. By contrast, the high frequency input can be resolved by performing a simple backprojection (SBP) reconstruction on a grid whose pixel size is much smaller than that of the detector elements. Applying filters to the reconstruction smoothens pixilation artifacts in the spatial domain and reduces spectral leakage in the Fourier domain.

My analytical model of super-resolution illustrates the importance of carefully calculating the incident angle at each point on the detector as proposed in my DOD predoctoral grant. In order to determine the sub-pixel shifts in the image of the sine plate between projections, it is necessary to model the spatial anisotropy of the incident angle on the detector. Because prior authors have approximated the incident angle as normal to the detector in all projections,<sup>3</sup> they are unable to derive the sub-pixel shifts in the image of the object between projections, and hence are not able to model the presence of super-resolution in the reconstruction.

Using a bar pattern phantom, the existence of super-resolution in DBT was verified experimentally. Individual projections of the bar pattern phantom exhibited classical signs of aliasing,<sup>14</sup> such as representing high frequency patterns at an erroneous orientation with less line pairs than expected. By contrast, bar patterns with frequencies higher than the alias frequency of the detector were successfully resolved in reconstructions performed on very fine grids. In select clinical examples, super-resolution was found to improve the visibility of microcalcifications, which are subtle signs of breast cancer in many women.<sup>15</sup> By reconstructing on grids whose pixel sizes are much smaller than the detector elements, the morphology of the calcifications was seen more clearly, and small calcifications that would not otherwise be visible became apparent due to super-resolution. For these reasons, super-resolution satisfies a central goal in SA2 of my predoctoral DOD grant, which was to develop techniques to improve image quality.

Finally, my research has demonstrated spatial anisotropies in the existence of super-resolution depending upon the directionality of the input frequency. Although super-resolution is achievable over a broad range of positions for an input frequency parallel to the chest wall side of the breast support, super-resolution is feasible at fewer positions for an input frequency perpendicular to the chest wall. Super-resolution along the latter directionality is achievable only at positions sufficiently displaced from the plane of the chest wall and from the mid plane perpendicular to the breast support and to the chest wall. The anisotropy of super-resolution has been demonstrated analytically from the calculation of the reconstruction of a sine plate, as well as experimentally from the reconstruction of bar patterns. This finding complements the central aim of SA1 in my predoctoral DOD grant, which was to demonstrate spatial anisotropy in the image quality of DBT systems.

## **II. C. Oblique Reconstructions in DBT**

My research on super-resolution initially assumed a reconstruction plane parallel to the breast support. In a subsequent study, I demonstrated that super-resolution is also achievable in an obliquely pitched reconstruction plane. This work was accepted for oral presentation at the Annual Meeting of the American Association of Physicists in Medicine (AAPM) in Vancouver, British Columbia on August 2, 2011.<sup>16</sup> In

addition, similar work was accepted as a poster presentation<sup>17</sup> at the Era of Hope conference in Orlando, Florida from August 2, 2011 to August 5, 2011. Because the Era of Hope conference presented a conflict with the Annual AAPM Meeting, my graduate supervisor, Dr. Maidment, presented this topic at Vancouver in my absence.

In order to demonstrate the existence of super-resolution in an oblique reconstruction plane, a theoretical framework was developed in which the reconstruction of an obliquely pitched sine plate was calculated (Figure 1). With this model, I have studied differences in the output profiles of individual projections and reconstructions. A Selenia Dimensions DBT system (Hologic Inc., Bedford MA) with 140  $\mu\text{m}$  detector elements and 15 projections acquired over a  $15^\circ$  arc was simulated. Also, the input object was oriented at a pitch ( $\zeta$ ) of  $30^\circ$  relative to the breast support. To investigate the potential for super-resolution, the input frequency (5.0 lp/mm) was specified to be higher than the detector alias frequency, 3.6 lp/mm.

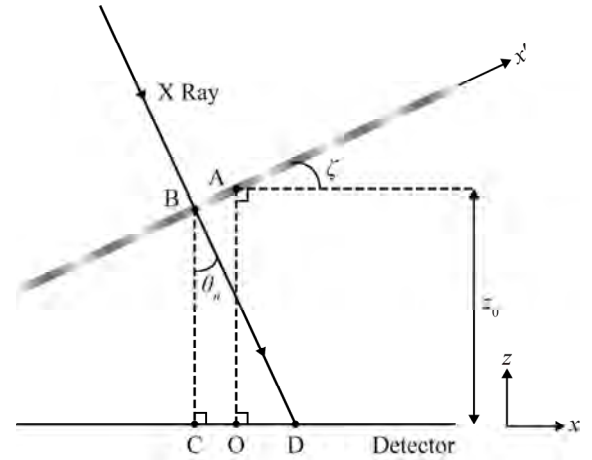


**Figure 1.** A schematic diagram of the DBT acquisition geometry is shown (figure not to scale). The input object (a sine plate) has an attenuation coefficient which varies sinusoidally along the angular pitch  $\zeta$ .

Figure 2 illustrates that the central projection cannot resolve the high frequency input object. As evidence of aliasing, the major peak in its Fourier transform occurs at a lower frequency (1.37 lp/mm) than the input frequency, 5.0 lp/mm. By contrast, SBP reconstruction can resolve the input and its major Fourier peak correctly occurs at 5.0 lp/mm. Adding ramp (RA) and spectrum apodization (SA) filters<sup>3</sup> to the reconstruction smoothens pixilation artifacts seen with SBP. These innovative results are unexpected based on the conventional interpretation of the Central Slice Theorem.<sup>3</sup> According to that theorem, Fourier space should be sampled only within double-napped cones (DNCs) whose opening angle matches the angular range of the DBT scan. The analytical modeling illustrates that super-resolution is possible well outside the DNCs whose opening angle spans  $-7.5^\circ$  to  $+7.5^\circ$  for the Selenia Dimensions system.

The feasibility of super-resolution in oblique reconstructions was later verified experimentally using a lead bar pattern phantom. The phantom was placed on a goniometry stand at a height of 7.6 cm above the breast support of a Selenia Dimensions DBT system. The goniometer was adjusted to vary the pitch of the bar patterns during the acquisition of 15 projections spanning a  $15^\circ$  arc. Reconstruction was performed along the obliquely pitched plane of the bar patterns using a commercial prototype reconstruction algorithm (Briona<sup>TM</sup>, Real Time Tomography, Villanova, PA). In the plane of the reconstruction, the pixel size of the reconstruction grid (11.7  $\mu\text{m}$ ) was much smaller than that of the detector elements (140  $\mu\text{m}$ ), so that the alias frequency of the reconstruction grid (42.7 lp/mm) was considerably higher than the alias frequency of the detector (3.57 lp/mm).

In the central projection acquired with bar patterns along a  $0^\circ$  pitch, frequencies up to 3.0 lp/mm are resolved (Figure 3). This finding is expected, since 3.0 lp/mm is below the detector alias frequency, 3.6 lp/mm for 140  $\mu\text{m}$  detector elements. At 4.0 lp/mm, however, a broad Moiré band<sup>14</sup> is present perpendicular to the bar patterns, and at 5.0 lp/mm, the bar patterns are represented as if they were a lower frequency ( $\sim 3.0$  lp/mm). By contrast, the reconstruction clearly shows spatial frequencies up to 5.0 lp/mm. Ultimately, the existence of super-resolution using the  $30^\circ$  pitch is significant because the DNCs in frequency space have an opening angle spanning approximately  $-7.5^\circ$  to  $+7.5^\circ$  for measurements made near the midpoint of the chest wall. At these locations along the detector, the divergence of the x-ray beam from the nominal projection angles is minimal, and the  $30^\circ$  pitch is therefore well outside the DNCs of frequency space.

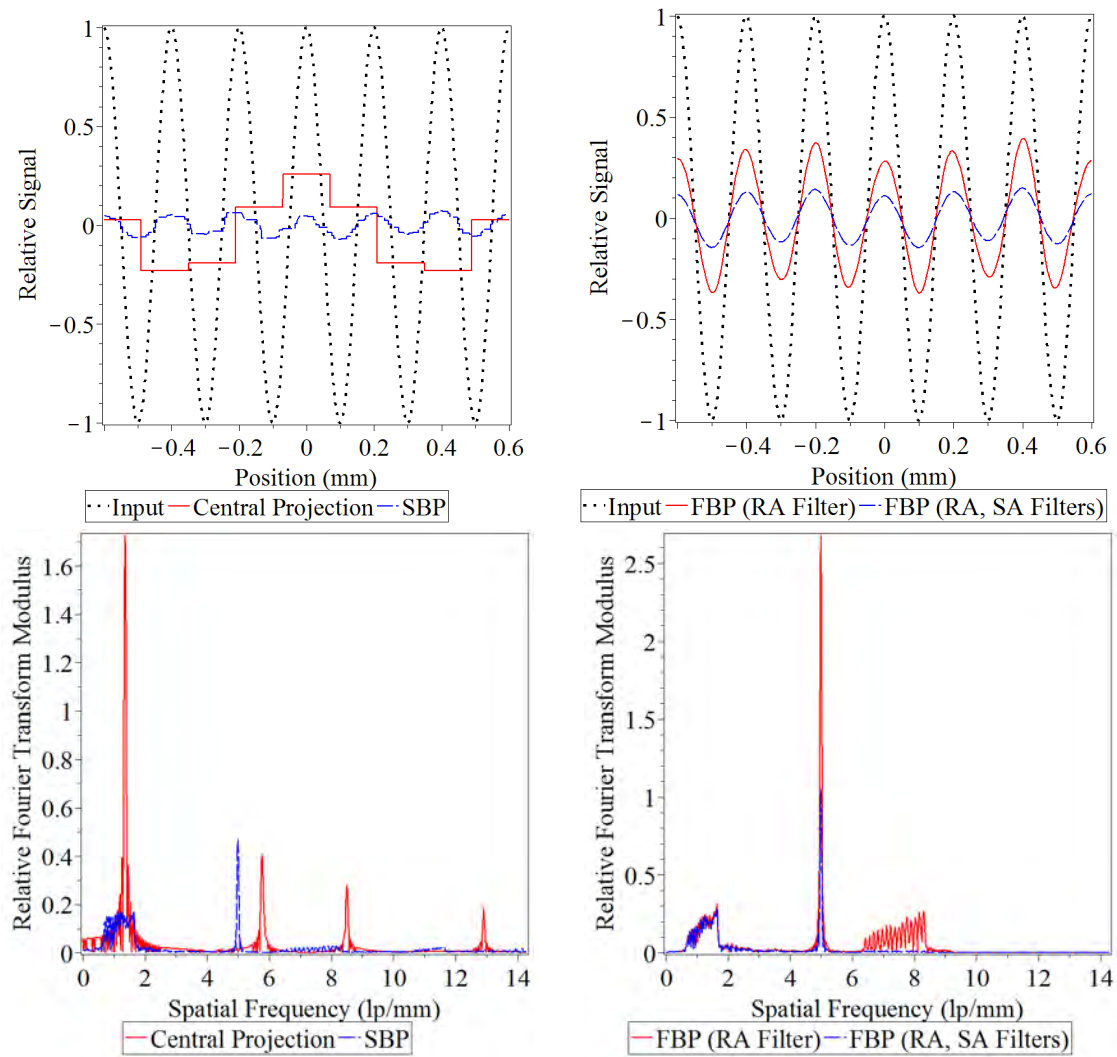


**Figure 2.** For a thin input object with a frequency of 5.0 lp/mm and an oblique pitch ( $\zeta$ ) of  $30^\circ$ , the central projection, SBP, and FBP reconstructions are compared in both the spatial and Fourier domains. The central height of the input object above the detector is 2.5 cm. A Selenia Dimensions DBT system (Hologic Inc., Bedford, MA) was simulated with  $140\ \mu\text{m}$  detector elements and 15 projections acquired over a  $15^\circ$  arc.

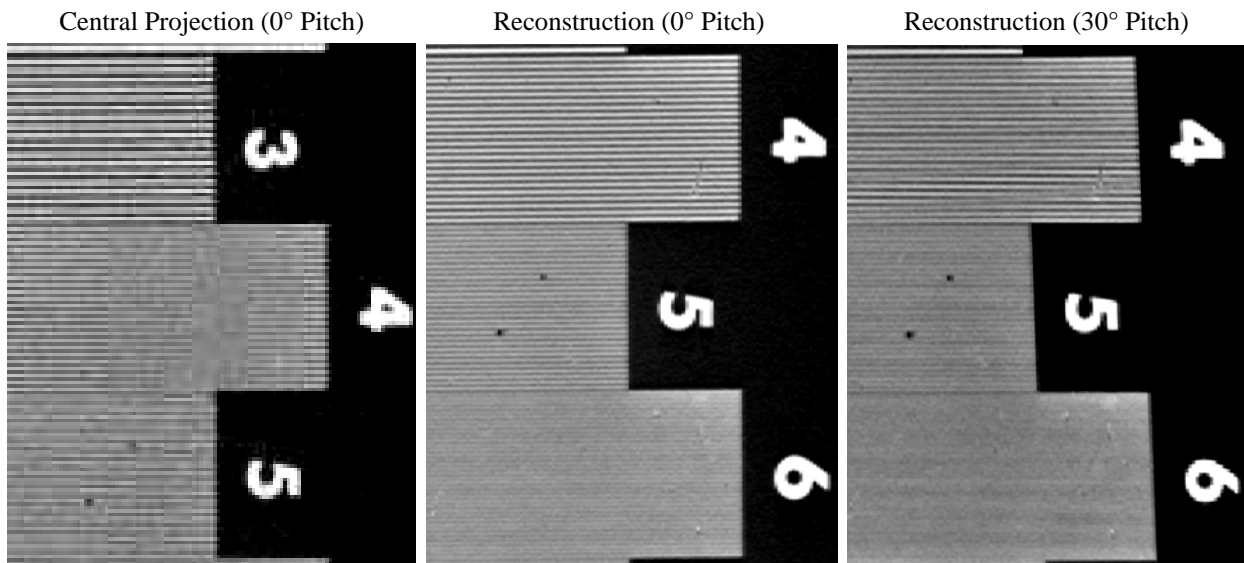


**Figure 3.** A bar pattern phantom was imaged with the Selenia Dimensions x-ray unit on a goniometry stand at  $0^\circ$  and  $30^\circ$  pitches. The reconstructions along both pitches can resolve higher frequencies than a single projection, providing experimental evidence of super-resolution.

To demonstrate the feasibility of super-resolution in oblique reconstruction planes using clinical images, reconstructions of microcalcifications were performed on grids with the pixel size  $28\text{ }\mu\text{m}$  using the Selenia Dimensions system. As shown in Figure 4, the visibility of microcalcifications in the lower half of the reconstruction does not differ considerably using either a  $0^\circ$  or  $30^\circ$  pitch. Although the upper right calcifications are not visible with the  $30^\circ$  pitch, visibility can be improved by simply translating the plane of reconstruction until they come into focus. Having a clear image of the structural features of microcalcifications at oblique pitches is useful because there may be cases whose morphological properties are best assessed along these directions.

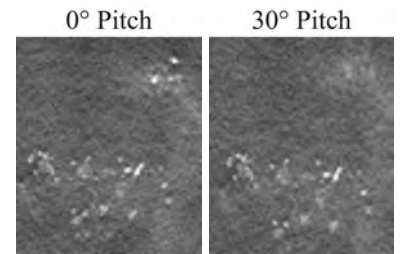


**Figure 4.** Two reconstructions of microcalcifications are shown.

## II. D. Optimization of Scan Time in DBT

In SA2 of my predoctoral DOD grant, I proposed to investigate differences in image quality comparing systems with continuous tube motion and step-and-shoot motion. Systems with continuous tube motion have the advantage of shorter scan time and hence less patient motion than systems with step-and-shoot motion. Their drawback, however, is blurring due to focal spot motion.<sup>3, 18, 19</sup>

In this work, I have used the concept of a sine plate to investigate subtleties of the imaging system that were not modeled in my super-resolution research. Unlike my super-resolution research which assumed a stationary sine plate, this project simulates the motion of the sine plate at a fixed velocity during the DBT scan in order to simulate patient motion. The reconstruction of the sine plate is calculated for various input frequencies and for either continuous tube motion or step-and-shoot motion. My work determines the optimal scan time which minimizes the trade-offs between patient motion and focal spot motion by maximizing the modulation of the reconstruction in a system with continuous tube motion.

My work demonstrates that a system with step-and-shoot motion will always have superior modulation relative to a system with continuous tube motion and with otherwise similar acquisition parameters. Consequently, in order to optimize a step-and-shoot system, the scan time yielding the same modulation as the highest achievable with continuous tube motion is calculated. This scan time provides a threshold below which the benefits of step-and-shoot motion are not outweighed by its drawbacks.

This analysis of image quality in systems with patient motion and either continuous tube motion or step-and-shoot motion is presented in an upcoming proceedings manuscript for the SPIE Physics of Medical Imaging conference in February, 2012 in San Diego, California.<sup>20</sup> Because no other researcher has modeled both tube motion and patient motion simultaneously, my work is the first to demonstrate a platform for optimizing scan time in DBT.

## III. KEY RESEARCH ACCOMPLISHMENTS

- In a recently published article for the journal *Medical Physics*,<sup>4</sup> I have proposed the first closed form model of the effect of oblique x-ray incidence on the transfer functions of DBT projections without making the simplifying assumption that the PSF for normal incidence is a delta function. Following an aim established in SA1 of my predoctoral DOD grant, this model has allowed me to demonstrate the spatial anisotropy of the transfer functions in each projection by carefully calculating the incident angle at each point on the detector.
- My research has been the first to show that DBT is capable of super-resolution (*i.e.*, sub-pixel resolution) using analytical modeling and experimental reconstructions of bar patterns.<sup>11</sup> The clinical impact of super-resolution is optimizing the visibility of microcalcifications in reconstructions performed on grids with



much smaller pixilation than the detector. The existence of super-resolution was later generalized to reconstruction planes with a broad range of pitches relative to the breast support.<sup>16, 17</sup>

- Much of my research effort has also focused on the development of optimization strategies for DBT, as described in SA2 of my predoctoral DOD grant. To date, two optimization strategies have been proposed. First, the phosphor thickness which optimizes DQE has been calculated for various projection angles.<sup>4</sup> Second, the optimal scan time has been evaluated in systems with patient motion and either continuous tube motion or patient motion.<sup>20</sup>

## IV. REPORTABLE OUTCOMES

- Acciavatti RJ, Maidment ADA. Optimization of phosphor-based detector design for oblique x-ray incidence in digital breast tomosynthesis. *Medical Physics*. 2011;38(11):6188-202.
- Acciavatti RJ, Maidment ADA. Optimization of In-Plane Resolution in Digital Breast Tomosynthesis Using Super-Resolution Image Reconstruction. *Medical Physics*. 2012: **to be submitted for review**.
- Acciavatti RJ, Maidment ADA. TU-A-301-07: Experimental and Theoretical Validation of Breast Tomosynthesis Reconstructions along Oblique Planes. *Medical Physics*. 2011;38(6):3746.
- Acciavatti RJ, Maidment ADA. An Analysis of Super-Resolution in Oblique Reconstructions for Digital Breast Tomosynthesis. Era of Hope Conference; 2011 (conference abstract); Orlando, FL; 2011 (**conference abstract**).
- Acciavatti RJ, Maidment ADA. Optimization of Continuous Tube Motion and Step-and-Shoot Motion in Digital Breast Tomosynthesis Systems with Patient Motion. In: Pelc NJ, Nishikawa RM, Whiting BR, editors. SPIE; 2012; San Diego, CA: SPIE; 2012. p. (**accepted**).

## V. CONCLUSION

My research on the resolution loss due to oblique x-ray incidence in DBT projections (Section II. A.) can effectively be considered complete, since it has been published in the November 2011 issue of the journal *Medical Physics*.<sup>4</sup> As I proposed in SA1 of my predoctoral DOD grant, this article demonstrates the spatial anisotropy of transfer functions in individual projections by carefully modeling the incident angle at each point on the detector. To explore optimization strategies for DBT as I proposed in SA2, this work shows that the phosphor thickness which maximizes DQE is projection angle dependent.

In addition, I have demonstrated the existence of super-resolution in DBT (Section II. B.) by calculating the reconstruction of a sine plate whose attenuation coefficient varies with position at a frequency higher than the detector alias frequency. The results of my analytical modeling were supported by evidence of super-resolution in experimental images of bar patterns and select clinical images of microcalcifications. A full manuscript on super-resolution will soon be submitted to the *Medical Physics* journal for review.<sup>11</sup> My future work on this project will involve responding to referee criticisms if the manuscript is accepted for publication.

My most recent projects on oblique reconstructions (Section II. C.) and optimization of scan time (Section II. D.) have been accepted for presentation at conferences,<sup>16, 17, 20</sup> but have not yet been formulated as manuscript submissions to a journal. In the coming months, it will be important to expand upon the fundamental ideas of these projects in order to develop peer-reviewed manuscript submissions. Although my current work on oblique DBT reconstructions studies the effect of orienting the reconstruction plane at various angles relative to the chest wall side of the breast support, it will be useful to model the effect of orienting the

plane at various angles relative to the chest wall-to-nipple direction as well. In my work on scan time optimization, I plan to model patient motion velocities that vary with time, such as the pulsatile motion of objects near a blood vessel, in addition to the constant velocities that are simulated in my SPIE proceedings manuscript.<sup>20</sup>

I have completed all non-thesis requirements for my doctoral degree. By the end of 2012, I plan to complete my thesis. This time frame was chosen in coordination with the termination of this DOD predoctoral training grant. My thesis committee met on January 5, 2012 and agreed with this time frame.

## VI. REFERENCES

- <sup>1</sup>Rafferty EA. Tomosynthesis: New weapon in breast cancer fight. *Decisions in Imaging Economics*. 2004;17(4).
- <sup>2</sup>Poplack SP, Tosteson TD, Kogel CA, Nagy HM. Digital breast tomosynthesis: initial experience in 98 women with abnormal digital screening mammography. *American Journal of Roentgenology*. 2007;189(3):616-23.
- <sup>3</sup>Zhao B, Zhao W. Three-dimensional linear system analysis for breast tomosynthesis. *Medical Physics*. 2008;35(12):5219-32.
- <sup>4</sup>Acciavatti RJ, Maidment ADA. Optimization of phosphor-based detector design for oblique x-ray incidence in digital breast tomosynthesis. *Medical Physics*. 2011;38(11):6188-202.
- <sup>5</sup>Swank RK. Calculation of Modulation Transfer Functions of X-Ray Fluorescent Screens. *Appl Opt*. 1973;12(8):1865-70.
- <sup>6</sup>Marshak RE, Brooks H, Hurwitz Jr. H. Introduction to the Theory of Diffusion and Slowing Down of Neutrons - I. *Nucleonics*. 1949;4:10-22.
- <sup>7</sup>Mainprize JG, Bloomquist AK, Kempston MP, Yaffe MJ. Resolution at oblique incidence angles of a flat panel imager for breast tomosynthesis. *Medical Physics*. 2006;33(9):3159-64.
- <sup>8</sup>Hajdok G, Cunningham IA. Penalty on the detective quantum efficiency from off-axis incident x rays. In: Yaffe MJ, Flynn MJ, editors. *Medical Imaging 2004: Physics of Medical Imaging*; 2004; San Diego: SPIE; 2004. p. 109-18.
- <sup>9</sup>Badano A, Kyprianou IS, Sempau J. Anisotropic imaging performance in indirect x-ray imaging detectors. *Medical Physics*. 2006;33(8):2698-713.
- <sup>10</sup>Que W, Rowlands JA. X-ray imaging using amorphous selenium: Inherent spatial resolution. *Medical Physics*. 1995;22(4):365-74.
- <sup>11</sup>Acciavatti RJ, Maidment ADA. Optimization of In-Plane Resolution in Digital Breast Tomosynthesis Using Super-Resolution Image Reconstruction. *Medical Physics*. 2012:(to be submitted for review).
- <sup>12</sup>Acciavatti RJ, Maidment ADA. Investigating the Potential for Super-Resolution in Digital Breast Tomosynthesis. In: Pelc NJ, Samei E, Nishikawa RM, editors. *SPIE*; 2011; Lake Buena Vista, FL: SPIE; 2011. p. 79615K-1 - K-12.
- <sup>13</sup>Freeman T. DBT: imaging with super-resolution. 2011 [cited 2012 January 25]; Available from: <http://medicalphysicsweb.org/cws/article/research/45274>
- <sup>14</sup>Albert M, Beideck DJ, Bakic PR, Maidment ADA. Aliasing effects in digital images of line-pair phantoms. *Medical Physics*. 2002;29(8):1716-8.
- <sup>15</sup>Lanyi M. Chapter 7: Differential Diagnosis of Microcalcifications. *Diagnosis and Differential Diagnosis of Breast Calcifications*. Berlin: Springer-Verlag; 1988. p. 193-231.
- <sup>16</sup>Acciavatti RJ, Maidment ADA. TU-A-301-07: Experimental and Theoretical Validation of Breast Tomosynthesis Reconstructions along Oblique Planes. *Medical Physics*. 2011;38(6):3746.
- <sup>17</sup>Acciavatti RJ, Maidment ADA. An Analysis of Super-Resolution in Oblique Reconstructions for Digital Breast Tomosynthesis. *Era of Hope Conference*; 2011 (conference abstract); Orlando, FL; 2011 (conference abstract).
- <sup>18</sup>Ren B, Ruth C, Stein J, Smith A, Shaw I, Jing Z. Design and performance of the prototype full field breast tomosynthesis system with selenium based flat panel detector. In: Flynn MJ, editor. *SPIE*; 2005; San Diego, CA: SPIE; 2005. p. 550-61.

- <sup>19</sup>Bissonnette M, Hansroul M, Masson E, Savard S, Cadieux S, Warmoes P, et al. Digital breast tomosynthesis using an amorphous selenium flat panel detector. In: Flynn MJ, editor. SPIE; 2005: (SPIE, Bellingham, WA, 2005); 2005. p. 529-40.
- <sup>20</sup>Acciavatti RJ, Maidment ADA. Optimization of Continuous Tube Motion and Step-and-Shoot Motion in Digital Breast Tomosynthesis Systems with Patient Motion. In: Pelc NJ, Nishikawa RM, Whiting BR, editors. SPIE; 2012; San Diego, CA: SPIE; 2012. p. (accepted).

## VII. APPENDICES

1. Acciavatti RJ, Maidment ADA. Optimization of phosphor-based detector design for oblique x-ray incidence in digital breast tomosynthesis. *Medical Physics*. 2011;38(11):6188-202.
2. Acciavatti RJ, Maidment ADA. Optimization of In-Plane Resolution in Digital Breast Tomosynthesis Using Super-Resolution Image Reconstruction. *Medical Physics*. 2012: **Draft to be Submitted to *Medical Physics Journal* for Review.**
3. Acciavatti RJ, Maidment ADA. TU-A-301-07: Experimental and Theoretical Validation of Breast Tomosynthesis Reconstructions along Oblique Planes. *Medical Physics*. 2011;38(6):3746.
4. Acciavatti RJ, Maidment ADA. An Analysis of Super-Resolution in Oblique Reconstructions for Digital Breast Tomosynthesis. Era of Hope Conference; 2011 (Conference Abstract); Orlando, FL; 2011.
5. Acciavatti RJ, Maidment ADA. Optimization of Continuous Tube Motion and Step-and-Shoot Motion in Digital Breast Tomosynthesis Systems with Patient Motion. In: Pelc NJ, Nishikawa RM, Whiting BR, editors. SPIE; 2012; San Diego, CA: SPIE; 2012. **Draft of Accepted Conference Proceedings.**

# Optimization of phosphor-based detector design for oblique x-ray incidence in digital breast tomosynthesis

Raymond J. Acciavatti and Andrew D. A. Maidment<sup>a)</sup>

Department of Radiology, Perelman School of Medicine at the University of Pennsylvania, Philadelphia, Pennsylvania 19104

(Received 24 May 2011; revised 20 August 2011; accepted for publication 28 August 2011; published 26 October 2011)

**Purpose:** In digital breast tomosynthesis (DBT), a volumetric reconstruction of the breast is generated from a limited range of x-ray projections. One trade-off of DBT is resolution loss in the projections due to non-normal (i.e., oblique) x-ray incidence. Although degradation in image quality due to oblique incidence has been studied using empirical data and Monte Carlo simulations, a theoretical treatment has been lacking. The purpose of this work is to extend Swank's calculations of the transfer functions of turbid granular phosphors to oblique incidence. The model is ultimately used as a tool for optimizing the design of DBT detectors.

**Methods:** A quantum-limited system and 20 keV x-rays are considered. Under these assumptions, the modulation transfer function (MTF) and noise power spectra (NPS) are derived using the diffusion approximation to the Boltzmann equation to model optical scatter within the phosphor. This approach is applicable to a nonstructured scintillator such as gadolinium oxysulfide doped with terbium ( $\text{Gd}_2\text{O}_2\text{S:Tb}$ ), which is commonly used in breast imaging and which can reasonably approximate other detector materials. The detective quantum efficiency (DQE) is then determined from the Nishikawa formulation, where it is written as the product of the x-ray quantum detection efficiency, the Swank factor, and the Lubberts fraction. Transfer functions are calculated for both front- and back-screen configurations, which differ by positioning the photocathode at the exit or entrance point of the x-ray beam, respectively.

**Results:** In the front-screen configuration, MTF and DQE are found to have considerable angular dependence, while NPS is shown to vary minimally with projection angle. As expected, the high frequency MTF and DQE are degraded substantially at large angles. By contrast, all transfer functions for the back-screen configuration have the advantage of significantly less angular dependence. Using these models, we investigated the possibility for optimizing the design of DBT detectors. As an example optimization strategy, the phosphor thickness which maximizes the DQE at a fixed frequency is analyzed. This work demonstrates that the optimal phosphor thickness for the front-screen is angularly dependent, shifting to lower thickness at higher angles. Conversely, the back-screen is not optimized by a single thickness but instead attains reasonably high DQE values over a large range of thicknesses. Although the back-screen configuration is not suited for current detectors using a glass substrate, it may prove to be preferred in future detectors using newly proposed plastic thin-film transistor (TFT) substrates.

**Conclusions:** Using the diffusion approximation to the Boltzmann equation to model the spread of light in a scintillator, this paper develops an analytical model of MTF, NPS, and DQE for a phosphor irradiated obliquely. The model is set apart from other studies on oblique incidence in being derived from first principles. This work has applications in the optimization of DBT detector design. © 2011 American Association of Physicists in Medicine. [DOI: 10.1118/1.3639999]

Key words: oblique x-ray incidence, digital breast tomosynthesis (DBT), optical transfer function (OTF), noise power spectra (NPS), detective quantum efficiency (DQE)

## I. INTRODUCTION

In many radiographic studies, non-normally (i.e., obliquely) incident x-rays provide a source of blurring at the periphery of the detector due to the divergence of the x-ray beam emitted from the focal spot. Que and Rowlands proposed an analytical model of the resolution loss due to oblique incidence by deriving an expression for the modulation transfer function (MTF) of amorphous selenium (*a*-Se) detectors from

first principles.<sup>1</sup> Their work assumes that the detector is operated in drift mode, so that the point spread function (PSF) for normal incidence is a delta function and hence the MTF for normal incidence is unity at all frequencies.<sup>2</sup>

Oblique incidence is more readily observed in digital mammography (DM) than many other imaging studies. A DM detector is placed closer to the focal spot than most modalities<sup>3</sup> to counteract the loss in x-ray penetration resulting from the use of relatively low energies ( $\sim 20$  keV).<sup>4-6</sup>

The drawback of decreasing the source-to-detector distance is increasing the angle of incidence relative to the normal, especially at the edges of the detector. For example, the maximum angle of incidence is  $25^\circ$  for a DM system with a detector field-of-view (FOV) of  $24 \times 30$  cm and a source-to-image distance of 70 cm measured at the midpoint of the chest wall.

In digital breast tomosynthesis (DBT), low dose x-ray projection images are acquired over a limited range of angles around the breast, and sharply in-focus slices at all depths of the breast volume are generated using image reconstruction techniques. Preliminary studies indicate that DBT provides increased sensitivity and specificity relative to DM for the early detection of breast cancer in women.<sup>7</sup> One shortcoming of DBT, however, is that it is more directly impacted by the resolution loss due to oblique incidence than DM. The maximum projection angle in DBT can be as large as  $20^\circ$  or  $30^\circ$ , and the angle of incidence at the edges of the detector is even higher if one takes into account the divergent x-ray beam geometry. While some DBT systems incorporate a rotating detector to counteract changes in obliquity, many systems employ a stationary detector.

Mainprize *et al.* experimentally demonstrated the resolution loss due to oblique incidence in cesium iodide doped with thallium (CsI:TI), a structured phosphor-based detector, using the slanted edge technique to measure MTF.<sup>8</sup> The authors showed that at  $10^\circ$  incidence, the MTF degradation becomes comparable to the resolution loss associated with other common sources of image blurring, such as the blurring of the focal spot and the lateral spread of visible light within the scintillator. At  $40^\circ$  incidence, the MTF is reduced considerably; for example, at 5 line pairs per mm (lp/mm), the MTF is degraded by 35%–40% over a broad range of kVp and target-filter combinations.

While Mainprize *et al.* did not measure noise power spectra (NPS), Hajdok and Cunningham have calculated NPS using Monte Carlo simulations of *a*-Se.<sup>3</sup> Their work demonstrated that unlike MTF, NPS has minimal angular dependence. Since the detective quantum efficiency (DQE) is dependent upon the square of the MTF, Hajdok and Cunningham have shown that the DQE degradation with oblique incidence at high frequencies is more pronounced than the MTF degradation.

Although oblique incidence has been studied experimentally and using Monte Carlo simulations, a theoretical treatment has been lacking. For this reason, the purpose of this paper is to extend Swank's calculations<sup>9</sup> of the transfer functions of turbid granular phosphors to oblique incidence. Building off our previous work on oblique incidence,<sup>10</sup> we analyze the light diffusion equations in a nonstructured scintillator such as gadolinium oxysulfide doped with terbium ( $\text{Gd}_2\text{O}_2\text{S:Tb}$ ), which is commonly used in breast imaging and which can reasonably approximate other detector materials. The theoretical formulation of this work differs from the one proposed by Que and Rowlands in not making the assumption that the PSF for normal incidence is a delta function. Ultimately, the analytical model is used as a tool for optimizing the design of the phosphor for oblique incidence.

## II. METHODS

### II.A. Transfer functions for front-screen configuration

The optical transfer function (OTF), NPS, and DQE of a turbid granular phosphor are derived here from first principles for all angles of incidence. The Boltzmann transport equation may be used to model the spread of visible light in a turbid phosphor. A first-order, steady state solution to the Boltzmann transport equation is a diffusion equation of the form<sup>11</sup>

$$-\nabla^2 \phi(\mathbf{r}) + \sigma^2 \phi(\mathbf{r}) = S(\mathbf{r}), \quad (1)$$

where  $\phi(\mathbf{r})$  is the product of the density of the secondary carriers (i.e., the optical photons) with the diffusion constant,  $\sigma$  is the reciprocal of the mean diffusion length of the secondary carriers, and  $S(\mathbf{r})$  is the source function. The diffusion equation is a useful approximation to the Boltzmann transport equation provided that three criteria are met: (1) solutions for  $\phi(\mathbf{r})$  are determined far from the x-ray source  $S(\mathbf{r})$  relative to the mean free path of optical scatter; (2) the optical properties of the phosphor possess no discontinuities; and (3) the probability of optical absorption is small compared against the probability of optical scatter.<sup>12</sup> This model has been used by Swank for normal incidence<sup>9</sup> and has shown good agreement with experimental data.<sup>12,13</sup>

As shown in Fig. 1, the source function  $S(\mathbf{r})$  in Eq. (1) may be modeled as the point  $(z_0 \tan \theta, 0, z_0)$  along the x-ray path length, where  $z_0$  is depth within the scintillator of total thickness  $T$  and where  $\theta$  is the angle of incidence relative to the normal. In terms of delta functions,  $S(\mathbf{r})$  can be written as

$$S(\mathbf{r}) = \delta(x - z_0 \tan \theta) \delta(y) \delta(z - z_0). \quad (2)$$

Using the Fourier representation of the delta function,<sup>14</sup> the source function can equivalently be expressed as the integral

$$S(\mathbf{r}) = \delta(z - z_0) \int_{-\infty}^{\infty} \int_{-\infty}^{\infty} e^{2\pi i[(x - z_0 \tan \theta)\nu_x + y\nu_y]} d\nu_x d\nu_y. \quad (3)$$

Defining  $\mathbf{v}$  as the 2D spatial frequency vector with components  $\nu_x$  and  $\nu_y$ , solutions to Eq. (1) can be written in the form

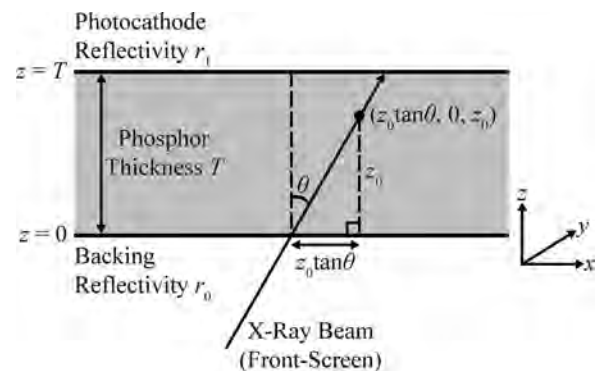


FIG. 1. In terms of delta functions, the source function  $S(\mathbf{r})$  at the depth  $z_0$  of the phosphor is found from trigonometry to be  $\delta(x - z_0 \tan \theta) \delta(y) \delta(z - z_0)$ , where  $\theta$  is the angle of x-ray incidence relative to the normal. The figure assumes a front-screen configuration in which x-rays are incident on the backing at  $z=0$  before striking the photocathode at  $z=T$ . Reversing the direction of the arrowhead of the x-ray beam converts the front-screen configuration to a back-screen configuration.

$$\phi(x, y, z) = \int_{-\infty}^{\infty} \int_{-\infty}^{\infty} \psi_{\mathbf{k}}(z) e^{2\pi i(x\nu_x + y\nu_y)} d\nu_x d\nu_y. \quad (4)$$

Substituting Eqs. (3) and (4) into Eq. (1), it can be shown that

$$-\frac{d^2\psi_{\mathbf{k}}}{dz^2} + q^2\psi_{\mathbf{k}} = e^{-ik_x z_0 \tan \theta} \delta(z - z_0), \quad (5)$$

where

$$q^2 = \sigma^2 + k_x^2 + k_y^2, \quad (6)$$

$$\psi_{\mathbf{k}}(z) = \begin{cases} C_1 \cosh(qz) + \frac{C_2}{q} \sinh(qz), & 0 \leq z \leq z_0 \\ C_1 \cosh(qz) + \frac{C_2}{q} \sinh(qz) - \frac{e^{-ik_x z_0 \tan \theta}}{q} \sinh[q(z - z_0)], & z_0 < z \leq T \end{cases} \quad (9)$$

The constants  $C_1$  and  $C_2$  can now be determined from boundary conditions concerning secondary carrier currents directed toward the planes at  $z=0$  and  $z=T$ . In terms of the inverse relaxation length,  $\tau$ , the secondary carrier currents across any plane of constant  $z$  are

$$j_{\text{left}}(z) = \frac{1}{2} \left[ \phi\tau + \frac{d\phi}{dz} \right], \quad (10)$$

$$j_{\text{right}}(z) = \frac{1}{2} \left[ \phi\tau - \frac{d\phi}{dz} \right]. \quad (11)$$

In the right-hand side of the two equations, the first term models the effusion current, while the second term comes from Fick's law. The first boundary condition is determined by the reflectivity  $r_0$  of the plane at  $z=0$ . Noting that  $j_{\text{right}}(0) = r_0 j_{\text{left}}(0)$ , one finds

$$\left. \frac{d\phi}{dz} \right|_{z=0} = \tau\rho_0 \phi|_{z=0}, \quad (12)$$

where

$$\rho_0 \equiv \frac{1 - r_0}{1 + r_0}. \quad (13)$$

The second boundary condition is determined from the reflectivity  $r_1$  of the boundary at  $z=T$ , as stipulated by the expression  $j_{\text{left}}(T) = r_1 j_{\text{right}}(T)$ . Defining  $\rho_1$  similar to  $\rho_0$  and noting that the boundary conditions hold for each Fourier component  $\psi_{\mathbf{k}}$  of  $\phi$ , it can be shown that

$$C_1 = \left[ \frac{(q + \tau\rho_1)e^{q(T-z_0)} + (q - \tau\rho_1)e^{-q(T-z_0)}}{(q + \tau\rho_0)(q + \tau\rho_1)e^{qT} - (q - \tau\rho_0)(q - \tau\rho_1)e^{-qT}} \right] \times e^{-ik_x z_0 \tan \theta}, \quad (14)$$

$$C_2 = \tau\rho_0 C_1. \quad (15)$$

Consistent with Swank's approach, the photocathode is defined by the plane  $z=T$  and the backing is defined by the

$$\mathbf{k} = 2\pi\mathbf{v}. \quad (7)$$

To solve Eq. (5) for  $\psi_{\mathbf{k}}(z)$ , one can apply integral transform techniques.<sup>15,16</sup> Denoting the Laplace transform of  $\psi_{\mathbf{k}}(z)$  as  $\mathcal{L}_{\mathbf{k}}(p)$ , the transform of the differential equation is

$$(-p^2 + q^2) \cdot \mathcal{L}_{\mathbf{k}}(p) + C_1 p + C_2 = e^{-ik_x z_0 \tan \theta} e^{-pz_0}, \quad (8)$$

where  $C_1$  and  $C_2$  are the constants of integration. Solving for  $\mathcal{L}_{\mathbf{k}}(p)$  and taking the inverse transform generates the following piece-wise expression for  $\psi_{\mathbf{k}}(z)$ :

plane  $z=0$ , as diagrammed schematically in Fig. 1. The OTF of the scattering process,  $G(\mathbf{v}, z_0)$ , is then determined for a point source from the expression

$$G(\mathbf{v}, z_0) = \left[ \frac{\rho_1}{1 + \rho_1} \right] \left[ \psi_{\mathbf{k}}\tau - \frac{d\psi_{\mathbf{k}}}{dz} \right] \Big|_{z=T}. \quad (16)$$

Hence,

$$G(\mathbf{v}, z_0) = \tau\rho_1 \left[ \frac{(q + \tau\rho_0)e^{(q-ik_x \tan \theta)z_0} + (q - \tau\rho_0)e^{-(q+ik_x \tan \theta)z_0}}{(q + \tau\rho_0)(q + \tau\rho_1)e^{qT} - (q - \tau\rho_0)(q - \tau\rho_1)e^{-qT}} \right]. \quad (17)$$

To calculate the OTF of the entire phosphor, one multiplies Eq. (17) by the relative x-ray signal as a function of the depth  $z_0$

$$N_F(z_0) = \frac{\mu e^{-\mu z_0 \sec \theta} \sec \theta}{1 - e^{-\mu T \sec \theta}}, \quad (18)$$

where  $\mu$  is the linear attenuation coefficient of the phosphor, and then integrates over the phosphor thickness. Assuming a front-screen ( $F$ ) configuration in which x-rays are first incident on the backing at  $z=0$  before striking the photocathode at  $z=T$ , the OTF is thus

$$G_F(\mathbf{v}) = \int_0^T N_F(z_0) G(\mathbf{v}, z_0) dz_0 \quad (19)$$

$$= \frac{\beta \mu \sec \theta}{1 - e^{-\mu T \sec \theta}} \left[ \frac{(q + \tau\rho_0)(e^{(\gamma_- - ik_x \tan \theta)T} - 1)}{\gamma_- - ik_x \tan \theta} - \frac{(q - \tau\rho_0)(e^{-(\gamma_+ + ik_x \tan \theta)T} - 1)}{\gamma_+ + ik_x \tan \theta} \right], \quad (20)$$

where

$$\beta \equiv \frac{\tau\rho_1}{(q + \tau\rho_0)(q + \tau\rho_1)e^{qT} - (q - \tau\rho_0)(q - \tau\rho_1)e^{-qT}}, \quad (21)$$

$$\gamma_{\pm} \equiv q \pm \mu \sec \theta. \quad (22)$$

The MTF is found from the normalized modulus of the OTF.<sup>17</sup>

In the absence of outside noise sources, the quantum NPS or  $W_F(\mathbf{v})$  is calculated by integrating the product of  $N_F(z_0)$  with  $|G(\mathbf{v}, z_0)|^2$  from  $z_0=0$  to  $z_0=T$ .



$$W_F(\mathbf{v}) = \int_0^T N_F(z_0) |G(\mathbf{v}, z_0)|^2 dz_0 \quad (23)$$

$$= \frac{\beta^2 \mu \sec \theta}{1 - e^{-\mu T \sec \theta}} \left[ \frac{(q + \tau \rho_0)^2 (e^{(q+\gamma_-)T} - 1)}{q + \gamma_-} + \frac{2(q^2 - \tau^2 \rho_0^2)(1 - e^{-\mu T \sec \theta})}{\mu \sec \theta} + \frac{(q - \tau \rho_0)^2 (1 - e^{-(q+\gamma_+)T})}{q + \gamma_+} \right] \quad (24)$$

With the OTF and quantum NPS known, it is now possible to determine the DQE. From the work of Nishikawa, DQE can be formulated as the product of four terms<sup>12</sup>

$$\text{DQE}(\mathbf{v}) = A_Q A_S R_C(\mathbf{v}) R_N(\mathbf{v}), \quad (25)$$

where  $A_Q$  is the x-ray quantum detection efficiency (QDE) determined by the Lambert-Beer Law as

$$A_Q = 1 - e^{-\mu T \sec \theta}, \quad (26)$$

$A_S$  is the Swank information factor

$$A_S = \frac{G_F^2(\mathbf{0})}{W_F(\mathbf{0})}, \quad (27)$$

$R_C(\mathbf{v})$  is the Lubberts fraction

$$R_C(\mathbf{v}) = \frac{1}{A_S} \cdot \frac{|G_F(\mathbf{v})|^2}{W_F(\mathbf{v})}, \quad (28)$$

and  $R_N(\mathbf{v})$  is the ratio of the x-ray quantum noise power to the total noise power. Assuming a quantum-limited imaging system,  $R_N(\mathbf{v})$  is taken to be unity in this work.

$$W_B(\mathbf{v}) = \frac{\beta^2 \mu \sec \theta}{e^{\mu T \sec \theta} - 1} \left[ \frac{(q + \tau \rho_0)^2 (e^{(q+\gamma_+)T} - 1)}{q + \gamma_+} + \frac{2(q^2 - \tau^2 \rho_0^2)(e^{\mu T \sec \theta} - 1)}{\mu \sec \theta} + \frac{(q - \tau \rho_0)^2 (1 - e^{-(q+\gamma_-)T})}{q + \gamma_-} \right]. \quad (31)$$

Equations (30) and (31) follow from Eqs. (19) and (23); the subscript “B” is used to denote a back-screen.

### III. RESULTS FOR A MODEL DETECTOR

#### III.A. Transfer Functions for Front- and Back-Screen Configurations

The OTF, NPS, and DQE calculations are now illustrated for a phosphor with a reflective backing ( $r_0 = 1$ ), a nonreflective photocathode ( $r_1 = 0$ ), and optical scatter at the diffusion limit ( $\tau \rightarrow \infty$ ). In view of the limitations of Swank’s model, a large value of  $\tau$  has been chosen. As Swank demonstrated in his original paper,<sup>9</sup> the MTF of a scattering phosphor ( $\tau > 0$ ) is always higher than the MTF a nonscattering phosphor ( $\tau = 0$ ) at low frequencies, but the opposite trend arises at high frequencies. The crossover point of the scattering and nonscattering MTF curves corresponds to the frequency beyond which Swank’s model becomes inaccurate. For very small values of  $\tau$ , the crossover point occurs at relatively low frequencies. However, for infinite  $\tau$ , the scattering MTF

#### II.B. Transfer functions for back-screen configuration

In a similar fashion, the transfer functions for a back-screen (B) configuration can be calculated. Unlike the front-screen configuration, x-rays first strike the photocathode at  $z = T$  before passing through the backing at  $z = 0$ . This modification reverses the direction of the x-ray beam in Fig. 1 without further altering the diagram. Hence

$$N_B(z_0) = \frac{\mu e^{-\mu(T-z_0) \sec \theta} \sec \theta}{1 - e^{-\mu T \sec \theta}}, \quad (29)$$

so that the OTF and quantum NPS are found to be

$$G_B(\mathbf{v}) = \frac{\beta \mu \sec \theta}{e^{\mu T \sec \theta} - 1} \left[ \frac{(q + \tau \rho_0)(e^{(\gamma_+ - ik_x \tan \theta)T} - 1)}{\gamma_+ - ik_x \tan \theta} - \frac{(q - \tau \rho_0)(e^{-(\gamma_- + ik_x \tan \theta)T} - 1)}{\gamma_- + ik_x \tan \theta} \right], \quad (30)$$

curve never crosses the nonscattering MTF curve between 0 and 10 lp/mm. Hence, Swank’s model is increasingly accurate in approaching the diffusion limit.

In calculating the transfer functions, we assume 20 keV monoenergetic x-rays<sup>4-6</sup> and a porous, 100  $\mu\text{m}$  thick  $\text{Gd}_2\text{O}_2\text{S:Tb}$  phosphor with 50% packing density. The attenuation coefficient  $\mu$  for the porous phosphor is determined by halving the value for a crystalline phosphor.<sup>12</sup> Since crystalline  $\text{Gd}_2\text{O}_2\text{S}$  has a mass density of 7.34  $\text{g/cm}^3$  and a mass attenuation coefficient of 36.9  $\text{cm}^2/\text{g}$  for 20 keV x-rays,<sup>18</sup> the attenuation coefficient for porous  $\text{Gd}_2\text{O}_2\text{S}$  is 13.5  $\text{mm}^{-1}$ .

In Fig. 2, cross sections of the MTF surface are plotted versus frequency at two polar angles ( $\alpha$ ) of the frequency vector ( $0^\circ$  and  $90^\circ$ ) for multiple angles of incidence and two optical absorption parameters. The value of the high optical absorption parameter ( $\sigma = 20 \text{ mm}^{-1}$ ) was chosen to match Swank’s example<sup>9</sup> in which  $\sigma T = 2$ . In practice, the optical absorption can be increased by adding an optical dye to the phosphor. Following convention, the polar angle is defined as the angle of the frequency vector relative to the  $x$  axis, so



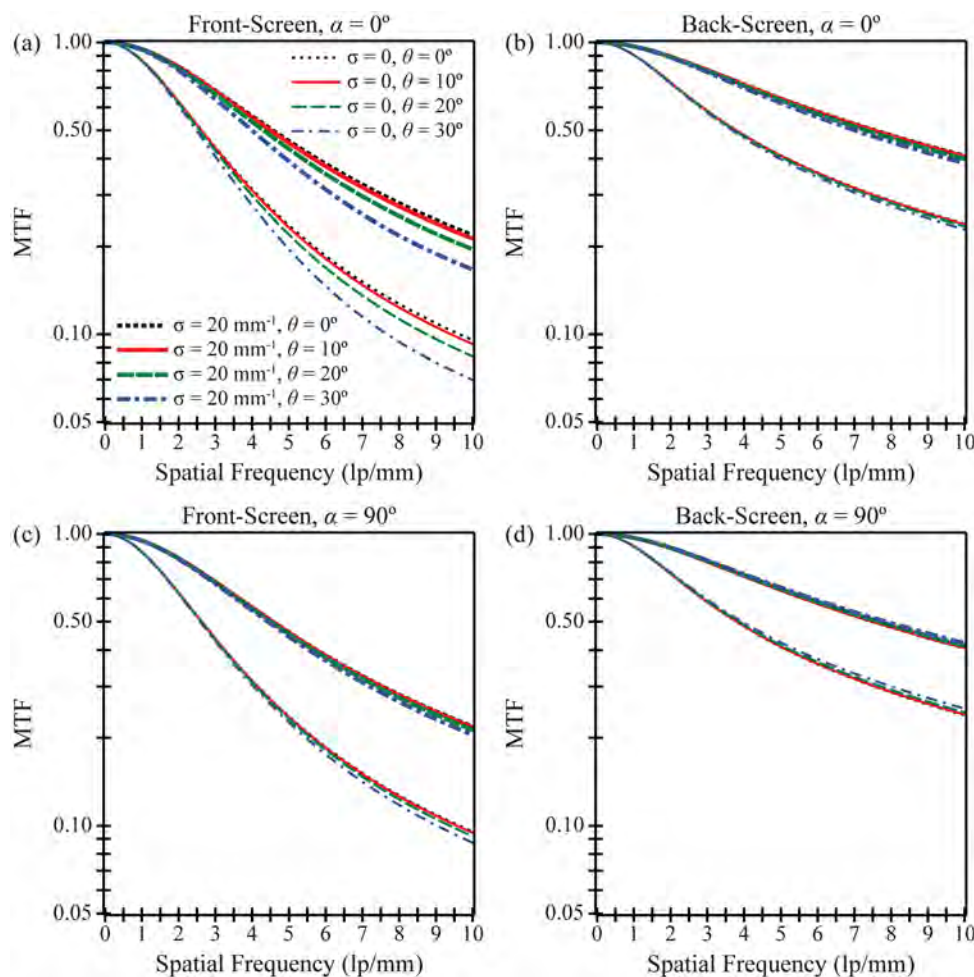


FIG. 2. The modulation transfer function (MTF) of a porous  $\text{Gd}_2\text{O}_2\text{S:Tb}$  phosphor is plotted versus frequency measured along  $0^\circ$  and  $90^\circ$  polar angles for multiple incident angles ( $\theta = 0^\circ, 10^\circ, 20^\circ, 30^\circ$ ) and two optical absorption parameters ( $\sigma = 0, 20 \text{ mm}^{-1}$ ). The scintillator possesses a reflective backing, a nonreflective photocathode, optical scatter at the diffusion limit, and quantum-limited noise. Also, the phosphor thickness is  $100 \mu\text{m}$ , and the incident x-ray energy is 20 keV. As shown, the front-screen configuration has considerably more angular dependence than the back-screen configuration.

that the  $0^\circ$  polar angle is only perpendicular to the x-ray beam for normal incidence and the  $90^\circ$  polar angle is always perpendicular to the x-ray beam (Fig. 1).

Consistent with Swank's work at normal incidence, Fig. 2 demonstrates that increasing the optical absorption increases the MTF. Figure 2(a) indicates that increasing the angle of incidence decreases the MTF, giving rise to poorer spatial resolution in the front-screen configuration. For example, comparing  $30^\circ$  incidence to normal incidence at  $5.0 \text{ lp/mm}$  ( $\alpha = 0^\circ$ ), the MTF decreases by 17% in a phosphor with no optical absorption and by 15% in a phosphor with high optical absorption. As expected, the MTF has minimal angular dependence orthogonal to the ray of incidence [Fig. 2(c)].

Figures 2(b) and 2(d) demonstrate that the back-screen configuration has superior MTF to the front-screen configuration for all projection angles. This result has been well-established for normal incidence.<sup>19,20</sup> More significantly, Figures 2(b) and 2(d) further show that the angular dependence of the MTF is much less pronounced in the back-screen configuration than in the front-screen configuration. For example, comparing  $30^\circ$  incidence to normal incidence at

$5.0 \text{ lp/mm}$  along a  $0^\circ$  polar angle, the back-screen MTF decreases by a mere 3%. Unlike the front-screen, the back-screen MTF increases slightly with projection angle for measurements orthogonal to the incident ray.

In Fig. 3, normalized NPS (NNPS) is plotted versus frequency for the same scintillator. Like MTF, NNPS increases with increasing optical absorption for all angles of incidence. Unlike MTF, NNPS is independent of the directionality of the frequency vector. Over projection angles typical of DBT, the angular dependence of the NNPS is minimal. For example, comparing  $30^\circ$  incidence to normal incidence at  $5.0 \text{ lp/mm}$  in a front-screen configuration, NNPS decreases by 8% in a phosphor with no optical absorption and by 4% in a phosphor with high optical absorption. In a back-screen configuration, NNPS increases slightly by 5% and 2%, respectively.

Figure 4 shows DQE versus frequency. In both a front- and back-screen configuration, Figures 4(a) and 4(b) demonstrate that for measurements made along a  $0^\circ$  polar angle, DQE increases with projection angle at low frequencies and decreases with projection angle at high frequencies. At low frequencies, the angular dependence of the x-ray quantum

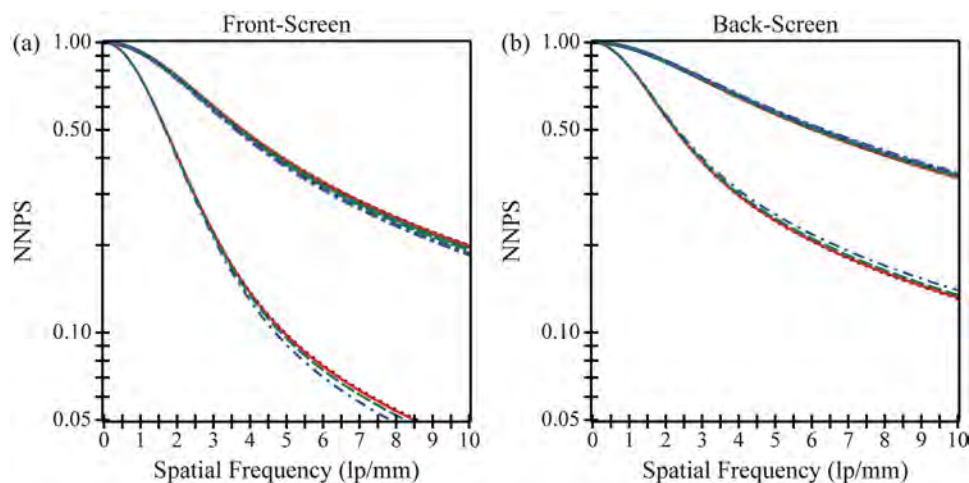


FIG. 3. Normalized noise power spectra (NNPS) is plotted versus frequency. NNPS is independent of the directionality of the frequency vector. While front-screen NNPS decreases with projection angle, back-screen NNPS increases slightly with projection angle. The plots implicitly share a legend with Fig. 2.

detection efficiency ( $A_Q$ ) is responsible for the DQE increase. In calculating  $A_Q$  using Eq. (26), the x-ray path length increases from the phosphor thickness  $T$  with normal

incidence to  $T \sec \theta$  with oblique incidence; hence a greater number of x-rays are converted to visible light. At high frequencies, the degradation in DQE with increasing projection

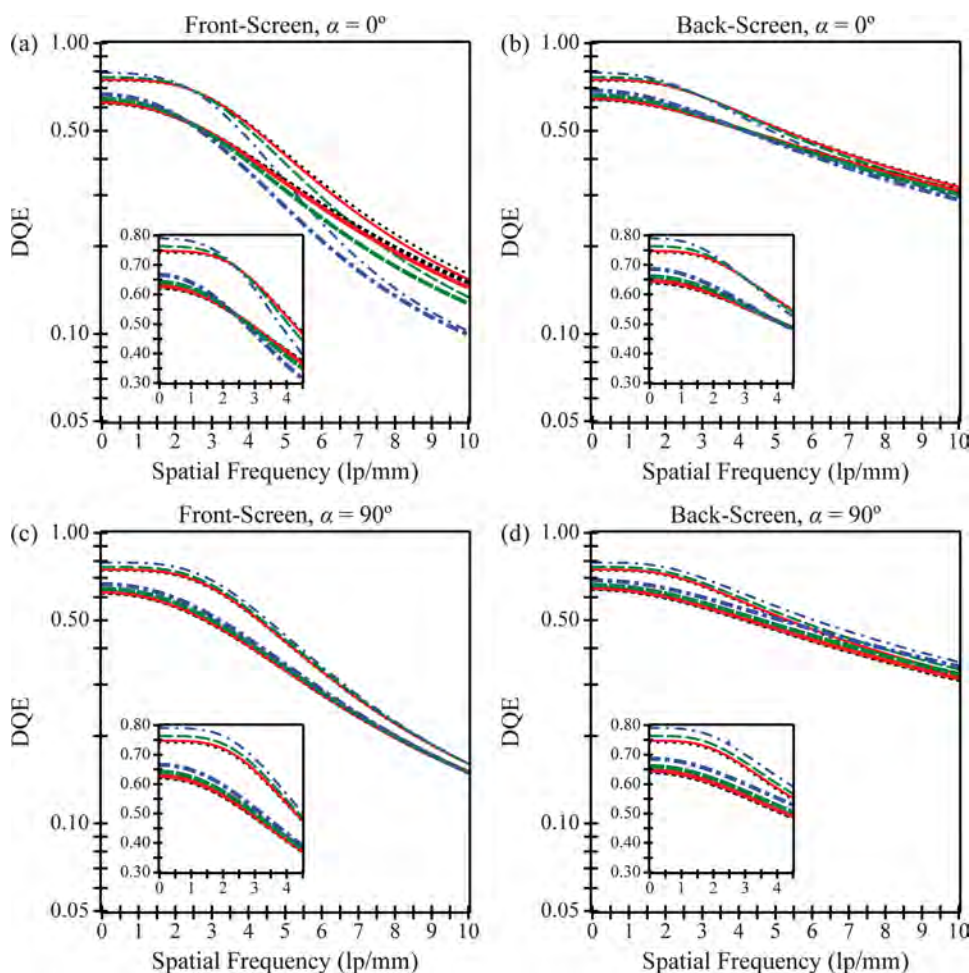


FIG. 4. Detective quantum efficiency (DQE) is plotted versus frequency. Along a  $0^\circ$  polar angle, DQE increases with projection angle at low frequencies and only decreases with projection angle at high frequencies. The front-screen has much more angular dependence than the back-screen at very high frequencies. For measurements orthogonal to the incident ray ( $90^\circ$  polar angle), DQE increases with projection angle over a very broad range of frequencies in both configurations. The plots implicitly share a legend with Fig. 2.

angle arises from the combined angular dependencies of the OTF and NPS. The high frequency DQE for the front-screen configuration is lower than that of the back-screen configuration, and its degradation with projection angle is much more pronounced. For example, at 5.0 lp/mm in a front-screen irradiated at a 30° angle, the DQE decreases by 20% relative to normal incidence. In the back-screen configuration, the relative decrease in DQE is less than 5%.

In the direction orthogonal to the incident ray, DQE increases with projection angle over a very broad range of frequencies [Figs. 4(c) and 4(d)]. Comparing 30° incidence with normal incidence at 5.0 lp/mm in a front-screen configuration, DQE increases by 6% in a phosphor with no optical absorption and by 4% in a phosphor with high optical absorption. Using a back-screen configuration, the relative increase in DQE is approximately twice as high.

In Fig. 5, the angular dependence of the Swank factor ( $A_S$ ) used for calculating the DQE is studied. Swank has shown that  $A_S$  provides a measure of the fluctuation in signal generated from each x-ray photon due to variability in the absorbed energy of each interacting x-ray and in the number of secondary carriers generated from each interacting x-ray.<sup>21</sup> Figure 5 demonstrates that in a phosphor with no optical absorption, the Swank factor is unity at all projection angles for either the front- or back-screen configuration. By contrast, in a phosphor with high optical absorption, the Swank factor has slight angular dependence over projection angles typical of DBT. For example, comparing 30° incidence to normal incidence,  $A_S$  increases by 0.3% in a front-screen configuration and by 0.5% in a back-screen configura-

tion. At very oblique angles approaching shearing incidence ( $\theta = 90^\circ$ ), the Swank factor increases sharply to unity.

Unlike  $A_S$ ,  $DQE(0)$  is projection angle dependent for all possible optical absorption parameters. For both configurations, the relative increase in  $DQE(0)$  comparing 30° incidence to normal incidence is 6% in a phosphor with no optical absorption and 7% in a phosphor with high optical absorption. The angular dependence of  $DQE(0)$  is therefore more pronounced than the Swank factor.

### III.B. Anisotropy of the transfer functions over the detector area

Because the focal spot of a DBT system emits x-rays in all directions, the angle of incidence is spatially variant at each point on the detector. Assuming a stationary detector whose center-of-rotation (COR) coincides with the midpoint of the chest wall, the angle of incidence relative to the normal at each point ( $x, y$ ) on the detector may be determined from the expression

$$\theta = \arctan \left[ \frac{\sqrt{(x - h \sin \Delta)^2 + y^2}}{h \cos \Delta} \right], \quad (32)$$

where  $h$  is the source-to-COR distance and  $\Delta$  is the nominal projection angle (i.e., the angle of the x-ray tube arc relative to the normal at the COR). In deriving this result, the phosphor thickness ( $T$ ) is taken to be negligible compared against the source-to-COR distance ( $h$ ). Also, the chest wall defines the  $x$  axis of the detector and its midpoint the origin. For a  $24 \times 30$  cm field-of-view (FOV) and a source-to-COR distance of 70 cm, the angle  $\theta$  is plotted versus the length ( $x$ ) and the width ( $y$ ) of the detector for the central projection ( $\Delta = 0^\circ$ ) and an oblique projection ( $\Delta = 20^\circ$ ) in Fig. 6. In the central projection [Fig. 6(a)], the angle of incidence relative to the normal varies between  $0^\circ$  and  $25^\circ$ , and in the oblique projection [Fig. 6(b)], it varies between  $10^\circ$  and  $35^\circ$ . For either case, the maximum angle is found at a corner of the FOV opposite the chest wall.

Like the angle of incidence, the transfer functions of the phosphor are spatially variant across the detector area (Fig. 7). To illustrate the spatial anisotropy of one of the transfer functions, a surface plot of front-screen DQE versus position along the detector is shown for the frequency 5.0 lp/mm in a phosphor with high optical absorption assuming a  $0^\circ$  polar angle for the frequency vector. In the central projection [Fig. 7(a)], the front-screen DQE varies between 0.34 and 0.30 (12% decrease), and in the oblique projection [Fig. 7(b)], it varies between 0.33 and 0.24 (27% decrease). Although not plotted in the figure, one can show that the back-screen DQE has much less variation over the detector area in either projection ( $<4\%$  decrease).

### III.C. Optimization of phosphor thickness for oblique incidence

In addition to illustrating the impact of oblique incidence on the transfer functions of a phosphor, the analytical models

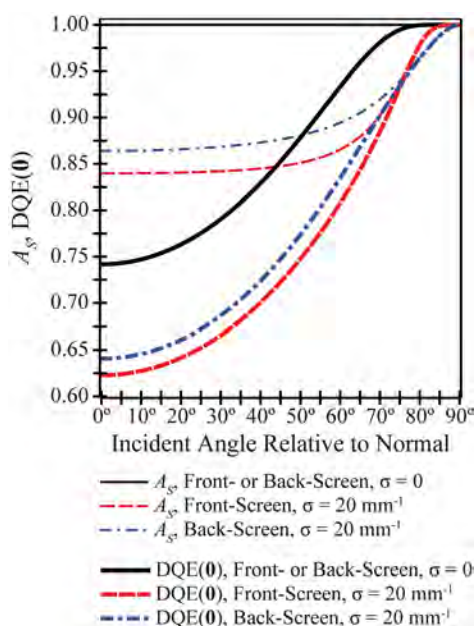


FIG. 5. The Swank information factor ( $A_S$ ) has no angular dependence in a phosphor lacking optical absorption and slight angular dependence over typical incident angles in a phosphor with high optical absorption.  $DQE(0)$  has greater relative variation with incident angle. Both  $A_S$  and  $DQE(0)$  increase sharply to unity at angles approaching shearing incidence ( $\theta = 90^\circ$ ).



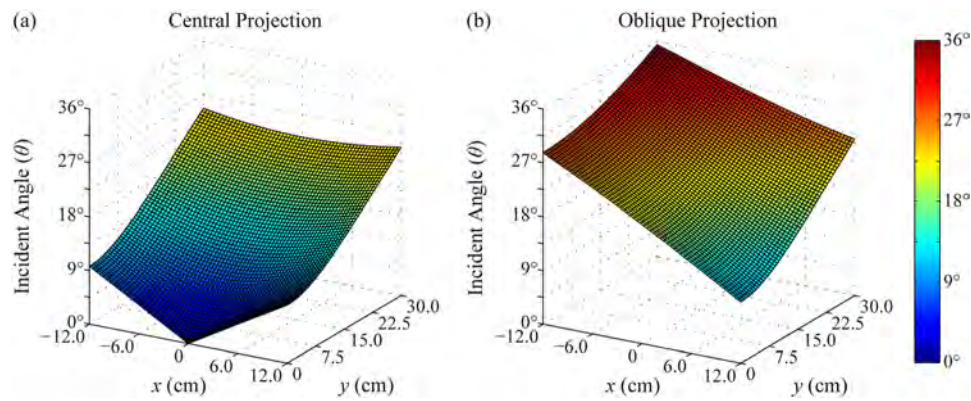


FIG. 6. The angle of incidence relative to the normal is plotted versus position along the detector for (a) the central projection and (b) an oblique projection. The DBT system has a source-to-COR distance of 70 cm, and the nominal projection angle in (b) is 20°.

developed in this work can be used as a platform for optimizing detector design over the range of projection angles used in DBT. One important element in the design of a phosphor is its x-ray quantum detection efficiency (QDE). In Figs. 8 and 9, DQE at a fixed frequency is plotted versus QDE at normal incidence to investigate whether DQE can be maximized by varying QDE. Both figures have been generated using the same phosphor parameters analyzed in Figs. 2–5, except the phosphor thickness  $T$  is now left as a variable which allows QDE at normal incidence to vary.

$$T = \frac{1}{\mu} \cdot \ln\left(\frac{1}{1 - A_{Q0}}\right) \quad (33)$$

In Eq. (33),  $A_{Q0}$  denotes the QDE at normal incidence.

Figure 8 illustrates that in a front- or back-screen configuration with no optical absorption, DQE(0) can be optimized by manufacturing a phosphor with a very large thickness (100% QDE). By contrast, in a phosphor with high optical absorption, the dependency of DQE(0) on QDE is quite different for the two configurations. In a front-screen, DQE(0) is maximized by an intermediate QDE which is projection angle dependent, favoring smaller thicknesses at

larger angles. For example, in the 0° and 30° projections, the optimal QDE at normal incidence are 0.73 and 0.72 corresponding to 97 and 94  $\mu\text{m}$  thicknesses, respectively. By contrast, the back-screen DQE(0) attains relatively high values over a broader range of QDE. With 100% QDE, DQE(0) plateaus to 0.64 and 0.68 for the 0° and 30° projections, respectively.

In Fig. 9, the dependency of DQE on QDE is analyzed at a higher frequency (5.0 lp/mm). The high frequency DQE for the front-screen is maximized at an intermediate QDE for both optical absorption parameters. For measurements made along the 0° polar angle in a front-screen with no optical absorption, the optimal QDE values at normal incidence are 0.60 for the 0° projection and 0.54 for the 30° projection, corresponding to 68 and 58  $\mu\text{m}$  thicknesses, respectively [Fig. 9(a)]. With high optical absorption, the respective QDE optima are 0.55 and 0.51 (59 and 52  $\mu\text{m}$  thicknesses). In the direction orthogonal to the incident ray, the optimal QDE have less projection angle dependence [Fig. 9(c)].

Unlike the front-screen configuration, the back-screen configuration supports relatively high DQE over large QDE values at 5.0 lp/mm. For measurements made along the 0° polar angle [Fig. 9(b)], the back-screen DQE plateaus to

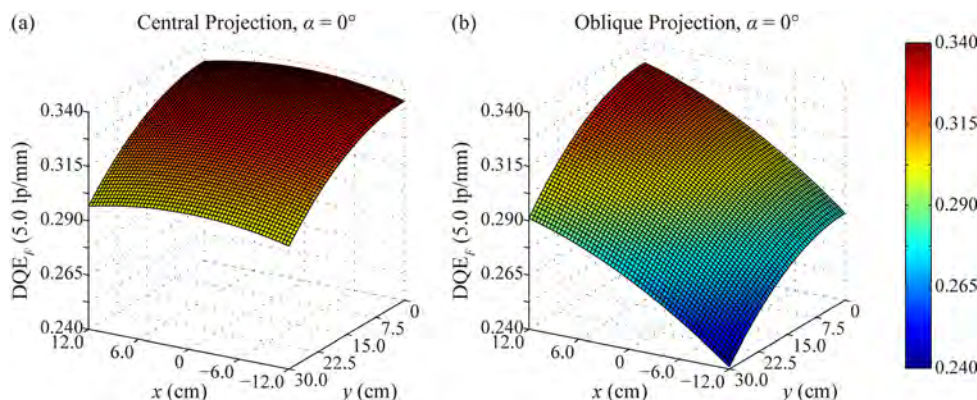


FIG. 7. The anisotropy of the transfer functions over the detector is illustrated by plotting the front-screen DQE at a fixed spatial frequency (5.0 lp/mm) versus areal position, assuming high optical absorption ( $\sigma = 20 \text{ mm}^{-1}$ ) and frequency measurements along a 0° polar angle. The oblique projection has greater variation in DQE over the detector area than the central projection. The directionalities of the  $x$  and  $y$  axes are flipped relative to Fig. 6 to improve visualization of the surfaces.

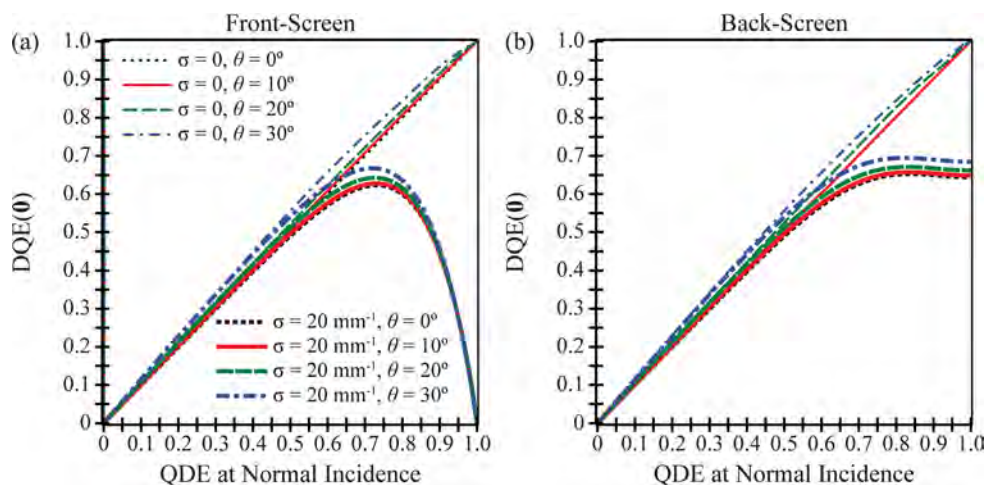


FIG. 8. For four angles of incidence and two optical absorption parameters, the dependency of  $DQE(0)$  on QDE at normal incidence is analyzed. With no optical absorption,  $DQE(0)$  for both front- and back-screen configurations is optimized by large QDE. With high optical absorption, the maximum  $DQE(0)$  for the front-screen occurs at intermediate QDE, while relatively high  $DQE(0)$  for the back-screen occurs over a broad range of large QDE. The optimal QDE for the front-screen is angularly dependent.

0.51 and 0.48 for the  $0^\circ$  and  $30^\circ$  projections, respectively, in a phosphor with no optical absorption (0.46 and 0.45 with high optical absorption). For measurements made along the

orthogonal direction, the back-screen DQE attains a higher plateau; also, the asymptote actually increases slightly with projection angle [Fig. 9(d)].

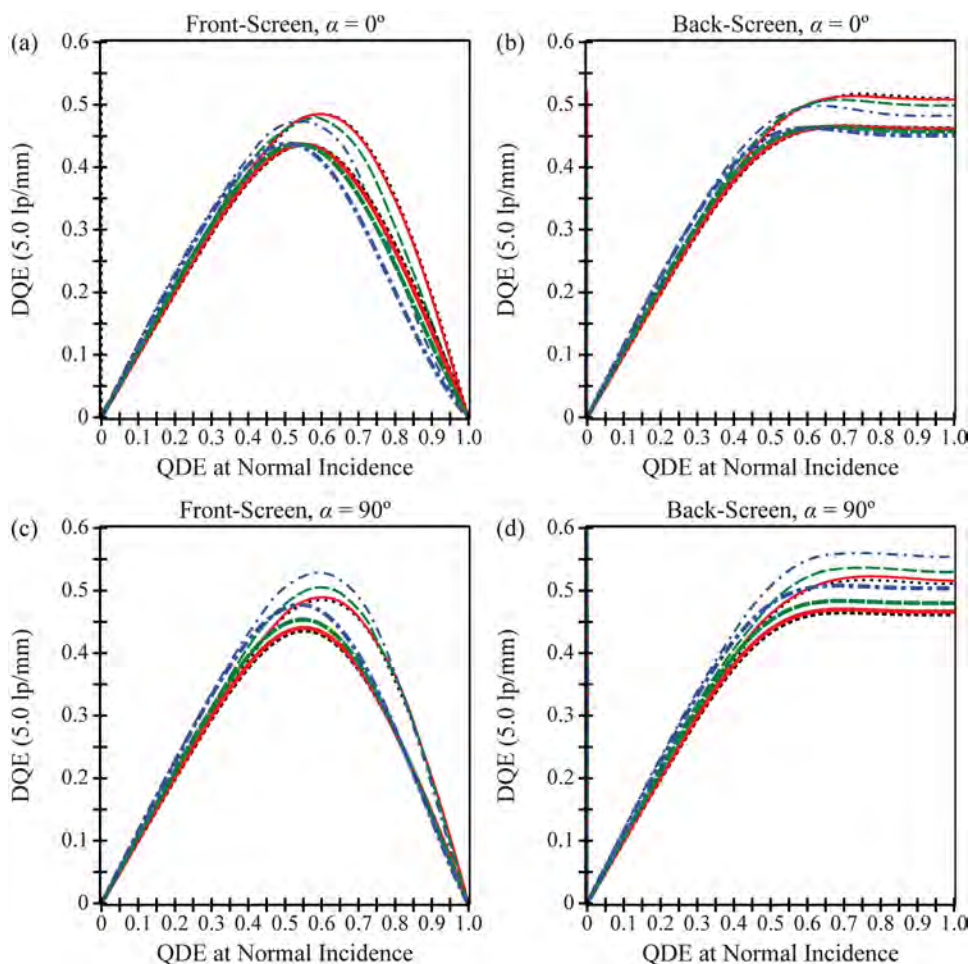


FIG. 9. At 5.0 lp/mm, DQE is plotted versus QDE at normal incidence. In the front-screen configuration, DQE is optimized by an intermediate QDE. The optimal QDE is projection angle dependent, shifting to lower values (thinner phosphors) at larger angles. By contrast, in the back-screen configuration, relatively high DQE is supported over large QDE values for all projection angles. The plots implicitly share a legend with Fig. 8.



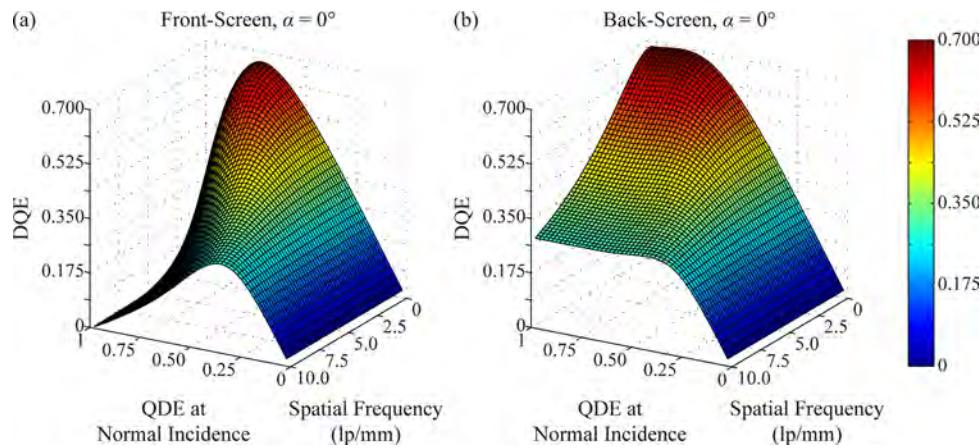


FIG. 10. A surface plot shows the dependence of DQE on both frequency and QDE at normal incidence, assuming  $\theta = 30^\circ$ ,  $\sigma = 20 \text{ mm}^{-1}$ , and a  $0^\circ$  polar angle for the frequency vector. At all frequencies, the front-screen DQE is optimized by an intermediate QDE. By contrast, the back-screen DQE attains relatively high values over a broad range of large QDE (thick phosphors).

To illustrate the dependence of DQE on both frequency and QDE, a surface plot is shown in Fig. 10 assuming  $30^\circ$  incidence, high optical absorption, and frequency measurements along the  $0^\circ$  polar angle. The curvature of the front-screen surface demonstrates that the value of QDE which maximizes DQE decreases with frequency. By contrast, the back-screen surface shows that DQE is not optimized by a single QDE value. Instead, at all frequencies, the back-screen supports relatively high DQE over very large QDE.

Figures 8–10 demonstrate that the optimal thickness of a front-screen is both projection angle dependent and frequency dependent. In Fig. 11, the combined dependence is shown explicitly in a surface plot, assuming a  $0^\circ$  polar angle and high optical absorption. The graph was generated in MATLAB R2010b by discretizing a grid ( $60 \times 60$ ) of incident angles and frequencies from  $0^\circ$  to  $45^\circ$  and 0 to 10 lp/mm, respectively. The optimal thickness which maximizes DQE was determined by the zero of the first partial derivative of DQE with respect to phosphor thickness. Because the zeros of the first DQE derivative cannot be easily solved in closed

form, Newton's method was implemented to find the zeros numerically

$$T_{n+1} = T_n - \frac{\partial D_F}{\partial T} \bigg|_{T=T_n} \cdot \left[ \frac{\partial^2 D_F}{\partial T^2} \bigg|_{T=T_n} \right]^{-1}, \quad n \in \mathcal{N}, \quad (34)$$

where  $D_F$  is the symbolic abbreviation for front-screen DQE. For all projection angles and frequencies investigated in the plot, the initial guess ( $25 \mu\text{m}$ ) and the number of iterations (9) provided convergence exceeding ten decimal places. Figure 11 demonstrates that the optimal phosphor thickness for the front-screen configuration is a decreasing function of both incident angle and frequency, ranging from  $97 \mu\text{m}$  ( $0^\circ$  incidence, 0 lp/mm) to  $25 \mu\text{m}$  ( $45^\circ$  incidence, 10 lp/mm).

#### IV. COMPARISON WITH RESULTS IN THE LITERATURE

This paper extends Swank's calculations<sup>9</sup> of the transfer functions of turbid phosphors to oblique x-ray incidence. In the limiting case of normal incidence, the formulas presented in this paper exactly reduce to Swank's results. Our work is unique in modeling the transfer functions for oblique incidence in closed form without making the assumption that the PSF of normal incidence is a delta function.<sup>1</sup> One benefit of this approach is unifying many prior results on oblique incidence under one model. For example, in a front-screen configuration, we demonstrate that oblique incidence degrades the MTF, and that the resultant loss in resolution becomes more pronounced with increasing frequency and increasing angle. Although these findings are derived for a turbid phosphor such as  $\text{Gd}_2\text{O}_2\text{S:Tb}$ , they are consistent with experimental data on  $\text{CsI:Tl}$  presented by Mainprize *et al.*<sup>8</sup> as well as analytical modeling of  $\alpha$ -Se proposed by Que and Rowlands.<sup>1</sup> On a similar note, we have observed that NPS is degraded with increasing projection angle, though to a lesser degree than MTF. This finding is concordant with the prior work of Hajdok and Cunningham,<sup>3</sup> who performed Monte Carlo simulations of  $\alpha$ -Se. As a final point, we have shown

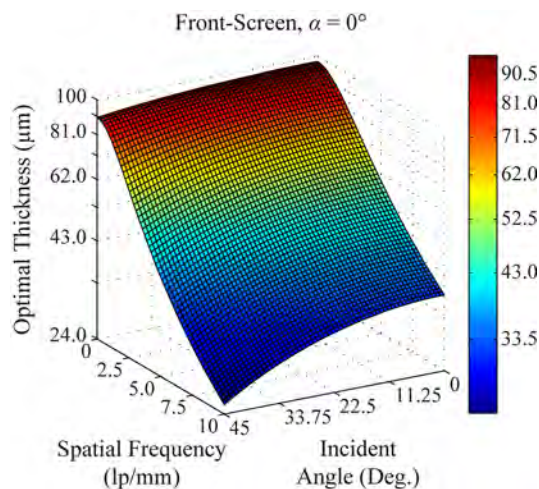


FIG. 11. For a front-screen configuration, the dependence of the optimal phosphor thickness on both the angle of incidence and frequency is analyzed, assuming  $\sigma = 20 \text{ mm}^{-1}$  and a  $0^\circ$  polar angle for the frequency vector.

that DQE increases with incident angle at low frequencies but only decreases with incident angle at high frequencies. Consistent with the findings of Hajdok and Cunningham, the DQE degradation with projection angle at high frequencies is more pronounced than the MTF degradation, reflecting the dependency of DQE on the square of MTF.

In this work, it has been observed that the Swank factor is angularly dependent, but that its variation is small over projection angles typical of DBT. In particular, it has been shown that the Swank factor changes by no more than 0.5% comparing 0° and 30° incidence. This observation is consistent with Monte Carlo simulations of CsI:Tl phosphors conducted by Badano *et al.*, who demonstrated that the variation in the Swank factor over projection angles typical of DBT is minimal.<sup>22</sup> While the relative change in the Swank factor with projection angle is small, the relative increase in  $DQE(0)$  is more substantial, as it includes the effect of increasing x-ray quantum detection efficiency with increasing projection angle.

Although our work demonstrates consistency with other studies on oblique incidence, it is important to identify fundamental differences between the detectors addressed in the comparison. This work models a turbid phosphor in which visible light spreads by optical scatter. By contrast, prior studies on CsI:Tl (Refs. 8 and 22) assume a structured phosphor in which needlelike crystals approximately 10  $\mu\text{m}$  in diameter transmit the optical photons to the photocathode by total internal reflection, thereby minimizing the lateral spread of visible light.<sup>19,23</sup> At a given incident angle, structured phosphors should have higher MTF than turbid phosphors for this reason. Although the transfer functions of turbid phosphors are different from structured phosphors, this work demonstrates that their angular dependence follows comparable trends. On a similar note, our model has shown concordance with prior studies on oblique incidence in *a*-Se.<sup>1,3</sup> In *a*-Se, an absorbed x-ray ionizes a Se atom, freeing an electron and a hole which migrate to different ends of the detector due to an applied electric field.<sup>19</sup> In drift mode, the electric field is small enough so that the electron and hole do not have sufficient kinetic energy to ionize Se atoms and create an avalanche of electron-hole pairs. Because the electron and hole migrate in a nearly perfect orthogonal path to opposite ends of the detector, the MTF of *a*-Se at normal incidence is approximately unity for all frequencies.<sup>2</sup> At higher incident angles, the MTF of *a*-Se decreases with frequency, but is expected to be superior to a turbid phosphor since there is no lateral spread of visible light. The analytical model of *a*-Se developed by Que and Rowlands<sup>1</sup> can effectively be derived by using Eq. (2) for the source function but by eliminating Eq. (1) for the diffusion of secondary carriers.

To our knowledge, this paper is the first to investigate the angular dependence of the transfer functions of the back-screen configuration. The consistency of our back-screen model with expected trends at normal incidence helps to suggest its validity. For example, in accord with experimental data in turbid phosphors,<sup>20</sup> we demonstrate that the back-screen has higher MTF than the front-screen. Because opti-

cal photons are predominately generated near the x-ray entrance surface of the phosphor, visible light exhibits less lateral spread before reaching the photocathode if the back-screen configuration is used.

Consistent with prior authors, this paper demonstrates that the Swank factor of the back-screen is greater than the front-screen. In experimental measurements on  $\text{Gd}_2\text{O}_2\text{S:Tb}$  phosphors at 20 keV, Trauernicht and Van Metter demonstrated that a back-screen has approximately 5% higher Swank factor than a comparable front-screen.<sup>24</sup> Such a relative change in  $A_S$  with screen configuration matches the results presented in Fig. 5. It is evident from Fig. 5 that the benefits of the back-screen over the front-screen should hold with higher incident angles.

## V. DISCUSSION

This study develops an analytical model of the transfer functions of turbid phosphors for oblique x-ray incidence. The results of the model are consistent with prior observations on oblique incidence in a range of detector types. Having an analytical model of the transfer functions has in turn led to the development of optimization strategies for improving detector design in DBT.

One area for optimizing detector design is the choice of a front- or back-screen configuration. Although it is well known that the back-screen has greater MTF than the front-screen at normal incidence, back-screen transfer functions have not yet been analyzed for oblique incidence. In this work, it is suggested that the back-screen transfer functions should have much less angular dependence than the front-screen, and consequently, exhibit less variation with position along the detector. As a result, a back-screen configuration may be chosen to optimize the design of a phosphor for oblique incidence. Initially, this result would seem to have no practical impact, since back-screens are not currently used clinically due to the glass substrate of the thin-film transistor (TFT) array for digital signal readout.<sup>25,27</sup> If these detectors were operated as back-screens, the high attenuation of glass ( $\sim 0.7$  mm thick) would prevent a large percentage of x-rays from reaching the phosphor itself,<sup>19</sup> and hence both QDE and DQE would be compromised. Based on new research on flexible organic light-emitting diode (OLED) displays, however, TFT arrays may soon be manufactured on a plastic substrate.<sup>28,34</sup> Because plastic is much less attenuating than glass, operating such a detector in a back-screen configuration would not be prohibitive. Detectors manufactured with plastic have many benefits such as being bendable, light-weight, and easy to transport. These future phosphor-based detectors should preferentially be operated as back-screens in order to optimize detector performance for oblique incidence.

The analytical model of the transfer functions was ultimately used as a platform for optimizing the QDE of the detector for oblique incidence. This work provides a method for determining the QDE that maximizes DQE at any frequency of interest, such as the frequency of small microcalcifications or fine cancerous lesions within the breast. To our

knowledge, this paper is the first to show that the optimal QDE is projection angle dependent in a front-screen, tending toward lower values (thinner phosphors) with increasing projection angle. Because the incident angle is greatest at the periphery of the detector opposite the chest wall, a corollary of this finding is that one beneficial design feature would be to reduce thickness at the edges and corners of the phosphor. Although it is beyond the scope of this paper to determine a single value for the optimum thickness at each point on a DBT detector, future work should be directed at modeling the transfer functions of the reconstruction<sup>35</sup> and optimizing thickness to maximize the 3D DQE for a fixed frequency of interest. In experimental practice, the optimal thickness should be calculated on a case-by-case basis for each detector under consideration, taking into account the unique characteristics of the imaging system.

In this paper, it was demonstrated that the back-screen DQE is not optimized by a single QDE but instead attains reasonably high values over a broad range of phosphor thicknesses. Hence, the back-screen configuration has an important benefit over the front-screen configuration: future detectors with a plastic TFT substrate can be manufactured with very large thickness without degradation in high frequency DQE at any projection angle.

A discussion of the limitations of this paper and directions for future modeling are now noted. One assumption made in the Results section is that the incident x-ray beam is monoenergetic. Since the phosphor attenuation coefficient  $\mu$  is energy-dependent, it is important to model polyenergetic x-ray spectra<sup>36–38</sup> when studying the phosphor thickness which maximizes DQE in a front-screen (Fig. 11). Future work should be aimed at determining if the angular dependence of the optimal thickness becomes more or less pronounced upon varying the kVp and the target-filter combination. Since Fig. 11 was generated assuming a monoenergetic x-ray beam, the reader should take caution against directly applying the optimal thickness calculations to any real imaging system.

Although a relatively low energy ( $\sim 20$  keV) is conventionally chosen to maximize contrast between glandular tissue and cancer,<sup>4–6</sup> it would be useful to simulate higher energies found in dual energy contrast-enhanced DBT (DE CE-DBT).<sup>39–44</sup> In DE CE-DBT, low and high energy images are acquired below and above the K edge of iodine (33.2 keV) after iodinated contrast is injected into the blood stream,<sup>45,46</sup> and contrast uptake is determined using weighted logarithmic subtraction. Contrast uptake can be used to quantify blood flow at the site of a tumor, which exceeds healthy tissue.<sup>47</sup>

Another extension of this work would be to model detector pixilation due to the TFT array in which the phosphor is placed in optical contact.<sup>25–27</sup> In this setting, the PSF is the convolution of the phosphor blurring function with the detector element sampling function.<sup>48–50</sup> An additional subtlety that may be modeled is the blurring of the focal spot. The MTF of the focal spot is degraded with increasing focal spot size,<sup>51</sup> as well as with increasing focal spot motion during a continuous DBT scan.<sup>35,52</sup> Our model can also be refined by taking into account detector lag and ghosting.<sup>53–55</sup> In addition,

one can incorporate the possibility for an NPS that is not quantum-limited but possesses outside noise sources.<sup>13</sup>

A final point of investigation would be to extend this work to a structured phosphor, such as CsI:Tl. In structured phosphors, needlelike crystals transmit the optical photons to the photocathode by total internal reflection to minimize the lateral spread of visible light. Structured phosphors have superior spatial resolution to nonstructured phosphors for this reason.<sup>19,23</sup> To model a structured phosphor, the boundary conditions for the secondary carrier currents would no longer be determined exclusively by the reflectivities of the backing and the photocathode. Instead, boundary conditions would also exist for the reflectivities of the walls of the needlelike crystals. Recently, Freed *et al.* have proposed an analytical model<sup>56,57</sup> of the PSF of CsI:Tl using a competing approach; their model was later generalized to direct-converting detectors.<sup>58</sup> A key step in the derivation of their PSF formula is considering three different functional forms (Gaussian, exponential, Lorentzian) to quantify the spread of secondary carriers or electron-hole pairs at each depth of the detector material. Empirically, the authors find that the Lorentzian provides the best match to data generated from Monte Carlo simulations. The authors then determine optimal values for the parameters in their model by minimizing the normalized differences between the analytical technique and Monte Carlo simulations. Although useful in providing a closed form solution for the PSF, their model is limited in not being derived from first principles. By contrast, in our current work, all results are derived from first principles, and the value of each parameter has physical significance. It would be intriguing to determine whether our current paper could be generalized to model the boundary conditions of a structured phosphor and have agreement with Freed *et al.*

## VI. CONCLUSION

This work develops analytical models of OTF, NPS, and DQE for a turbid phosphor irradiated obliquely. Our analysis differs from much of the previous work on oblique incidence in that closed form solutions are obtained from first principles, thereby providing greater insight into the underlying detector physics.

Ultimately, the model provides a platform for optimizing the design of DBT detectors. For example, in a conventional front-screen configuration, the model is a useful tool for optimizing phosphor thickness at various angles of incidence. Because the incident angle is spatially variant across the detector area, the potential merit of designing a phosphor with reduced thickness near its periphery has been proposed.

This work demonstrates that the transfer functions of the back-screen have less angular dependence than the front-screen, and that high DQE is supported over a broader range of thicknesses for all incident angles. As a result, future DBT detectors manufactured on a plastic substrate instead of glass should preferentially be operated in the back-screen configuration.



## ACKNOWLEDGMENTS

The authors thank Aldo Badano for a useful background discussion on the impact of oblique incidence on detector performance. The project described was supported by Grant No. T32EB009384 from the National Institute of Biomedical Imaging and Bioengineering (NIBIB). The content is solely the responsibility of the authors and does not necessarily represent the official views of the NIBIB or the National Institutes of Health. Additional support was provided by a pre-doctoral training Grant No. W81XWH-11-1-0100 through the Department of Defense Breast Cancer Research Program.

## NOMENCLATURE

$\partial$  = partial derivative operator.  
 $\nabla^2$  = Laplacian operator.  
 $\in$  = set membership.  
 $\mathcal{L}$  = Laplace transform operator.  
 $\mathcal{N}$  = set of natural numbers.  
 $\alpha$  = polar angle of the 2D spatial frequency vector  $\mathbf{v}$ .  
 $\beta$  = a term defined by Eq. (21) to simplify intermediate calculations.  
 $\gamma_{\pm}$  = a term defined by Eq. (22) to simplify intermediate calculations.  
 $\Delta$  = nominal projection angle.  
 $\delta$  = delta function.  
 $\theta$  = angle of x-ray incidence relative to the normal to the detector.  
 $\mu$  = x-ray linear attenuation coefficient of the phosphor.  
 $\mathbf{v}$  = spatial frequency vector with components  $\nu_x$  and  $\nu_y$ .  
 $\rho_j$  = a quantity defined by Eq. (13) that is related to surface reflectivity. The subscripts  $j = 0, 1$  correspond to the phosphor backing and photocathode, respectively.  
 $\sigma$  = reciprocal of the mean diffusion length of optical photons.  
 $\tau$  = inverse relaxation length (the diffusion limit occurs with  $\tau \rightarrow \infty$ ).  
 $\phi(\mathbf{r})$  = product of photon density and the diffusion constant.  
 $\psi_{\mathbf{k}}(z)$  = Fourier transform of  $\phi(\mathbf{r})$  in a plane of constant  $z$ .  
 $A_Q$  = x-ray quantum detection efficiency.  
 $A_{Q0}$  = x-ray quantum detection efficiency at normal incidence.  
 $A_S$  = Swank information factor.  
 $B$  = back-screen configuration (often used as a subscript).  
 $C_1, C_2$  = constants of integration used in intermediate calculations.  
 $CE$  = contrast-enhanced  
 $COR$  = center-of-rotation of x-ray tube, corresponding to the midpoint of the chest wall side of the detector.  
 $D$  = symbolic abbreviation for detective quantum efficiency.  
 $DBT$  = digital breast tomosynthesis.  
 $DE$  = dual energy

$DM$  = digital mammography.

$DQE$  = detective quantum efficiency.

$F$  = front-screen configuration (often used as a subscript).

$FOV$  = field-of-view.

$G(\mathbf{v})$  = optical transfer function found by summing the contributions of each depth  $z_0$  of the phosphor.

$G(\mathbf{v}, z_0)$  = optical transfer function associated with the depth  $0 \leq z_0 \leq T$  of the phosphor.

$h$  = source-to-COR distance for rotating x-ray tube.

$i$  = imaginary unit given as  $\sqrt{-1}$ .

$j(z)$  = photon currents across any plane of constant  $z$ .

$\mathbf{k}$  = a quantity equivalent to  $2\pi\mathbf{v}$ .

$MTF$  = modulation transfer function.

$n$  = iteration number for Newton's Method.

$NPS$  = noise power spectra.

$N(z_0)$  = relative x-ray signal at the depth  $z_0$  of the phosphor.

$OLED$  = organic light-emitting diode.

$OTF$  = optical transfer function.

$p$  = independent variable of the Laplace transform of a function.

$PSF$  = point spread function.

$q$  = a quantity defined in Eq. (6) to simplify intermediate calculations.

$QDE$  = quantum detection efficiency.

$r_j$  = reflectivity of a surface, where  $j = 0, 1$  correspond to the phosphor backing and photocathode, respectively.

$R_C(\mathbf{v})$  = Lubberts fraction.

$R_N(\mathbf{v})$  = ratio of the quantum noise power to the total noise power.

$S(\mathbf{r})$  = source function, modeled as point-like.

$T$  = phosphor thickness.

$TFT$  = thin-film transistor.

$W(\mathbf{v})$  = noise power spectra.

$x$  = position along the chest wall side of the detector.

$y$  = position perpendicular to the chest wall side of the detector.

$z_0$  = depth within a phosphor (with or without the subscript).

<sup>a)</sup> Author to whom correspondence should be addressed. Electronic mail: Andrew.Maidment@uphs.upenn.edu; Telephone: +1-215-746-8763; Fax: +1-215-746-8764.

<sup>1</sup> W. Que and J. A. Rowlands, "X-ray imaging using amorphous selenium: Inherent spatial resolution," *Med. Phys.* **22**(4), 365–374 (1995).

<sup>2</sup> D. L. Lee, L. K. Cheung, B. Rodricks, and G. F. Powell, "Improved imaging performance of a 14 x 17-inch Direct Radiography (TM) System using Se/TFT detector," *SPIE Conference on Physics of Medical Imaging* (SPIE, San Diego, CA, 1998), p. 14–23.

<sup>3</sup> G. Hajdok and I. A. Cunningham, "Penalty on the Detective Quantum Efficiency from Off-Axis Incident X rays," in *Medical Imaging: Physics of Medical Imaging*, edited by M. J. Yaffe and M. J. Flynn (SPIE, San Diego, 2004), pp. 109–118.

<sup>4</sup> P. C. Johns and M. J. Yaffe, "X-ray Characterization of normal and neoplastic breast tissues," *Phys. Med. Biol.* **32**(6), 675–695 (1987).

<sup>5</sup> M. J. Yaffe, "Digital Mammography," edited by J. Beutel, H. L. Kundel, and R. L. V. Metter, *Handbook of Medical Imaging, Physics and*

- Psychophysics*, (SPIE - The International Society for Optical Engineering, Bellingham, WA, 2000), Vol. 1, Chap. V, pp. 329–372.
- <sup>6</sup>J. T. Bushberg, J. A. Seibert, M. Edwin, J. Leidholdt, and J. M. Boone, "Mammography," 2nd ed., *The Essential Physics of Medical Imaging*, edited by J.-R. John, A. Snyder, T. DeGeorge (Lippincott Williams and Wilkins, Philadelphia, PA, 2002), Chap. VIII, pp. 191–229.
  - <sup>7</sup>E. A. Rafferty, "Tomosynthesis: New weapon in breast cancer fight," *Decisions in Imaging Economics* **17**(4) (2004).
  - <sup>8</sup>J. G. Mainprize, A. K. Bloomquist, M. P. Kempston, and M. J. Yaffe, "Resolution at oblique incidence angles of a flat panel imager for breast tomosynthesis," *Med. Phys.* **33**(9), 3159–3164 (2006).
  - <sup>9</sup>R. K. Swank, "Calculation of modulation transfer functions of x-ray fluorescent screens," *Appl. Opt.* **12**(8), 1865–1870 (1973).
  - <sup>10</sup>R. J. Acciavatti and A. D. A. Maidment, "Calculation of OTF, NPS, and DQE for Oblique X-Ray Incidence on Turbid Granular Phosphors," *Lect. Notes Comput. Sci.* **6136**, 436–443 (2010).
  - <sup>11</sup>R. E. Marshak, H. Brooks, H. Hurwitz, Jr., "Introduction to the theory of diffusion and slowing down of neutrons-I," *Nucleonics* **4**, 10–22 (1949).
  - <sup>12</sup>R. M. Nishikawa and M. J. Yaffe, "Model of the spatial-frequency-dependent detective quantum efficiency of phosphor screens," *Med. Phys.* **17**(5), 894–904 (1990).
  - <sup>13</sup>R. M. Nishikawa and M. J. Yaffe, "Effect of various noise sources on the detective quantum efficiency of phosphor screens," *Med. Phys.* **17**(5), 887–893 (1990).
  - <sup>14</sup>S. M. Lea, "Generalized Functions in Physics," *Mathematics for Physicists*, Brooks/Cole - Thomson Learning, Belmont, CA, 2004, Chap. VI, p. 287–322.
  - <sup>15</sup>H. H. Barrett and K. J. Myers, "Series Expansions and Integral Transforms," *Foundations of Image Science*, edited by B. E. A. Saleh (John Wiley & Sons, New York, 2004), Chap. IV, pp. 175–214.
  - <sup>16</sup>S. M. Lea, "Laplace Transforms," *Mathematics for Physicists* (Brooks/Cole - Thomson Learning, Belmont, CA, 2004) Chap. V, p. 251–286.
  - <sup>17</sup>J. C. Dainty and R. Shaw, Chapter 6: Fourier Transforms, and the Analysis of Image Resolution and Noise. *Image Science*. Academic Press, London, England, 1974. p.190–231.
  - <sup>18</sup>M. J. Berger, *et al.*, "XCOM: Photon Cross Section Database," [cited 2010 December 30]; Available from: <http://physics.nist.gov/xcom>
  - <sup>19</sup>J. A. Rowlands and J. Yorkston, "Flat Panel Detectors for Digital Radiography," *Handbook of Medical Imaging: Physics and Psychophysics*, edited by J. Beutel, H. L. Kundel, R. L. Van Metter (SPIE - The International Society for Optical Engineering, Bellingham, WA, 2000), Vol. 1, Chap. IV, pp. 223–328.
  - <sup>20</sup>I. Kandarakis, D. Cavouras, E. Kanellopoulos, C. D. Nomicos, and G. S. Panayiotakis, "Image quality evaluation of YVO<sub>4</sub>:Eu phosphor screens for use in x-ray medical imaging detectors," *Radiat. Meas.* **29**(5), 481–486 (1998).
  - <sup>21</sup>R. K. Swank, "Absorption and noise in x-ray phosphors," *J. Appl. Phys.* **44**(9), 4199–4203 (1973).
  - <sup>22</sup>A. Badano, I. S. Kyrianiou, and J. Sempau, "Anisotropic imaging performance in indirect x-ray imaging detectors," *Med. Phys.* **33**(8), 2698–2713 (2006).
  - <sup>23</sup>E. Samei, "Image quality in two phosphor-based flat panel digital radiographic detectors," *Med. Phys.* **30**(7), 1747–1757 (2003).
  - <sup>24</sup>D. P. Trauernicht and R. V. Metter, "Conversion noise measurement for front and back x-ray intensifying screens," *SPIE*, **1231**, 262–270 (1990).
  - <sup>25</sup>T. Jing, *et al.*, "Amorphous silicon pixel layers with cesium iodide converters for medical radiography," *IEEE Trans. Nucl. Sci.* **41**(4), 903–909 (1994).
  - <sup>26</sup>A. R. Cowen, S. M. Kengyelics, and A. G. Davies, "Solid-state, flat-panel, digital radiography detectors and their physical imaging characteristics," *Clin. Radiol.* **63**, 487–498 (2008).
  - <sup>27</sup>V. V. Nagarkar, T. K. Gupta, S. R. Miller, Y. Klugerman, M. R. Squillante, G. Entine, "Structured CsI(Tl) scintillators for x-ray imaging applications," *IEEE Trans. Nucl. Sci.* **45**(3), 492–496 (1998).
  - <sup>28</sup>Y. He and J. Kanicki, "High-efficiency organic polymer light-emitting heterostructure devices on flexible plastic substrates," *Appl. Phys. Lett.* **76**(6), 661–663 (2000).
  - <sup>29</sup>M. S. Weaver, *et al.*, "Organic light-emitting devices with extended operating lifetimes on plastic substrates," *Appl. Phys. Lett.* **81**(16), 2929–2931 (2002).
  - <sup>30</sup>K. R. Sarma, *et al.*, *Active Matrix OLED Using 150C a-Si TFT Backplane Built on Flexible Plastic Substrate*, edited by D. Hopper, (SPIE, Orlando, FL, 2003), pp. 180–191.
  - <sup>31</sup>A. Sugimoto, H. Ochi, S. Fujimura, A. Yoshida, T. Miyadera, and M. Tsuchida, "Flexible OLED displays using plastic substrates," *IEEE J. Sel. Top. Quantum Electron.* **10**(1), 107–114 (2004).
  - <sup>32</sup>S. R. Forrest, "The path to ubiquitous and low-cost organic electronic appliances on plastic," *Nature (London)* **428**, 911–918 (2004).
  - <sup>33</sup>A. Nathan, A. Kumar, K. Sakariya, P. Servati, S. Sambandan, and D. Striakhilev, "Amorphous silicon thin film transistor circuit integration for organic LED displays on glass and plastic," *IEEE J. Solid-State Circuits* **39**(9), 1477–1486 (2004).
  - <sup>34</sup>K. Tsukagoshi, J. Tanabe, I. Yagi, K. Shigeto, K. Yanagisawa, and Y. Aoyagi, "Organic light-emitting diode driven by organic thin film transistor on plastic substrates," *J. Appl. Phys.* **99**(6), p. 064506 (2006).
  - <sup>35</sup>B. Zhao and W. Zhao, "Three-dimensional linear system analysis for breast tomosynthesis," *Med. Phys.* **35**(12), 5219–5132 (2008).
  - <sup>36</sup>D. M. Tucker, G. T. Barnes, and D. P. Chakraborty, "Semiempirical model for generating tungsten target x-ray spectra," *Med. Phys.* **18**(2), 211–218 (1991).
  - <sup>37</sup>J. M. Boone, T. R. Fewell, and R. J. Jennings, "Molybdenum, rhodium, and tungsten anode spectral models using interpolating polynomials with application to mammography," *Med. Phys.* **24**(12), 1863–1874 (1997).
  - <sup>38</sup>M. M. Blough, R. G. Waggener, W. H. Payne, and J. A. Terry, Calculated mammographic spectra confirmed with attenuation curves for molybdenum, rhodium, and tungsten targets. *Medical Physics*. 1998; **25**(9):1605–12.
  - <sup>39</sup>A.-K. Carton, J. Li, S. C. Chen, E. F. Conant, and A. D. A. Maidment, "Optimization of contrast-enhanced digital breast tomosynthesis," *Lect. Notes Comput. Sci.* **4046**, 183–189 (2006).
  - <sup>40</sup>S. C. Chen, A. K. Carton, M. Albert, E. F. Conant, M. D. Schnall, and A. D. A. Maidment, "Initial clinical experience with contrast-enhanced digital breast tomosynthesis," *Acad. Radiol.* **14**(2), 229–238 (2007).
  - <sup>41</sup>A. K. Carton, K. Lindman, C. Ullberg, T. Francke, A. D. A. Maidment, "Dual-Energy Contrast Enhanced Digital Breast Tomosynthesis: Concept, Method and Evaluation on Phantoms," *Medical Imaging: Physics of Medical Imaging*, edited by J. Hsieh and M. J. Flynn (SPIE, San Diego, CA, 2007), pp. 1–12.
  - <sup>42</sup>S. Puong, F. Patoureaux, R. Iordache, X. Bouchevreau, and S. Muller, "Dual-Energy Contrast Enhanced Digital Breast Tomosynthesis: Concept, Method and Evaluation on Phantoms," *Medical Imaging: Physics of Medical Imaging*, edited by J. Hsieh and M. J. Flynn (SPIE, San Diego, CA, 2007), pp. 1–12.
  - <sup>43</sup>S. Puong, X. Bouchevreau, N. Duchateau, R. Iordache, and S. Muller, "Optimization of Beam Parameters and Iodine Quantification in Dual-Energy Contrast Enhanced Digital Breast Tomosynthesis," *Medical Imaging: Physics of Medical Imaging*, edited by J. Hsieh and E. Samei (SPIE, San Diego, CA, 2008), pp. 1–11.
  - <sup>44</sup>A. K. Carton, S. C. Gavenonis, J. A. Currian, E. F. Conant, M. D. Schnall, A. D. A. Maidment, "Dual-energy contrast-enhanced digital breast tomosynthesis—A feasibility study," *Br. J. Radiol.* **83**, 344–350 (2010).
  - <sup>45</sup>A.-K. Carton, C. Ullberg, K. Lindman, R. Acciavatti, T. Francke, and A. D. A. Maidment, "Optimization of a dual-energy contrast-enhanced technique for a photon-counting digital breast tomosynthesis system: I. A theoretical model," *Med. Phys.* **37**(11), 5896–5907 (2010).
  - <sup>46</sup>A.-K. Carton, C. Ullberg, and A. D. A. Maidment, "Optimization of a dual-energy contrast-enhanced technique for a photon-counting digital breast tomosynthesis system: II. An experimental validation," *Med. Phys.* **37**(11), 5908–5913 (2010).
  - <sup>47</sup>N. Weidner, J. P. Semple, W. R. Welch, and J. Folkman, "Tumor Angiogenesis and Metastasis—Correlation in invasive breast carcinoma," *N. Engl. J. Med.* **324**, 1–8 (1991).
  - <sup>48</sup>M. Albert and A. D. A. Maidment, "Linear response theory for detectors consisting of discrete arrays," *Med. Phys.* **27**(10), 2417–2434 (2000).
  - <sup>49</sup>R. J. Acciavatti and A. D. A. Maidment, "An Analytical Model of NPS and DQE Comparing Photon Counting and Energy Integrating Detectors," *Physics of Medical Imaging*, edited by E. Samei and N. J. Pelc (SPIE, San Diego, CA, 2010), pp. 1–12.
  - <sup>50</sup>R. J. Acciavatti and A. D. A. Maidment, A comparative analysis of OTF, NPS, and DQE in energy integrating and photon counting digital x-ray detectors," *Med. Phys.* **37**(12), 6480–6495 (2010).

- <sup>51</sup>H. E. Johns and J. R. Cunningham, *Chapter 16: Diagnostic Radiology. The Physics of Radiology*. 4th ed., Charles C Thomas, Springfield, IL, 1983. p.557–669.
- <sup>52</sup>B. Ren, C. Ruth, J. Stein, A. Smith, I. Shaw, and Z. Jing, “Design and Performance of the Prototype Full Field Breast Tomosynthesis System With Selenium Based Flat Panel Detector,” *Medical Imaging: Physics of Medical Imaging*, edited by M. J. Flynn (SPIE, San Diego, CA, 2005), pp. 550–561.
- <sup>53</sup>A. K. Bloomquist, M. J. Yaffe, G. E. Mawdsley, and D. M. Hunter, “Lag and ghosting in a clinical flat-panel selenium digital mammography system,” *Med. Phys.* **33**(8), 2998–3005 (2006).
- <sup>54</sup>J. H. Siewerdsen and D. A. Jaffray, “A ghost story: Spatio-temporal response characteristics of an indirect-detection flat-panel imager,” *Med. Phys.* **26**(8), 1624–1641 (1999).
- <sup>55</sup>W. Zhao, G. DeCrescenzo, S. O. Kasap, and J. A. Rowlands, Ghosting caused by bulk charge trapping in direct conversion flat-panel detectors using amorphous selenium. *Med. Phys.* **32**(2), 488–500 (2005).
- <sup>56</sup>M. Freed, S. Park, and A. Badano, “A fast, angle-independent, analytical model of CsI detector response for optimization of 3D x-ray breast imaging systems,” *Med. Phys.* **37**(6), 2593–2605 (2010).
- <sup>57</sup>M. Freed, S. Park, and A. Badano, “Erratum: “ A fast, angle-dependent, analytical model of CsI detector response for optimization of 3D x-ray breast imaging systems,” *Med. Phys.* **38**(4), 2307 (2011).
- <sup>58</sup>A. Badano, M. Freed, and Y. Fang, “Oblique incidence effects in direct x-ray detectors: A first-order approximation using a physics-based analytical model,” *Med. Phys.* **38**(4), 2095–2098 (2011)

# **Optimization of In-Plane Resolution in Digital Breast Tomosynthesis Using Super-Resolution Image Reconstruction**

Raymond J. Acciavatti and Andrew D. A. Maidment, Ph.D.

*Department of Radiology  
Perelman School of Medicine at the University of Pennsylvania  
Philadelphia, Pennsylvania*

Abbreviated Title: Super-Resolution in Digital Breast Tomosynthesis

Contact Information:

Andrew D. A. Maidment, Ph.D. FAAPM

Perelman School of Medicine at the University of Pennsylvania

Department of Radiology – Physics Section

1 Silverstein Building

3400 Spruce Street

Philadelphia, PA 19104-4206, USA

Voice: 215-746-8763

Fax: 215-746-8764

Email: Andrew.Maidment@uphs.upenn.edu

## **ABSTRACT**

45 **Purpose:** Digital breast tomosynthesis (DBT) is a 3D x-ray imaging modality in which tomographic sections of the breast are generated from a limited range of tube angles. Because oblique x-ray incidence shifts the image of an object in sub-pixel detector element increments with each increasing projection angle, it is demonstrated that DBT is capable of super-resolution (*i.e.* sub-pixel resolution).

50 **Methods:** By convention, DBT reconstructions are performed on planes parallel to the breast support at various depths of the breast volume. In order for resolution in each reconstructed slice to be comparable to the detector, the pixel size should match that of the detector elements; hence, the highest frequency that can be resolved in the plane of reconstruction is the alias frequency of the detector. This study considers reconstruction grids with much smaller pixilation to visualize higher

55 frequencies. For analytical proof of super-resolution, a theoretical framework is developed in which the reconstruction of a high frequency sinusoidal input is calculated using both simple backprojection (SBP) and filtered backprojection (FBP). To study the frequency spectrum of the reconstruction, its Fourier transform is also calculated. The experimental feasibility of super-resolution was investigated using a commercial DBT system (Selenia Dimensions, Hologic,

60 Bedford, MA) and a commercial prototype reconstruction solution (Briona<sup>TM</sup>, Real Time Tomography, Villanova, PA). Images of bar patterns with frequencies higher than the detector alias frequency were acquired and subsequently reconstructed. To demonstrate the clinical importance of super-resolution, the visibility of microcalcifications was compared among reconstruction grids of varying sizes.

65 **Results:** Using analytical modeling, it is shown that the central projection cannot resolve frequencies exceeding the detector alias frequency. The Fourier transform of the central projection is maximized at a lower frequency than the input as evidence of aliasing. By contrast, SBP

reconstruction can resolve the input, and its Fourier transform is correctly maximized at the input frequency. Incorporating filters into the reconstruction smoothens pixilation artifacts in the spatial domain and reduces spectral leakage in the Fourier domain. In addition, it is demonstrated that the feasibility of super-resolution is dependent on the directionality of the input frequency. Super-resolution is achievable over a broad range of positions for frequencies parallel to the chest wall side of the breast support, but is feasible only at certain positions for frequencies perpendicular to the chest wall. At the latter orientation of the input frequency, super-resolution is achievable at positions sufficiently displaced from: (1) the chest wall, and (2) the mid plane perpendicular to the chest wall and to the breast support. Consistent with the analytical results, experimental reconstructions of bar patterns showed visibility of frequencies greater than the detector alias frequency. For the two orientations of the bar patterns, super-resolution was present at positions predicted from analytical modeling. Ultimately, super-resolution was found to improve the visibility of fine morphological details of microcalcifications in select examples of clinical DBT images.

**Conclusions:** This work demonstrates the feasibility of super-resolution in DBT, and has applications in the visualization of microcalcifications and other subtle signs of breast cancer.

**Key words:** Digital breast tomosynthesis (DBT), super-resolution, bar pattern phantom, microcalcifications, filtered backprojection (FBP).

## **I. INTRODUCTION**

Digital breast tomosynthesis (DBT) is a 3D imaging modality in which low dose x-ray projections are acquired over a limited angular range about the breast. Using digital image reconstruction techniques, tomographic sections at all depths of the breast volume are subsequently generated. Unlike 2D digital mammography (DM), DBT can filter out overlapping anatomical structures which may hide a tumor. Early clinical trials indicate that DBT has greater sensitivity and specificity for early cancer detection relative to DM.<sup>1</sup>

In conventional practice, the reconstructed slices are generated on planes parallel to the breast support. In order to have the same in-plane resolution in the reconstruction as the detector, the pixel size in each reconstructed slice should match that of the detector elements. Using this approach, the highest frequency that can be resolved in the plane of reconstruction is the alias frequency of the detector. This study considers the possibility for reconstruction grids with much smaller pixilation so that higher frequencies can be visualized. Because non-normal x-ray incidence causes the image of an object to be translated in sub-pixel detector element increments with each increasing projection angle, it is demonstrated in this work that DBT is capable of super-resolution (*i.e.*, sub-pixel resolution).

Super-resolution has been well-described in a number of applications involving reconstruction from projections,<sup>2</sup> including forensics, satellite imaging, computed tomography (CT), and magnetic resonance imaging (MRI); however, to our knowledge, its potential in DBT has not yet been explored. An understanding of super-resolution and an analysis of how to optimize its presence may prove to be useful for designing the highest quality DBT systems. Although it is possible to improve spatial resolution simply by reducing the pixel size of the detector, there are practical lower limits on the sizes that can be manufactured. In addition, one drawback of reducing the pixel size is decreasing the mean number of photons incident on each detector element and

hence decreasing the signal-to-noise ratio (SNR) per pixel according to Poisson statistics<sup>3</sup> for x-ray distributions. Clinically, super-resolution should be beneficial to diagnostic radiologists by improving the visibility of microcalcifications and other subtle signs of breast cancer with no increased radiation dose to the patient.

120 In this study, a theoretical framework for investigating super-resolution in DBT is developed by calculating the reconstruction of a sine input whose frequency is greater than the alias frequency of the detector. For optimal visualization of high frequencies in the 3D image, an infinitesimally fine (*i.e.*, non-pixelated) reconstruction grid is considered. The reconstruction techniques include both simple backprojection (SBP) and filtered backprojection (FBP). In order to investigate the  
125 experimental feasibility of super-resolution using a commercial DBT system, images of a bar pattern phantom with frequencies higher than the alias frequency of the detector were acquired and subsequently reconstructed. In addition, clinical images of microcalcifications were analyzed, and differences in the visibility of microcalcifications were examined on various reconstruction grid sizes.

## 130 II. METHODS

### II. A. Input Object and Acquisition Geometry

An analytical framework for investigating the potential for super-resolution in DBT is now developed by calculating the reconstruction of a high frequency sinusoidal input. Accordingly,  
135 suppose that a rectangular prism with infinite extent in the  $x$  and  $y$  directions has a linear attenuation coefficient  $\mu(x, y, z)$  which varies sinusoidally along the  $x$  direction with frequency  $f_0$ . Throughout the remainder of this manuscript, the input object will be termed a “*sine plate*”. With the  $xz$  plane defining the chest wall, the frequency vector is therefore oriented parallel to the chest wall side of the breast support. Figure 1 illustrates a cross section of the sine plate in the  $xz$  plane. As shown,



140 the rectangular prism is positioned between  $z = z_0 + \varepsilon/2$  and  $z = z_0 - \varepsilon/2$ , where  $z_0$  is the central height of the prism and  $\varepsilon$  is the prism's thickness. Defining the origin O as the midpoint of the chest wall side of the detector, the attenuation coefficient may be written as

$$\mu(x, y, z) = C \cdot \cos[2\pi f_0(x - x_0)] \cdot \text{rect}\left(\frac{z - z_0}{\varepsilon}\right), \quad (1)$$

where  $C$  is a constant denoting the amplitude of the waveform,  $x_0$  is a translational shift in the  
145 waveform relative to the origin, and the rect function is defined by the expression

$$\text{rect}(u) \equiv \begin{cases} 1 & , |u| \leq 1/2 \\ 0 & , |u| > 1/2 \end{cases}. \quad (2)$$

By setting the amplitude  $C$  to  $1/\varepsilon$ ,  $\mu(x, y, z)$  may be normalized<sup>4</sup> so that the total attenuation found by integrating along the  $z$  direction is simply  $\cos[2\pi f_0(x - x_0)]$  for all  $\varepsilon$ . Provided that  $|z - z_0| \leq \varepsilon$ , the 1D Fourier transform ( $\mathcal{F}_1$ ) of Eq. (1) along the  $x$  direction peaks at the frequencies  $f_x = \pm f_0$ , and  
150 vanishes at all other frequencies.<sup>5</sup>

$$\mathcal{F}_1\mu(f_x, y, z) = \int_{-\infty}^{\infty} \mu(x, y, z) \cdot e^{-2\pi i f_x x} dx \quad (3)$$

$$= \frac{C}{2} \left[ e^{-2\pi i f_0 x_0} \delta(f_x - f_0) + e^{2\pi i f_0 x_0} \delta(f_x + f_0) \right] \cdot \text{rect}\left(\frac{z - z_0}{\varepsilon}\right) \quad (4)$$

Typically, only the positive frequency  $f_x = +f_0$  is of interest in a physical measurement. Thus, although it is non-physical for an attenuation coefficient to vary between negative and positive  
155 values, formulating  $\mu(x, y, z)$  by Eq. (1) is helpful for a thought experiment in interrogating the reconstruction of a single input frequency. An analysis of the case for which the input frequency is oriented along the  $y$  direction (*i.e.*, perpendicular to the chest wall) is considered separately in Appendix A.

The most general DBT acquisition geometry with a divergent x-ray beam and a rotating  
160 detector is now modeled. In acquiring the  $n^{\text{th}}$  projection, the focal spot emits x rays at the nominal

projection angle  $\psi_n$  relative to the center-of-rotation (COR) of the DBT system. The COR and the focal spot lie in the plane of the chest wall. In addition, the detector rotates about the  $y$  axis at the angle  $\gamma_n$  relative to the  $x$  direction. The two parameters  $\psi_n$  and  $\gamma_n$  are determined from the nominal angular spacing  $\Delta\psi$  and the detector gear ratio  $g$  by the relations

$$165 \quad \psi_n = n \cdot \Delta\psi \quad (5)$$

$$\gamma_n = \frac{\psi_n}{g}. \quad (6)$$

For an odd number of  $N$  total projections, the index  $n$  varies between  $-(N-1)/2$  and  $(N-1)/2$ , and the special case  $n = 0$  defines the central projection.

As a final step in this section, it is useful to calculate the incident angle at each point on the detector. Following Figure 2, the vector from O to an arbitrary point C on the detector for the  $n^{\text{th}}$  projection is

$$\overrightarrow{OC} = u_1 \mathbf{i}'_n + u_2 \mathbf{j}'_n \quad (7)$$

$$= (u_1 \cos \gamma_n) \mathbf{i} + u_2 \mathbf{j} + (u_1 \sin \gamma_n) \mathbf{k}. \quad (8)$$

The matrix transformation between the primed and unprimed coordinate systems supports the transition from Eq. (7) to Eq. (8).

$$\begin{pmatrix} \mathbf{i}'_n \\ \mathbf{j}'_n \\ \mathbf{k}'_n \end{pmatrix} = \begin{pmatrix} \cos \gamma_n & 0 & \sin \gamma_n \\ 0 & 1 & 0 \\ -\sin \gamma_n & 0 & \cos \gamma_n \end{pmatrix} \begin{pmatrix} \mathbf{i} \\ \mathbf{j} \\ \mathbf{k} \end{pmatrix} \quad (9)$$

Additional vectors from O to the COR at point B and from the COR to the focal spot at point A are

$$\overrightarrow{OB} = l \mathbf{k} \quad (10)$$

$$\overrightarrow{BA} = (-h \sin \psi_n) \mathbf{i} + (h \cos \psi_n) \mathbf{k}, \quad (11)$$

180 where  $l$  is the distance between O and the COR. In Eq. (11), it is assumed that for positive values of  $\psi_n$ , the  $x$  component of the displacement of the focal spot at A relative to the COR at B is negative.

This sign convention is chosen so that positive values of  $\psi_n$  cause the  $x$  component of the trajectory from A to C to be positive for positive values of  $u_1$  (Figure 2). By the summation rules for vectors, the net vector from point C on the detector to the focal spot at A is

$$\overrightarrow{CA} = -\overrightarrow{OC} + \overrightarrow{OB} + \overrightarrow{BA} \quad (12)$$

$$= -(u_1 \cos \gamma_n + h \sin \psi_n) \mathbf{i} - u_2 \mathbf{j} + (l + h \cos \psi_n - u_1 \sin \gamma_n) \mathbf{k} . \quad (13)$$

Thus the angle of incidence is found from the expression

$$\cos \theta_n = \frac{\overrightarrow{CA} \cdot \mathbf{k}'_n}{|\overrightarrow{CA}| |\mathbf{k}'_n|}, \quad (14)$$

giving

$$\theta_n = \arccos \left[ \frac{h \cos(\psi_n - \gamma_n) + l \cos \gamma_n}{\sqrt{(u_1 \cos \gamma_n + h \sin \psi_n)^2 + u_2^2 + (l + h \cos \psi_n - u_1 \sin \gamma_n)^2}} \right]. \quad (15)$$

The dot product in Eq. (14) has been computed using Eq. (9) to write  $\mathbf{k}'_n$  in terms of the unprimed unit vectors.

## II. B. Detector Signal

To calculate the detector signal for each projection, it is useful to perform ray tracing through the input object. We begin by defining the line from the focal spot at A to the incident point on the detector at C for the  $n^{\text{th}}$  projection. This line can be expressed as the parametric equation

$$\begin{pmatrix} x \\ y \\ z \end{pmatrix} = w \begin{pmatrix} u_1 \cos \gamma_n + h \sin \psi_n \\ u_2 \\ u_1 \sin \gamma_n - l - h \cos \psi_n \end{pmatrix} + \begin{pmatrix} -h \sin \psi_n \\ 0 \\ l + h \cos \psi_n \end{pmatrix}, \quad (16)$$

where  $(x, y, z)$  is a point in  $\mathbb{R}^3$  and  $w$  is a free parameter. The focal spot at A has been defined to correspond with  $w = 0$ , while the incident point at C has been defined to correspond with  $w = 1$ .

The x-ray path length  $\mathcal{L}_n$  through the input object for the  $n^{\text{th}}$  projection image is determined from the intersection of Eq. (16) with the planes  $z = z_0 + \varepsilon/2$  and  $z = z_0 - \varepsilon/2$ . The values of  $w$  for these two points are

$$w_n^+ = \frac{z_0 + (\varepsilon/2) - l - h \cos \psi_n}{u_1 \sin \gamma_n - l - h \cos \psi_n} \quad (17)$$

$$w_n^- = \frac{z_0 - (\varepsilon/2) - l - h \cos \psi_n}{u_1 \sin \gamma_n - l - h \cos \psi_n}, \quad (18)$$

where  $w_n^+$  and  $w_n^-$  correspond to the entrance and exit points of the x-ray through the input, respectively. For the  $n^{\text{th}}$  projection image, total x-ray attenuation  $\mathcal{A}\mu(n)$  is now found by integrating  $\mu(x, y, z)$  along  $\mathcal{L}_n$ .

$$\mathcal{A}\mu(n) = \int_{\mathcal{L}_n} \mu ds \quad (19)$$

The differential arc length  $ds$  along  $\mathcal{L}_n$  is

$$ds = \sqrt{\left(\frac{dx}{dw}\right)^2 + \left(\frac{dy}{dw}\right)^2 + \left(\frac{dz}{dw}\right)^2} dw \quad (20)$$

$$= \sqrt{(u_1 \cos \gamma_n + h \sin \psi_n)^2 + u_2^2 + (l + h \cos \psi_n - u_1 \sin \gamma_n)^2} dw \quad (21)$$

$$= [h \cos(\psi_n - \gamma_n) + l \cos \gamma_n] \sec(\theta_n) \cdot dw. \quad (22)$$

Eq. (22) follows from Eq. (15). Substituting Eq. (22) into Eq. (19) yields the total x-ray attenuation

$$\mathcal{A}\mu(n) = \kappa_n \int_{w_n^+}^{w_n^-} \cos[2\pi f_0(u_1 \cos \gamma_n + h \sin \psi_n)w + \lambda_n] dw \quad (23)$$

$$= \frac{\kappa_n \left( \sin[2\pi f_0(u_1 \cos \gamma_n + h \sin \psi_n)w_n^- + \lambda_n] - \sin[2\pi f_0(u_1 \cos \gamma_n + h \sin \psi_n)w_n^+ + \lambda_n] \right)}{2\pi f_0(u_1 \cos \gamma_n + h \sin \psi_n)}$$

$$(24)$$

where

$$\kappa_n = C[h \cos(\psi_n - \gamma_n) + l \cos \gamma_n] \sec \theta_n \quad (25)$$

$$\lambda_n = -2\pi f_0(h \sin \psi_n + x_0). \quad (26)$$

Using a sum-to-product trigonometric identity for real numbers  $b_1$  and  $b_2$

$$\sin(b_1) - \sin(b_2) = 2 \cos\left(\frac{b_1 + b_2}{2}\right) \sin\left(\frac{b_1 - b_2}{2}\right), \quad (27)$$

one may rewrite Eq. (24) as

$$\mathcal{A}\mu(n) = \kappa_n (w_n^- - w_n^+) \cos\left[\pi f_0(u_1 \cos \gamma_n + h \sin \psi_n)(w_n^+ + w_n^-) + \lambda_n\right] \text{sinc}\left[f_0(u_1 \cos \gamma_n + h \sin \psi_n)(w_n^- - w_n^+)\right] \quad (28)$$

$$= \frac{\varepsilon \kappa_n \cos\left[\frac{2\pi f_0(l + h \cos \psi_n - z_0)(u_1 \cos \gamma_n + h \sin \psi_n)}{l + h \cos \psi_n - u_1 \sin \gamma_n} + \lambda_n\right] \text{sinc}\left[\frac{\varepsilon f_0(u_1 \cos \gamma_n + h \sin \psi_n)}{l + h \cos \psi_n - u_1 \sin \gamma_n}\right]}{l + h \cos \psi_n - u_1 \sin \gamma_n} \quad (29)$$

where

$$\text{sinc}(u) \equiv \frac{\sin(\pi u)}{\pi u}. \quad (30)$$

The transition from Eq. (28) to (29) follows from Eqs. (17) and (18). Eq. (29) possesses a singularity at  $u_1 = (l + h \cos \psi_n) \csc \gamma_n$ , the point at which the denominator vanishes. For typical acquisition geometries, this singularity is not expected to correspond to a position on the detector, since neither the attenuation coefficient  $\mu(x, y, z)$  nor the path length  $\mathcal{L}_n$  should have an infinity.

Eq. (29) provides an expression for signal intensity versus position along the detector, assuming that the detector is non-pixelated and possesses an x-ray converter whose modulation transfer function (MTF) is unity at all frequencies. An amorphous selenium (*a*-Se) photoconductor operated in drift mode is a good approximation for an x-ray converter with these properties.<sup>6</sup> In a

clinical setting,  $a$ -Se is placed in contact with a plate of amorphous silicon ( $a$ -Si) in which a thin-  
 240 film transistor (TFT) array samples detector signal in pixels (*i.e.*, detector elements).<sup>7-9</sup> The  
 logarithmically-transformed signal in the  $\mathbf{m}^{\text{th}}$  detector element for the  $n^{\text{th}}$  projection is

$$\mathcal{D}\mu(\mathbf{m}, n) = \int_{a_y m_y}^{a_y(m_y+1)} \int_{a_x(m_x-1/2)}^{a_x(m_x+1/2)} \mathcal{A}\mu(n) \cdot \frac{du_1}{a_x} \frac{du_2}{a_y}. \quad (31)$$

In Eq. (31),  $m_x$  and  $m_y$  are integers used for labeling detector elements, and  $a_x$  and  $a_y$  denote detector  
 element lengths in the directions parallel and perpendicular to the chest wall, respectively. In the  
 245 special case of square detector elements, it is assumed that  $a_x = a_y = a$ . Detector elements are  
 centered on  $u_1 = m_x a_x$  and  $u_2 = (m_y + 1/2)a_y$ , where  $m_x \in \mathbb{Z}$  and  $m_y \in \mathbb{Z}^*$ .

It is important to note that the integrand in Eq. (31) is dependent on both  $u_1$  and  $u_2$  due to the  
 dependency of  $\kappa_n$  [Eq. (25)] on the incident angle  $\theta_n$  [Eq. (15)]. However, because  $\theta_n$  should vary  
 minimally within the area of a single detector element, total attenuation can be well approximated  
 250 by the expression

$$\tilde{\mathcal{A}}\mu(n) = \mathcal{A}\mu(n) \Big|_{\theta_n = \theta_{\mathbf{mn}}}, \quad (32)$$

where  $\theta_{\mathbf{mn}}$  is the evaluation of  $\theta_n$  at the centroid of the  $\mathbf{m}^{\text{th}}$  detector element

$$\theta_{\mathbf{mn}} \equiv \theta_n \Big|_{(u_1, u_2) = (m_x a_x, [m_y + 1/2] a_y)}, \quad (33)$$

so that

$$\mathcal{D}\mu(\mathbf{m}, n) \cong \int_{a_x(m_x-1/2)}^{a_x(m_x+1/2)} \tilde{\mathcal{A}}\mu(n) \cdot \frac{du_1}{a_x}. \quad (34)$$

Because it would be difficult to evaluate Eq. (34) in closed form, it is appropriate to apply  
 approximate integration techniques. One such method is the midpoint formula<sup>10</sup>

$$\mathcal{D}\mu(\mathbf{m}, n) \cong \lim_{J_x \rightarrow \infty} \frac{1}{J_x} \sum_{j_x=1}^{J_x} \tilde{\mathcal{A}}\mu(j_x, n), \quad (35)$$

where



$$\tilde{\mathcal{A}}\mu(j_x, n) \equiv \tilde{\mathcal{A}}\mu(n) \Big|_{u_1 = a_x \left( \frac{j_x - 1/2}{J_x} + m_x - \frac{1}{2} \right)}. \quad (36)$$

The raw signal  $\mathcal{S}\mu(u_1, u_2)$  across the detector can now be determined for the  $n^{\text{th}}$  projection as

$$\mathcal{S}\mu(u_1, u_2) = \sum_{\mathbf{m}} \mathcal{D}\mu(\mathbf{m}, n) \cdot \text{rect} \left( \frac{u_1 - m_x a_x}{a_x} \right) \cdot \text{rect} \left( \frac{u_2 - (m_y + 1/2) a_y}{a_y} \right). \quad (37)$$

Using this expression for raw signal, it is now possible to calculate the x-ray transform<sup>11</sup>  $\mathcal{X}\mu(t_1, t_2)$ .

$$\mathcal{X}\mu(t_1, t_2) = \sum_{\mathbf{m}} \mathcal{D}\mu(\mathbf{m}, n) \cdot \text{rect} \left( \frac{t_1 \sec \theta_{\mathbf{m}n} - m_x a_x}{a_x} \right) \cdot \text{rect} \left( \frac{t_2 \sec \theta_{\mathbf{m}n} - (m_y + 1/2) a_y}{a_y} \right) \quad (38)$$

To justify the transition from Eq. (37) to Eq. (38), one must determine the affine parameters  $t_1$  and  $t_2$  in terms of  $u_1$  and  $u_2$  by considering a line segment  $\overline{\text{OD}}$  which is orthogonal to  $\overline{\text{AC}}$  and which connects the origin with the x-ray beam (Figure 2). From trigonometry, the length  $|\mathbf{t}| = \sqrt{t_1^2 + t_2^2}$  of  $\overline{\text{OD}}$  is

$$|\mathbf{t}| = |\mathbf{u}| \cos \theta_n. \quad (39)$$

By generalizing Eq. (39) to components, one finds  $t_1 = u_1 \cos \theta_n$  and  $t_2 = u_2 \cos \theta_n$ . In Eq. (38), the incident angle across the area of the  $\mathbf{m}^{\text{th}}$  detector element for the  $n^{\text{th}}$  projection has been approximated by its value at the centroid.

## II. C. Filtered Backprojection (FBP) Reconstruction from the Projections

The reconstructed attenuation coefficient can now be determined by filtering the x-ray transform with the function  $\phi(t_1, t_2)$  and backprojecting the result along the ray of incidence.<sup>12</sup> It is customary to apply filtering exclusively to frequencies within the plane of the x-ray tube motion, so that the filter's 2D Fourier transform  $\mathcal{F}_2 \phi(f_1, f_2)$  is independent of  $f_2$

$$\mathcal{F}_2\phi(f_1, f_2) = \mathcal{F}_1\phi(f_1), \quad (40)$$

280 and hence

$$\phi(t_1, t_2) = \phi(t_1)\delta(t_2). \quad (41)$$

The specific formula for  $\phi(t_1)$  will be addressed in the next section. Assuming that the reconstruction grid is infinitesimally fine (*i.e.*, non-pixelated), the filtered backprojection (FBP) reconstruction is

$$\begin{aligned} \mu_{\text{FBP}} = \sum_{\mathbf{m}, n} \frac{\mathcal{D}\mu(\mathbf{m}, n)}{N} \cdot & \left[ \phi(t_1) * \text{rect} \left( \frac{t_1 \sec \theta_{\mathbf{m}n} - m_x a_x}{a_x} \right) \right]_{t_1 = x'_n \cos \theta_{\mathbf{m}n} + z'_n \cos(\Gamma_{\mathbf{m}n}) \sin(\theta_{\mathbf{m}n})} \\ & \cdot \left[ \text{rect} \left( \frac{t_2 \sec \theta_{\mathbf{m}n} - (m_y + 1/2) a_y}{a_y} \right) \right]_{t_2 = y'_n \cos \theta_{\mathbf{m}n} + z'_n \sin(\Gamma_{\mathbf{m}n}) \sin(\theta_{\mathbf{m}n})}, \end{aligned} \quad (42)$$

where  $\mu_{\text{FBP}}$  is the reconstructed attenuation coefficient and  $*$  is the convolution operator. Within the plane of the detector, backprojection of signal in the  $\mathbf{m}^{\text{th}}$  detector element for the  $n^{\text{th}}$  projection is directed azimuthally along the angle  $\Gamma_{\mathbf{m}n}$  relative to the  $\mathbf{i}_n'$  axis (Figure 2). As shown in Eq. (42), backprojection may be performed for each of the  $N$  projections using the primed coordinate system. To evaluate Eq. (42) at the point  $(x, y, z)$  in the unprimed coordinate system, one applies the matrix transformation given in Eq. (9).

It is now important to illustrate how the azimuthal backprojection angle  $\Gamma_{\mathbf{m}n}$  is calculated. Begin by considering an arbitrary point E along the x-ray beam at which signal is backprojected from the incident point C (Figure 2). A line segment along the  $\mathbf{k}_n'$  direction may then be drawn from E to the point F on the detector for the  $n^{\text{th}}$  projection. As a result, within the plane of the detector, backprojection is directed from C to F at the angle  $\Gamma_n$  relative to the  $\mathbf{i}_n'$  axis. Point G may now be defined as the position at the chest wall side of the detector which is collinear with points C

and F. A derivation of the formula for  $\Gamma_n$  requires knowledge of the distance  $d_n$  between G and O, which is now calculated.

$$\overrightarrow{GO} = d_n \mathbf{i}'_n \quad (43)$$

$$= (d_n \cos \gamma_n) \mathbf{i} + (d_n \sin \gamma_n) \mathbf{k} \quad (44)$$

Since ACG and ECF are similar triangles,  $\overrightarrow{GA}$  is parallel to  $\overrightarrow{FE}$  and is in turn parallel to  $\mathbf{k}_n'$ .

Denoting  $\times$  as the cross product operator, it follows that

$$\overrightarrow{GA} \times \mathbf{k}_n' = \mathbf{0}, \quad (45)$$

305 where

$$\overrightarrow{GA} = \overrightarrow{GO} + \overrightarrow{OA} \quad (46)$$

$$= (d_n \cos \gamma_n - h \sin \psi_n) \mathbf{i} + (d_n \sin \gamma_n + l + h \cos \psi_n) \mathbf{k}. \quad (47)$$

To calculate  $\overrightarrow{OA}$  in Eq. (46), Eqs. (10) and (11) have been summed. Substituting Eqs. (9) and (47) into the cross product of Eq. (45) gives

$$\overrightarrow{GA} \times \mathbf{k}_n' = \begin{vmatrix} \mathbf{i} & \mathbf{j} & \mathbf{k} \\ d_n \cos \gamma_n - h \sin \psi_n & 0 & d_n \sin \gamma_n + l + h \cos \psi_n \\ -\sin \gamma_n & 0 & \cos \gamma_n \end{vmatrix} \quad (48)$$

$$= -[d_n + l \sin \gamma_n - h \sin(\psi_n - \gamma_n)] \mathbf{j}. \quad (49)$$

By combining Eqs. (45) and (49), one can solve for  $d_n$ .

$$d_n = h \sin(\psi_n - \gamma_n) - l \sin \gamma_n \quad (50)$$

Using this result, it follows from trigonometry that

$$\cos \Gamma_n = \frac{u_1 + d_n}{\sqrt{(u_1 + d_n)^2 + u_2^2}} \quad (51)$$

$$\sin \Gamma_n = \frac{u_2}{\sqrt{(u_1 + d_n)^2 + u_2^2}}. \quad (52)$$

Substituting the coordinates of the detector element centroid into Eqs. (51)-(52), one finds that the azimuthal backprojection angle for the  $\mathbf{m}^{\text{th}}$  detector element in the  $n^{\text{th}}$  projection satisfies the properties

$$\cos \Gamma_{\mathbf{m}n} = \frac{m_x a_x + d_n}{\sqrt{(m_x a_x + d_n)^2 + (m_y + 1/2)^2 a_y^2}} \quad (53)$$

$$\sin \Gamma_{\mathbf{m}n} = \frac{(m_y + 1/2) a_y}{\sqrt{(m_x a_x + d_n)^2 + (m_y + 1/2)^2 a_y^2}}. \quad (54)$$

These relations are the expressions needed for FBP reconstruction in Eq. (42). One special case of Eq. (42) is simple backprojection (SBP) reconstruction

$$\mathcal{B}(\chi\mu) = \sum_{\mathbf{m},n} \frac{\mathcal{D}\mu(\mathbf{m},n)}{N} \cdot \text{rect} \left( \frac{x'_n + z'_n \cos(\Gamma_{\mathbf{m}n}) \tan(\theta_{\mathbf{m}n}) - m_x a_x}{a_x} \right) \cdot \text{rect} \left( \frac{y'_n + z'_n \sin(\Gamma_{\mathbf{m}n}) \tan(\theta_{\mathbf{m}n}) - (m_y + 1/2) a_y}{a_y} \right), \quad (55)$$

where  $\mathcal{B}$  denotes the backprojection operator. With SBP, the filter  $\phi(t_1, t_2)$  effectively becomes the product  $\delta(t_1)\delta(t_2)$ . According to Eq. (55), backprojection in the primed coordinate system occurs by translating  $x'_n$  and  $y'_n$  by  $-z'_n \cos(\Gamma_{\mathbf{m}n}) \tan(\theta_{\mathbf{m}n})$  and  $-z'_n \sin(\Gamma_{\mathbf{m}n}) \tan(\theta_{\mathbf{m}n})$ , respectively, where  $z'_n$  is the height of the backprojected point (E) above the plane of the detector. These translational shifts are illustrated in Figure 2.

## II. D. Formulation of the Reconstruction Filter

Following Zhao's linear systems theory for DBT,<sup>13</sup> a ramp (RA) filter should be applied to the x-ray transform of each projection to reduce the low frequency detector response.<sup>14</sup> The filter is truncated at the spatial frequencies  $f_1 = -\zeta$  and  $f_1 = +\zeta$  in the Fourier domain.

$$\mathcal{F}_1 \phi_{\text{RA}}(f_1) = \begin{cases} |f_1| & , |f_1| \leq \xi \\ 0 & , |f_1| > \xi \end{cases} \quad (56)$$

The spatial representation  $\phi_{\text{RA}}(t_1)$  of the RA filter is determined by its inverse Fourier transform.<sup>5</sup>

$$\phi_{\text{RA}}(t_1) = \int_{-\infty}^{\infty} \mathcal{F}_1 \phi_{\text{RA}}(f_1) \cdot e^{2\pi i t_1 f_1} df_1 \quad (57)$$

$$= \xi^2 \left[ 2\text{sinc}(2\xi t_1) - \text{sinc}^2(\xi t_1) \right] \quad (58)$$

Using this result, the convolution in Eq. (42) can be calculated.

$$\phi_{\text{RA}}(t_1) * \text{rect}\left(\frac{t_1 \sec \theta_{\text{mn}} - m_x a_x}{a_x}\right) = \frac{\left[ a_x \cos(\theta_{\text{mn}}) \left[ \cos(\pi a_x \xi \cos \theta_{\text{mn}}) \cos[2\pi \xi (t_1 - m_x a_x \cos \theta_{\text{mn}})] - 1 \right] + 2(t_1 - m_x a_x \cos \theta_{\text{mn}}) \sin(\pi a_x \xi \cos \theta_{\text{mn}}) \sin[2\pi \xi (t_1 - m_x a_x \cos \theta_{\text{mn}})] \right]}{2\pi^2 [t_1 - (m_x - 1/2)a_x \cos \theta_{\text{mn}}][t_1 - (m_x + 1/2)a_x \cos \theta_{\text{mn}}]} \quad (59)$$

Since noise tends to occur at high frequencies, a spectrum apodization (SA) filter is often applied in addition to the RA filter in order to reduce the high frequency detector response. Following Zhao's approach, a Hanning window function is the SA filter.

$$\mathcal{F}_1 \phi_{\text{SA}}(f_1) = \begin{cases} \frac{1}{2} \left[ 1 + \cos\left(\frac{\pi f_1}{\xi}\right) \right] & , |f_1| \leq \xi \\ 0 & , |f_1| > \xi \end{cases} \quad (60)$$

$$\phi_{\text{SA}}(t_1) = \frac{\xi \text{sinc}(2\xi t_1)}{1 - 4\xi^2 t_1^2} \quad (61)$$

According to the convolution theorem,<sup>5</sup> the net filter is thus

$$\phi_{\text{SA}}(t_1) * \phi_{\text{RA}}(t_1) = \frac{\xi^2 \left[ \pi^2 (12\xi^2 t_1^2 - 1) \text{sinc}^2(\xi t_1) - 2\pi^2 (4\xi^2 t_1^2 - 1) \text{sinc}(2\xi t_1) - 4(4\xi^2 t_1^2 + 1) \right]}{2\pi^2 (4\xi^2 t_1^2 - 1)^2} \quad (62)$$

The convolution of the net filter in Eq. (62) with the rect function in Eq. (42) can be performed in

closed form similar to Eq. (59). This expression is omitted as it is lengthy.

## II. E. Fourier Transform of the DBT Images

According to Eq. (4), the Fourier transform of the input along the  $x$  direction peaks at the  
 355 frequencies  $f_x = \pm f_0$ . To determine whether the frequency spectra of the DBT images possess this  
 expected dependency on  $f_0$ , their continuous Fourier transforms may be considered. Within the  
 plane of the detector, the 2D Fourier transform of the  $n^{\text{th}}$  projection is

$$\mathcal{F}_2(\mathcal{S}\mu)(f_1, f_2) = \int_{-\infty}^{\infty} \int_{-\infty}^{\infty} \mathcal{S}\mu(u_1, u_2) \cdot e^{-2\pi i(f_1 u_1 + f_2 u_2)} du_1 du_2 \quad (63)$$

$$= a_x a_y \cdot \text{sinc}(a_x f_1) \text{sinc}(a_y f_2) \cdot \sum_{\mathbf{m}} \mathcal{D}\mu(\mathbf{m}, n) \cdot e^{-2\pi i[m_x a_x f_1 + (m_y + 1/2) a_y f_2]}. \quad (64)$$

360 The 2D Fourier transform of the reconstruction along the  $x$  and  $y$  directions may now be calculated  
 by considering a fixed height  $z$ . Because this study only considers input frequencies parallel to the  
 $xy$  plane, it is unnecessary to transform along the  $z$  direction. Although filtered backprojection  
 reconstruction in Eq. (42) is performed in the primed coordinate system, it is important to take the  
 Fourier transform in the unprimed coordinated system. As such, the reconstructed attenuation  
 365 coefficient can be written in the form

$$\mu_{\text{FBP}}(x, y, z) = \sum_{\mathbf{m}, n} \frac{\mathcal{D}\mu(\mathbf{m}, n)}{N} \cdot [\rho_1(t_1)]|_{t_1 = \sigma_{1\mathbf{m}n}x + \sigma_{2\mathbf{m}n}z} \cdot [\rho_2(t_2)]|_{t_2 = \sigma_{3\mathbf{m}n}x + \sigma_{4\mathbf{m}n}y + \sigma_{5\mathbf{m}n}z}, \quad (65)$$

where

$$\rho_1(t_1) = \phi(t_1) * \text{rect}\left(\frac{t_1 \sec \theta_{\mathbf{m}n} - m_x a_x}{a_x}\right) \quad (66)$$

$$\rho_2(t_2) = \text{rect}\left(\frac{t_2 \sec \theta_{\mathbf{m}n} - (m_y + 1/2) a_y}{a_y}\right), \quad (67)$$

370 and

$$\sigma_{1\mathbf{m}n} = \cos(\gamma_n) \cos(\theta_{\mathbf{m}n}) - \cos(\Gamma_{\mathbf{m}n}) \sin(\gamma_n) \sin(\theta_{\mathbf{m}n}) \quad (68)$$

$$\sigma_{2\mathbf{m}n} = \sin(\gamma_n) \cos(\theta_{\mathbf{m}n}) + \cos(\Gamma_{\mathbf{m}n}) \cos(\gamma_n) \sin(\theta_{\mathbf{m}n}) \quad (69)$$

$$\sigma_{3\mathbf{m}l} = -\sin(\Gamma_{\mathbf{m}l})\sin(\gamma_n)\sin(\theta_{\mathbf{m}l}) \quad (70)$$

$$\sigma_{4\mathbf{m}l} = \cos\theta_{\mathbf{m}l} \quad (71)$$

$$375 \quad \sigma_{5\mathbf{m}l} = \sin(\Gamma_{\mathbf{m}l})\cos(\gamma_n)\sin(\theta_{\mathbf{m}l}) . \quad (72)$$

According to the convolution theorem, the Fourier transform of Eq. (66) under the frequency variable  $f_1$  is

$$\mathcal{F}_1\rho_1(f_1) = \mathcal{F}_1\phi(f_1) \cdot a_x \cos(\theta_{\mathbf{m}l})\text{sinc}(a_x f_1 \cos\theta_{\mathbf{m}l})e^{-2\pi i m_x a_x f_1 \cos\theta_{\mathbf{m}l}} . \quad (73)$$

In the special case of SBP reconstruction, the filter in Eq. (73) is unity. In a similar fashion, the

380 Fourier transform of Eq. (67) may be written

$$\mathcal{F}_1\rho_2(f_2) = a_y \cos(\theta_{\mathbf{m}l})\text{sinc}(a_y f_2 \cos\theta_{\mathbf{m}l})e^{-2\pi i (m_y+1/2)a_y f_2 \cos\theta_{\mathbf{m}l}} . \quad (74)$$

The 2D Fourier transform of Eq. (65) at the fixed depth  $z$  is now determined from the expression

$$\mathcal{F}_2\mu_{\text{FBP}}(f_x, f_y, z) = \sum_{\mathbf{m}, l} \frac{\mathcal{D}\mu(\mathbf{m}, l)}{N} \cdot \int_{-\infty}^{\infty} \rho_1(\sigma_{1\mathbf{m}l}x + \sigma_{2\mathbf{m}l}z) \cdot I_{y\mathbf{m}l}(x) \cdot e^{-2\pi i f_x x} dx , \quad (75)$$

where  $I_{y\mathbf{m}l}(x)$  is given by the integral

$$385 \quad I_{y\mathbf{m}l}(x) = \int_{-\infty}^{\infty} \rho_2(\sigma_{3\mathbf{m}l}x + \sigma_{4\mathbf{m}l}y + \sigma_{5\mathbf{m}l}z) \cdot e^{-2\pi i f_y y} dy . \quad (76)$$

To evaluate Eq. (76), one can make the change of variables  $\eta_{y\mathbf{m}l} = \sigma_{3\mathbf{m}l}x + \sigma_{4\mathbf{m}l}y + \sigma_{5\mathbf{m}l}z$ . Since

$\sigma_{4\mathbf{m}l} > 0$ , it follows that

$$I_{y\mathbf{m}l}(x) = \int_{-\infty}^{\infty} \rho_2(\eta_{y\mathbf{m}l}) e^{\frac{-2\pi i f_y (\eta_{y\mathbf{m}l} - \sigma_{3\mathbf{m}l}x - \sigma_{5\mathbf{m}l}z)}{\sigma_{4\mathbf{m}l}}} \frac{d\eta_{y\mathbf{m}l}}{\sigma_{4\mathbf{m}l}} \quad (77)$$

$$= \frac{e^{\frac{2\pi i f_y (\sigma_{3\mathbf{m}l}x + \sigma_{5\mathbf{m}l}z)}{\sigma_{4\mathbf{m}l}}}}{\sigma_{4\mathbf{m}l}} \int_{-\infty}^{\infty} \rho_2(\eta_{y\mathbf{m}l}) e^{-2\pi i \left(\frac{f_y}{\sigma_{4\mathbf{m}l}}\right) \eta_{y\mathbf{m}l}} d\eta_{y\mathbf{m}l} \quad (78)$$

$$390 \quad = \frac{e^{\frac{2\pi i f_y (\sigma_{3\mathbf{m}l}x + \sigma_{5\mathbf{m}l}z)}{\sigma_{4\mathbf{m}l}}}}{\sigma_{4\mathbf{m}l}} \mathcal{F}_1\rho_2\left(\frac{f_y}{\sigma_{4\mathbf{m}l}}\right), \quad (79)$$



where  $\mathcal{F}_1\rho_2$  has been previously calculated in Eq. (74). Using Eq. (79), Eq. (75) can now be rewritten as

$$\mathcal{F}_2\mu_{\text{FBP}}(f_x, f_y, z) = \sum_{\mathbf{m}, n} \frac{\mathcal{D}\mu(\mathbf{m}, n)}{N} \frac{e^{\frac{2\pi i f_y \sigma_{5\mathbf{m}n} z}{\sigma_{4\mathbf{m}n}}} I_{x\mathbf{m}n}}{\sigma_{4\mathbf{m}n}} \mathcal{F}_1\rho_2\left(\frac{f_y}{\sigma_{4\mathbf{m}n}}\right), \quad (80)$$

where

$$I_{x\mathbf{m}n} = \int_{-\infty}^{\infty} \rho_1(\sigma_{1\mathbf{m}n}x + \sigma_{2\mathbf{m}n}z) e^{-2\pi i \left(f_x - \frac{\sigma_{3\mathbf{m}n}f_y}{\sigma_{4\mathbf{m}n}}\right)x} dx. \quad (81)$$

To evaluate Eq. (81), it is helpful to perform the substitution  $\eta_{x\mathbf{m}n} = \sigma_{1\mathbf{m}n}x + \sigma_{2\mathbf{m}n}z$ .

$$I_{x\mathbf{m}n} = \int_{-\infty}^{\infty} \rho_1(\eta_{x\mathbf{m}n}) e^{-2\pi i \left(f_x - \frac{\sigma_{3\mathbf{m}n}f_y}{\sigma_{4\mathbf{m}n}}\right) \left(\frac{\eta_{x\mathbf{m}n} - \sigma_{2\mathbf{m}n}z}{\sigma_{1\mathbf{m}n}}\right)} \frac{d\eta_{x\mathbf{m}n}}{|\sigma_{1\mathbf{m}n}|} \quad (82)$$

$$= \frac{e^{\frac{2\pi i \sigma_{2\mathbf{m}n} z (\sigma_{4\mathbf{m}n} f_x - \sigma_{3\mathbf{m}n} f_y)}{\sigma_{1\mathbf{m}n} \sigma_{4\mathbf{m}n}}}}{|\sigma_{1\mathbf{m}n}|} \int_{-\infty}^{\infty} \rho_1(\eta_{x\mathbf{m}n}) e^{-2\pi i \left(\frac{\sigma_{4\mathbf{m}n} f_x - \sigma_{3\mathbf{m}n} f_y}{\sigma_{1\mathbf{m}n} \sigma_{4\mathbf{m}n}}\right) \eta_{x\mathbf{m}n}} d\eta_{x\mathbf{m}n} \quad (83)$$

$$= \frac{e^{\frac{2\pi i \sigma_{2\mathbf{m}n} z (\sigma_{4\mathbf{m}n} f_x - \sigma_{3\mathbf{m}n} f_y)}{\sigma_{1\mathbf{m}n} \sigma_{4\mathbf{m}n}}}}{|\sigma_{1\mathbf{m}n}|} \mathcal{F}_1\rho_1\left(\frac{\sigma_{4\mathbf{m}n} f_x - \sigma_{3\mathbf{m}n} f_y}{\sigma_{1\mathbf{m}n} \sigma_{4\mathbf{m}n}}\right) \quad (84)$$

where  $\mathcal{F}_1\rho_1$  is given by Eq. (73). The final expression for the 2D Fourier transform of the reconstruction can now be derived by combining Eqs. (80) and (84).

$$\mathcal{F}_2\mu_{\text{FBP}}(f_x, f_y, z) = \sum_{\mathbf{m}, n} \frac{\mathcal{D}\mu(\mathbf{m}, n)}{N} \frac{e^{\frac{2\pi i z}{\sigma_{1\mathbf{m}n} \sigma_{4\mathbf{m}n}} [\sigma_{2\mathbf{m}n} \sigma_{4\mathbf{m}n} f_x + (\sigma_{1\mathbf{m}n} \sigma_{5\mathbf{m}n} - \sigma_{2\mathbf{m}n} \sigma_{3\mathbf{m}n}) f_y]}}{|\sigma_{1\mathbf{m}n}| \sigma_{4\mathbf{m}n}} \mathcal{F}_1\rho_1\left(\frac{\sigma_{4\mathbf{m}n} f_x - \sigma_{3\mathbf{m}n} f_y}{\sigma_{1\mathbf{m}n} \sigma_{4\mathbf{m}n}}\right) \mathcal{F}_1\rho_2\left(\frac{f_y}{\sigma_{4\mathbf{m}n}}\right) \quad (85)$$

A special case of this result is important to consider.

$$\mathcal{F}_2\mu_{\text{FBP}}(f_x, 0, z) = \sum_{\mathbf{m}, n} \frac{\mathcal{D}\mu(\mathbf{m}, n)}{N} \frac{e^{\frac{2\pi i \sigma_{2\mathbf{m}n} z f_x}{\sigma_{1\mathbf{m}n}}} a_y \cos \theta_{\mathbf{m}n}}{|\sigma_{1\mathbf{m}n}| \sigma_{4\mathbf{m}n}} \mathcal{F}_1\rho_1\left(\frac{f_x}{\sigma_{1\mathbf{m}n}}\right) \quad (86)$$

Eq. (86) is useful for analyzing the reconstruction of an input frequency oriented along the  $x$  direction; that is,  $f_y = 0$ .

### 410 **III. RESULTS**

#### **III. A. Input Frequency Directed Parallel to the Chest Wall Side of the Breast Support**

Image acquisition is now simulated for a Selenia Dimensions integrated multi-mode mammography and tomosynthesis x-ray system (Hologic Inc., Bedford, MA) having 15 projections, an angular spacing ( $\Delta\psi$ ) of  $1.07^\circ$  between projections, a source-to-COR distance ( $h$ ) of 70.0 cm, a  
415 COR-to-origin distance ( $l$ ) of 0 cm, and square detector element length ( $a_x = a_y = a$ ) of  $140\ \mu\text{m}$ . In addition, the sine plate has a thickness ( $\varepsilon$ ) of 0.5 mm, a translational shift ( $x_0$ ) of 0 mm along the direction of the chest wall side of the breast support, and a frequency ( $f_0$ ) of  $0.7a^{-1}$  (5.00 lp/mm) parallel to the  $x$  axis. To illustrate DBT's potential for super-resolution, the input frequency is specified to be higher than the detector alias frequency  $0.5a^{-1}$  (3.57 lp/mm). The sine plate is placed  
420 at a height corresponding to the mid-thickness of a typical breast size (50.0 mm thick) under compression. With the breast support positioned 25.0 mm above the origin of the detector, the sine plate is therefore positioned at the height  $z_0 = 50.0$  mm.

FBP reconstructions are performed with either the RA filter alone or the RA and SA filters together, assuming a truncation frequency ( $\xi$ ) of  $2a^{-1}$  (14.3 lp/mm). Although  $\xi$  is typically chosen  
425 to be the detector alias frequency  $0.5a^{-1}$ , it is necessary to choose a higher value to achieve super-resolution. The specified value of  $\xi$  corresponds to the second zero of the MTF of the sampling process for frequency measurements along the  $f_1$  direction ( $f_2 = 0$ ).<sup>15-17</sup>

$$\text{MTF}(f_1, f_2) = \text{sinc}(a_x f_1) \text{sinc}(a_y f_2) \quad (87)$$

Figure 3 shows a plot of the reconstruction filters versus frequency. The two filters almost perfectly  
430 match each other at low frequencies but diverge at high frequencies, since the SA filter is intended  
to suppress high frequency noise.

### ***III. A. 1. Individual Projections***

At a fixed distance ( $u_2$ ) of 30.0 mm from the chest wall, Figure 4(a)-(b) shows a cross  
435 section of signal versus detector position  $u_1$  for the central projection ( $n = 0$ ) and an oblique  
projection ( $n = 7$ ). The  $u_2$  displacement lies between the chest wall and nipple of a typical breast.  
In the recent development of a physical 3D anthropomorphic phantom for image quality assessment  
in DM and DBT,<sup>18, 19</sup> Carton *et al.* modeled a distance of 65.0 mm between the chest wall and  
nipple for an average breast size of 450 mL. The  $u_2$  displacement considered in Figure 4(a)-(b) thus  
440 corresponds to a position approximately halfway between the chest wall and nipple of this phantom.

In Figure 4(c)-(d), the modulus of the Fourier transform of detector signal is plotted versus  
frequency  $f_1$ , assuming  $f_2 = 0$  [Eq. (64)]. The central and oblique projections are similar in that they  
both represent a high frequency input as if it were a lower frequency. The Fourier transform of  
either projection does not occur at the input frequency 5.00 lp/mm but instead occurs at a lower  
445 frequency as evidence of aliasing.

The two projections and their frequency spectra are also plotted in Figure 4 for an infinite  
source-to-COR distance ( $h$ ) with no other changes in the acquisition parameters. This limiting case  
transforms the divergent beam geometry into a parallel beam geometry. Consequently, the x-ray  
angle relative to the normal to the detector does not vary with position ( $u_1, u_2$ ) by Eq. (15) but  
450 instead is always  $\psi_n - \gamma_n$  for the  $n^{\text{th}}$  projection.

In the parallel beam geometry, the central projection represents the input frequency as if it  
were  $a^{-1} - f_0$ , or  $0.3a^{-1}$ . As a result, the Fourier transform has a major peak at  $0.3a^{-1}$  (2.14 lp/mm),

and has minor peaks at  $0.7a^{-1}$  (5.0 lp/mm),  $1.3a^{-1}$  (9.29 lp/mm), and  $1.7a^{-1}$  (12.14 lp/mm). Unlike the parallel beam geometry, the divergent beam geometry magnifies the input so that it projects  
 455 onto the x-ray converter with the frequency  $f_0/M$

$$M = \frac{h}{h - z_0}, \quad (88)$$

where  $M$  denotes the magnification.<sup>20</sup> With a source-to-COR distance ( $h$ ) of 70.0 cm and an object-to-detector distance ( $z_0$ ) of 50.0 mm,  $M$  is 1.077. As a result of the magnification, the peaks in the Fourier transform of detector signal occur at different frequencies than the parallel beam geometry.  
 460 Accordingly, these Fourier peaks occur at  $a^{-1} - f_0/M$  (2.50 lp/mm),  $f_0/M$  (4.64 lp/mm),  $2a^{-1} - f_0/M$  (9.64 lp/mm), and  $a^{-1} + f_0/M$  (11.78 lp/mm). The Fourier transform of the most oblique projection peaks at similar frequencies as the central projection.

### ***III. A. 2. SBP Reconstruction***

465 Figure 5(a) shows SBP reconstruction versus position ( $x$ ) measured parallel to the chest wall side of the breast support, performed at the distance  $y = 30.0$  mm from the chest wall and at the height  $z = z_0 = 50.0$  mm above the breast support. Unlike an individual projection, SBP reconstruction can resolve the input frequency 5.00 lp/mm. This property arises because the oblique projections give information about the input which is not present in the central projection  
 470 alone [Figure 4(b)]. Although not explicitly plotted in Figure 5(a), it can be shown that super-resolution is present across a broad range of  $x$  and  $y$  positions in the reconstructed volume.

The SBP Fourier transform [Eq. (86)] correctly possesses its major peak at 5.00 lp/mm. The major peak of an individual projection, occurring at 2.50 lp/mm, is now highly suppressed in magnitude [Figure 5(c)].

### ***III. A. 3. FBP Reconstruction***

FBP reconstructions are now performed with either the RA filter alone or the RA and SA filters together. In the spatial domain, these reconstructions are plotted versus position ( $x$ ) parallel to the chest wall side of the breast support, assuming  $y = 30.0$  mm and  $z = 50.0$  mm [Figure 5(b)].

480 Figure 5(b) demonstrates that reconstruction filters smoothen pixilation artifacts found in the SBP reconstruction. In addition, Figure 5(b) shows that reconstructing with the RA filter alone yields greater modulation than reconstructing with the RA and SA filters together. The modulation for reconstruction with the RA filter alone is 41.0%, yet the modulation for reconstruction with the RA and SA filters together is 29.8%. It is expected that reconstruction with the RA filter alone has  
485 greater modulation, since the amplitude of this filter exceeds that of the RA and SA filters together at the input frequency (Figure 3). Importantly, the modulation of either FBP reconstruction technique is well above the limit of resolution for typical imaging systems, which is often taken to be 5%. In addition, the modulation of either FBP reconstruction technique is greater than that of SBP reconstruction (18.4%).

490 Although reconstruction with the RA filter alone has the benefit of greater modulation than reconstruction with the RA and SA filters together, the trade-off is greater spectral leakage at very high frequencies. In fact, the amplitude of the high frequency spectral leakage is greater with the RA filter alone than with SBP. In experimental practice, reconstruction with the RA filter alone also increases the presence of noise, which tends to occur at high frequencies.

### **III. B. Input Frequency Directed Perpendicular to the Chest Wall**

495 It is now demonstrated that the existence of super-resolution is dependent on the directionality of the input frequency. Super-resolution arises because of sub-pixel detector element shifts in the image of an object with each increasing projection angle. In order to investigate the

feasibility of super-resolution for frequencies oriented along the  $y$  direction (*i.e.*, perpendicular to the chest wall), the translational shift in the  $u_2$  position of the incident x ray is now calculated. For the  $n^{\text{th}}$  projection, an x ray passing from the focal spot through the point  $(x, y, z)$  strikes the detector at the  $u_2$  coordinate

$$u_2(n) = \frac{y[l \cos \gamma_n + h \cos(\psi_n - \gamma_n)]}{x \sin \gamma_n + (l - z) \cos \gamma_n + h \cos(\psi_n - \gamma_n)}. \quad (89)$$

This expression follows from Eq. (16). The translational shift in the  $u_2$  position of the object comparing projection numbers  $n_1$  and  $n_2$  is thus

$$\Delta u_2(n_1, n_2) = u_2(n_2) - u_2(n_1). \quad (90)$$

Assuming that  $z = 50.0$  mm, Figure 6 shows the magnitude of this translational shift versus position  $y$  within two planes,  $x = 0$  and  $x = -30.0$  mm, comparing the central projection and an oblique projection ( $n_1 = 0, n_2 = 7$ ) as well as two oblique projections ( $n_1 = -7, n_2 = 7$ ). Throughout the remainder of this work, a plane defined by a fixed value of  $x$  will be termed an AP/SS plane since it has extent in both the anteroposterior (AP) and source-to-support (SS) directions. Although the SS direction technically varies with position on the breast support due to the divergence of the x-ray beam, it is assumed to be equivalent to the  $z$  direction for the purpose of this work. As such, the SS direction lies along the same axis as the source-to-image distance (SID), or the length between the focal spot and the origin O for the central projection (Figure 1). In a cranial-caudal (CC) view, an AP/SS plane is thus a sagittal plane through the breast. By contrast, in a mediolateral oblique (MLO) view, the same plane is at an approximately  $45^\circ$  angle relative to the sagittal and transverse planes through the breast.

In the mid AP/SS plane ( $x = 0$ ), translational shifts between projections are minimal in a typical sized breast. For example, with  $x = 0$ ,  $y = 30.0$  mm, and  $z = 50.0$  mm, the translational shift between the central projection and an oblique projection is 0.009 mm (6.52% of detector element

length), and the translational shift between the two most oblique projections is zero. For this reason, super-resolution along the  $y$  direction is simply not achievable within the mid AP/SS plane.

525 As illustrated in Figure 7(a), SBP reconstruction at  $x = 0$  in the region  $y \in [29.4 \text{ mm}, 30.6 \text{ mm}]$  resembles a single projection.

In Figure 6, it is demonstrated that the  $u_2$  translational shift between projections increases as the magnitude of the distance  $x$  increases. For example, with  $x = -30.0 \text{ mm}$  and  $y = 30.0 \text{ mm}$ , the translational shift between the central projection and the oblique projection is  $0.047 \text{ mm}$  (33.4% of detector element length), and the translational shift between the two most oblique projections is  $0.112 \text{ mm}$  (80.0% of detector element length). Because these translational shifts are sufficiently large, SBP reconstruction [Figure 7(c)] shows super-resolution at  $x = -30.0 \text{ mm}$  over the region  $y \in [29.4 \text{ mm}, 30.6 \text{ mm}]$ . Unlike SBP reconstruction for an input frequency oriented along the  $x$  direction [Figure 5(a)], the amplitudes of the peaks in Figure 7(c) are noticeably different from each other, indicating the presence of reconstruction artifacts. It can be shown that these artifacts are minimized by increasing the distance  $y$  from the chest wall, since the  $u_2$  translational shifts between projections increase with  $y$  (Figure 6).

The SBP reconstructions in Figure 7 can be analyzed further by computing their 1D Fourier transform along the  $y$  direction. To show differences in these Fourier transforms at fixed values of  $x$ , we choose not to transform over both  $x$  and  $y$  as given by Eq. (85).

$$\mathcal{F}_1[\mathcal{B}(\mathcal{X}\mu)](x, f_y, z) = \sum_{\mathbf{m}, n} \frac{\mathcal{D}\mu(\mathbf{m}, n)}{N} \frac{e^{\frac{2\pi i f_y (\sigma_{3\mathbf{m}l}x + \sigma_{5\mathbf{m}l}z)}{\sigma_{4\mathbf{m}l}}}}{\sigma_{4\mathbf{m}l}} \text{rect}\left[\frac{(\sigma_{1\mathbf{m}l}x + \sigma_{2\mathbf{m}l}z)\sec\theta_{\mathbf{m}l} - m_x a_x}{a_x}\right] \mathcal{F}_1\rho_2\left(\frac{f_y}{\sigma_{4\mathbf{m}l}}\right) \quad (91)$$

For additional proof that super-resolution is not achievable within the mid AP/SS plane, Figure 7(b) shows that the major Fourier peak at  $x = 0$  occurs well below the input frequency. By contrast, the major Fourier peak at  $x = -30.0 \text{ mm}$  [Figure 7(d)] matches the input frequency,  $5.00 \text{ lp/mm}$ .



Although not shown in the plot, it can be demonstrated that spectral leakage is reduced by increasing the magnitude of the distance  $x$  relative to the mid AP/SS plane.

As a final point in this section, it is important to note that by applying the filters in Figure 3 to the SBP reconstructions of Figure 7, the modulation effectively vanishes (graph not shown). This finding arises because filtering is applied only within the plane of the chest wall [Eq. (40)]. An input frequency oriented along the  $y$  direction contributes a component of 0 lp/mm within the plane of the chest wall; since the reconstruction filters vanish at 0 lp/mm (Figure 3), FBP reconstructions are expected to have no modulation. For this reason, future research on filter optimization is merited as described in the Discussion section.

#### **IV. EXPERIMENTAL AND CLINICAL VALIDATION**

Using a high contrast bar pattern phantom, we have experimentally verified the existence of super-resolution in DBT. The phantom was taped beneath the compression paddle (24 cm  $\times$  29 cm) of the Selenia Dimensions system, and placed 2.5 cm above the breast support. With the alternating light and dark bands of the phantom spanning a 6.0 mm length, the line pairs ranged in frequency from 1.0 lp/mm to 10.0 lp/mm. To match the simulation of Section IIIA, the frequency 5.0 lp/mm was oriented along the  $x$  direction parallel to the chest wall side of the breast support. Also, following the simulation, the bar patterns at 5.0 lp/mm covered the region  $x \in [-0.6 \text{ mm}, 0.6 \text{ mm}]$ , and the edge of the bar patterns near the numeral “5” (Figure 8) was positioned slightly greater than  $y = 30 \text{ mm}$  from the chest wall. Using the large (0.3 mm nominal) focal spot and a CC view, 15 projections were acquired at 30 kVp and 14 mAs with a W/AI target-filter combination. The technique for determining the optimal mAs with photo-timing is described in our previous work.<sup>4</sup>

Reconstruction was subsequently performed using a backprojection filtering (BPF) commercial prototype reconstruction solution (Briona<sup>TM</sup>, Real Time Tomography, Villanova, PA).

570 Although it is possible to reconstruct on a non-pixelated grid using analytical modeling, a pixelated grid was required for the experimental data. In order to ensure that high frequencies can be resolved in the plane of the reconstruction, the pixel size of the reconstruction grid (20.44  $\mu\text{m}$ ) was chosen to be significantly smaller than that of the detector elements (140  $\mu\text{m}$ ). Consequently, the alias frequency of the reconstruction grid (24.46 lp/mm) was substantially higher than the alias  
575 frequency of the detector (3.57 lp/mm).

Figure 8 shows that the central projection correctly resolves frequencies below the detector alias frequency, 3.57 lp/mm. At the next highest frequency (4.0 lp/mm), one would expect to see 24 line pairs spanning a 6.0 mm length. Instead, less than 24 line pairs are visible, and Moiré patterns<sup>21</sup> are present. Finally, at 5.0 lp/mm, only 16 line pairs are evident within a 6.0 mm length,  
580 indicating that the pattern is incorrectly represented as a frequency between 2.0 and 3.0 lp/mm.

Unlike the central projection, BPF reconstruction can resolve frequencies higher than the detector alias frequency (Figure 9). In fact, up to 6.0 lp/mm (36 line pairs spanning 6.0 mm) can be observed at the correct orientation with no Moiré patterns. At 7.0 lp/mm, the signal becomes too faint to distinguish bar patterns. This finding arises because the MTF of the reconstruction is  
585 reduced with increasing frequency; recall from Eq. (87) that the MTF of the sampling process vanishes at the frequency  $f_1 = a^{-1}$  (7.14 lp/mm), assuming  $f_2 = 0$ . As expected from the analytical modeling, it should be noted that super-resolution along the  $x$  direction was observed over many different x-ray acquisitions in which the bar pattern phantom was placed at various positions in the imaging volume.

590 By rotating the bar pattern phantom 90°, the potential for super-resolution orthogonal to the chest wall was also analyzed (Figure 10). To orient the reader with the positioning of the phantom, it is important to note that the left edges of the even numerals “4” and “6” were aligned on the mid AP/SS plane ( $x = 0$ ), and that the separation between 4.0 and 5.0 lp/mm was positioned at a

displacement  $y = 30$  mm from the chest wall. As expected from the analytical modeling (Section IIIB), the extreme left regions of the bar patterns show aliasing of high frequencies due to their proximity to the mid AP/SS plane. Super-resolution is only present at the extreme right of the bar patterns (5.0 and 6.0 lp/mm), where the magnitude of the distance  $x$  relative to the mid AP/SS plane is approximately 30 mm or greater.

It is important to note that the extreme right of the bar patterns at 4.0 lp/mm does not display super-resolution as cleanly as the extreme right of the bar patterns at 5.0 and 6.0 lp/mm due to the presence of Moiré patterns. Recall that the phantom is positioned so that lower frequencies are closer to the chest wall. Because the  $u_2$  translational shift between projections is minimized with decreasing distance from the chest wall (Figure 6), it is expected that super-resolution along the  $y$  direction should not be achievable at positions too close to the chest wall.

In breast imaging, super-resolution has applications in improving the visualization of small microcalcification clusters, which are an early indication of cancer. This concept is illustrated in Figure 11. In the figure, the left image is generated by bilinearly interpolating a BPF reconstruction performed using pixels of length 140  $\mu\text{m}$ . The bilinear interpolation yields a final result (a) with pixels of length 35  $\mu\text{m}$  (hence, four-fold magnification). By contrast, the right image (b) is generated by performing a BPF reconstruction using pixels of length 35  $\mu\text{m}$ . Super-resolution is present in (b), not (a). A few small microcalcifications that cannot be discerned in image (a) are indeed evident in image (b), and finer detail in their overall structural morphology can be observed in image (b). Having a clearer image of the structural features of microcalcifications is useful as it yields greater diagnostic information about their pathology,<sup>22</sup> and can help to diagnose breast cancer in its early stages of development. For this reason, super-resolution in DBT has enormous potential for future applications in breast imaging.

## **V. DISCUSSION**

In DBT reconstructions using grids with the same pixel size as the detector elements, the highest frequency that can be resolved in each reconstructed slice is the detector alias frequency. This study demonstrates that reconstruction grids with much smaller pixilation display super-resolution, or visibility of higher frequencies. Super-resolution arises because the image of the object is shifted in sub-pixel detector element increments with each increasing projection angle.

Super-resolution was first demonstrated analytically by calculating the reconstruction of a sinusoidal input whose frequency was oriented along the  $x$  direction parallel to the chest wall side of the breast support. Using an infinitesimally fine reconstruction grid, it was shown that both SBP and FBP can resolve higher frequencies than a single projection over a broad range of positions in the imaging volume. FBP reconstructions were performed either with the RA filter alone or with the RA and SA filters together. Although reconstruction with the RA filter alone has the benefit of greater modulation in the spatial domain, it presents the trade-off of increased noise and spectral leakage at high frequencies. In rotating the sine plate by  $90^\circ$ , the visibility of high frequencies was found to be dependent upon position within the reconstructed volume. Positions with super-resolution along the  $y$  direction must be sufficiently displaced relative to the chest wall ( $y = 0$ ) and to the mid AP/SS plane ( $x = 0$ ).

We have experimentally observed super-resolution in images of bar patterns using the Selenia Dimensions system and a commercial BPF reconstruction algorithm. A single projection showed classical signs of aliasing, including Moiré patterns and the visibility of fewer line pairs than expected. By contrast, reconstructions using very fine grids resolved frequencies higher than the alias frequency of the detector. For the two orientations of the bar patterns, the presence of super-resolution was verified at positions predicted from analytical modeling. In select clinical examples, super-resolution was found to improve the visibility of microcalcifications, which are

early indicators of breast cancer in many women. As a result of super-resolution, the morphology of microcalcifications was seen more clearly, and small microcalcifications that were not otherwise visible became apparent.

645 Super-resolution is a particularly useful property for x-ray systems that employ binning when switching from 2D to 3D imaging modes. For example, in the Selenia Dimensions system, the DM detector element dimensions are  $70\text{ }\mu\text{m} \times 70\text{ }\mu\text{m}$ , whereas the DBT detector element dimensions are  $140\text{ }\mu\text{m} \times 140\text{ }\mu\text{m}$ . Binning has the benefit of lowering the readout time, but presents the drawback of reducing the alias frequency of the detector. Initially, it would seem that  
650 binning should make DBT less capable of resolving high frequency information, such as microcalcifications. However, the existence of super-resolution in the reconstruction may counter the trade-offs of binning.

Some of the limitations of this study and directions for future investigation are now noted. In calculating detector signal, this paper assumes that the MTF of *a*-Se in drift mode is unity. While  
655 this assumption is valid for normal x-ray incidence, it is less justifiable with oblique x-ray incidence.<sup>23-27</sup> Que and Rowlands proposed the first analytical model of the optical transfer function (OTF) of *a*-Se in drift mode for all incident angles.<sup>23</sup> Their work was later validated by Hajdok and Cunningham with Monte Carlo simulations.<sup>24</sup> Denoting  $\mu_{\text{Se}}$  as the attenuation coefficient of Se and  $L$  as the thickness of the photoconductor, the OTF at each frequency  $f$  is

660 
$$\text{OTF}(f) = \frac{\left[1 - e^{-(\mu_{\text{Se}}L \sec \theta_n + 2\pi i f L \tan \theta_n)}\right] \cos \theta_n}{1 + \frac{2\pi i f \sin \theta_n}{\mu_{\text{Se}}}}. \quad (92)$$

The MTF is the normalized modulus of the OTF. For more thorough modeling, signal in the x-ray converter should be convolved with the point spread function (PSF) of *a*-Se before detector element sampling is performed, where the PSF is determined from the OTF using Fourier theory. It is important to model MTF degradation for measurements near the edge of the detector opposite the

665 chest wall, as the incident angle deviates considerably from the normal. Upon examining  $\theta_n$  across multiple projections in the Selenia Dimensions detector, it can be shown that the maximum incident angle is approximately  $25^\circ$ . Assuming 200  $\mu\text{m}$  thick  $\alpha\text{-Se}$  and 20 keV x rays<sup>28-30</sup> for which  $\mu_{\text{Se}}$  is  $20.5 \text{ mm}^{-1}$ ,<sup>31</sup> the corresponding MTF at 5.0 lp/mm is 85.8%.

While it is important to consider MTF degradation at positions distal to the chest wall, it is  
670 less critical for positions close to the chest wall. For example, in the central projection at the position  $u_1 = u_2 = 30.0 \text{ mm}$ , the incident angle is  $3.47^\circ$ , and the MTF at 5.0 lp/mm is 99.7%. Consequently, for the purpose of this work, an x-ray converter with MTF of unity was assumed.

In addition to modeling the MTF of the x-ray converter, the analytical model of super-resolution can be refined by modeling the MTF of the focal spot. Although this paper assumes a  
675 point-like focal spot, future work should consider the MTF degradation with increasing focal spot size<sup>32</sup> and increasing focal spot motion during a continuous scan of the projections.<sup>13, 33</sup> Detector lag and ghosting<sup>34-36</sup> should also be simulated, and the presence of shot noise<sup>37</sup> should be modeled at various dose levels. Because this work considers a high contrast input frequency either with the analytical simulation or with the experimental bar patterns, it was not necessary to model the  
680 presence of noise at different dose levels. Future studies on super-resolution with low contrast input frequencies will require a noise simulation, as the visibility of the patterns should be influenced by dose. Finally, because the linear attenuation coefficient of an input is energy dependent, polyenergetic x-ray spectra<sup>38-40</sup> should also be simulated in the analytical model. This work implicitly assumes a monoenergetic x-ray beam.

685 In CT, the conventional low frequency filter is the RA filter<sup>13, 14</sup> which increases linearly with frequency from zero (Figure 3). Since filtering was only applied in the plane of the x-ray tube motion, this work has demonstrated that the RA filter is not suited for imaging frequencies perpendicular to the chest wall, since the modulation of the reconstruction vanishes (Section IIIB).

Lauritsch and Härer have shown that replacing the conventional filter with a polynomial filter improves the quality of the DBT reconstruction. Their filter rises sharply at low frequencies, plateaus to unity at intermediate frequencies, and falls in value at high frequencies.<sup>41, 42</sup> Future work should consider a polynomial filter for analytical modeling of super-resolution, since the non-zero offset will never yield zero modulation for any orientation of the input frequency. It should be noted that the filters used in the experimental reconstructions of bar patterns oriented perpendicular to the chest wall (Figure 10) have a non-zero offset at 0 lp/mm, unlike the RA filter used in the analytical modeling.

Because super-resolution has important clinical applications in improving the visibility of microcalcifications, future work should ultimately transition from modeling a sinusoidal input to simulating microcalcifications in a breast background.<sup>43</sup> Using model observers, improvements in the visibility of microcalcifications should be assessed with image reconstructions at varying grid sizes. It would be useful to determine that coarsest grid size at which the benefits of super-resolution are achieved among observers, as reconstructions on coarser grids require less memory for data storage.

## **VI. CONCLUSION**

To our knowledge, this work is the first to demonstrate the existence of super-resolution in DBT. An analytical model of super-resolution was developed by calculating the reconstruction of a high frequency sinusoidal input. While a single projection cannot resolve frequencies higher than the alias frequency of the detector, a reconstruction on a very fine grid can resolve these frequencies. Super-resolution is made possible by the sub-pixel detector element shifts in the image of the object between projections.



Using a bar pattern phantom, we have experimentally verified the existence of super-resolution in DBT. In considering an input frequency oriented both parallel and perpendicular to the chest wall side of the breast support, the experimental images confirmed the presence of super-resolution at positions predicted by analytical modeling. Ultimately, super-resolution was shown to improve the visibility of fine structural details of microcalcifications in clinical DBT images.

## **ACKNOWLEDGEMENT**

The authors thank Baorui Ren (Hologic Inc., Bedford, MA) for providing useful background information on the acquisition geometry of the Selenia Dimensions tomosynthesis system. In addition, we gratefully acknowledge the assistance of Michael O'Shea and Roshan Karunamuni (University of Pennsylvania, Philadelphia, PA) in the acquisition of the bar pattern images showing the experimental feasibility of super-resolution in DBT. Also, we thank Johnny Kuo, Susan Ng, Peter Ringer (Real Time Tomography, LLC, Villanova, PA), and Predrag Bakic (University of Pennsylvania) for their help in reconstructing bar pattern and clinical images. Finally, we are grateful to David Pokrajac (Delaware State University, Dover, DE) for helpful feedback on improving the efficiency of MATLAB coding. Andrew D. A. Maidment is the chair of the Scientific Advisory Board of Real Time Tomography.

The project described was supported by Grant T32EB009384-01 from the National Institute of Biomedical Imaging and Bioengineering (NIBIB). The content is solely the responsibility of the authors and does not necessarily represent the official views of the NIBIB or the National Institutes of Health (NIH). Additional support for RJA was provided by predoctoral training grant No. W81XWH-11-1-0100 through the Department of Defense Breast Cancer Research Program. Support for RTT was provided separately through NIH grants R43EB007140/R44EB007140.

## **APPENDIX A: DETECTOR SIGNAL FOR AN INPUT FREQUENCY DIRECTED PERPENDICULAR TO THE CHEST WALL**

This appendix calculates detector signal for an input frequency perpendicular to the chest wall. Under this assumption, the input rectangular prism of thickness  $\varepsilon$  has a linear attenuation coefficient  $\mu(x, y, z)$  which varies sinusoidally along the  $y$  direction with frequency  $f_0$

$$\mu(x, y, z) = C \cdot \cos[2\pi f_0(y - y_0)] \cdot \text{rect}\left(\frac{z - z_0}{\varepsilon}\right), \quad [(A1): cf. (1)]$$

where  $y_0$  is a translational shift in the waveform relative to the origin. The amplitude  $C$  of the waveform is equivalent to  $1/\varepsilon$  upon normalizing total attenuation along the  $z$  direction. The 1D Fourier transform of Eq. (A1) along the  $y$  direction peaks at the frequencies  $f_y = \pm f_0$  and vanishes at all other frequencies, following a formula similar to Eq. (4) with the exchange of  $x_0$  for  $y_0$  and  $f_x$  for  $f_y$ . Using Eqs. (17)-(19) and Eq. (22), total x-ray attenuation versus position  $(u_1, u_2)$  along the plane of the rotated detector is calculated for the  $n^{\text{th}}$  projection as

$$\mathcal{A}\mu(n) = \kappa_n \int_{w_n^+}^{w_n^-} \cos(2\pi f_0 u_2 w + \Lambda) dw \quad [(A2): cf. (23)]$$

$$= \frac{\kappa_n \left( \sin[2\pi f_0 u_2 w_n^- + \Lambda] - \sin[2\pi f_0 u_2 w_n^+ + \Lambda] \right)}{2\pi f_0 u_2}, \quad [(A3): cf. (24)]$$

where

$$\Lambda = -2\pi f_0 y_0. \quad [(A4): cf. (26)]$$

Following the sum-to-product trigonometric identity given in Eq. (27), one may rewrite Eq. (A3) as

$$\mathcal{A}\mu(n) = \kappa_n (w_n^- - w_n^+) \cos[\pi f_0 u_2 (w_n^+ + w_n^-) + \Lambda] \text{sinc}\left[f_0 u_2 (w_n^- - w_n^+)\right] \quad [(A5): cf. (28)]$$

$$= \frac{\varepsilon \kappa_n \cos\left[\frac{2\pi f_0 u_2 (l + h \cos \psi_n - z_0)}{l + h \cos \psi_n - u_1 \sin \gamma_n} + \Lambda\right] \text{sinc}\left[\frac{\varepsilon f_0 u_2}{l + h \cos \psi_n - u_1 \sin \gamma_n}\right]}{l + h \cos \psi_n - u_1 \sin \gamma_n}. \quad [(A6): cf. (29)]$$

755 The logarithmically-transformed signal in the  $\mathbf{m}^{\text{th}}$  detector element for the  $n^{\text{th}}$  projection is now determined from Eq. (31). The midpoint formula<sup>44</sup> for approximating this double integral is

$$\mathcal{D}\mu(\mathbf{m}, n) = \lim_{J_y \rightarrow \infty} \frac{1}{J_y} \sum_{j_y=1}^{J_y} \left[ \lim_{J_x \rightarrow \infty} \frac{1}{J_x} \sum_{j_x=1}^{J_x} \mathcal{A}\mu(j_x, j_y, n) \right], \quad [(\text{A7}): \text{cf. (35)}]$$

where

$$\mathcal{A}\mu(j_x, j_y, n) \equiv \mathcal{A}\mu(n) \Big|_{(u_1, u_2) = \left( a_x \left[ \frac{j_x - 1/2}{J_x} + m_x - \frac{1}{2} \right], a_y \left[ \frac{j_y - 1/2}{J_y} + m_y \right] \right)}. \quad [(\text{A8}): \text{cf. (36)}]$$

760 FBP reconstruction now follows from Eq. (42).

## APPENDIX B: NOMENCLATURE

Symbol	Meaning
$\bullet$	Dot product operator.
$*$	Convolution operator.
$\times$	Cross product operator.
$\in$	Set membership.
$\mathcal{A}\mu(n)$	Total attenuation for the $n^{\text{th}}$ projection.
$\tilde{\mathcal{A}}\mu(n)$	A useful approximation for total attenuation [Eqs. (32)-(33)].
$\mathcal{B}$	Backprojection operator.
$\mathcal{D}\mu(\mathbf{m}, n)$	Signal in the $\mathbf{m}^{\text{th}}$ detector element for the $n^{\text{th}}$ projection.
$\mathcal{F}$	Fourier transform operator (subscript denotes dimension).
$\mathcal{L}_n$	Path length through the input for the $n^{\text{th}}$ projection.
$\mathbb{R}^3$	Euclidean 3-space.
$S\mu(u_1, u_2)$	Raw signal at coordinate $(u_1, u_2)$ on the rotated detector.

$\mathcal{X}$	X-ray transform operator.
$\mathbb{Z}$	Set of integers.
$\mathbb{Z}^*$	Set of non-negative integers.
$\gamma_n$	Angle of rotation of the detector relative to the $x$ axis for the $n^{\text{th}}$ projection.
$\Gamma_{\mathbf{m}n}$	Angle of backprojection within the plane of the detector [Eqs. (53)-(54)].
$\delta$	Delta function.
$\Delta\psi$	Angular spacing between projections.
$\Delta u_2(n_1, n_2)$	Translational shift in $u_2$ coordinate of incident ray comparing projection numbers $n_1$ and $n_2$ .
$\varepsilon$	Thickness of sine plate (Figure 1).
$\theta_n$	Angle of x-ray incidence relative to the normal to the detector ( $\theta_{\mathbf{m}n}$ denotes the special case at the centroid of the $\mathbf{m}^{\text{th}}$ detector element for the $n^{\text{th}}$ projection).
$\kappa_n$	A quantity defined by Eq. (25).
$\lambda_n$	A quantity defined by Eq. (26).
$\Lambda$	A quantity defined by Eq. (A6).
$\mu$	X-ray linear attenuation coefficient of input.
$\mu_{\text{Se}}$	X-ray linear attenuation coefficient of $a$ -Se photoconductor.
$\xi$	Truncation frequency of reconstruction filter.
$\rho_1, \rho_2$	Quantities defined by Eqs. (66)-(67).
$\sigma_{j\mathbf{m}n}$	Terms defined by Eqs. (68)-(72) used to simplify intermediate calculations, where $j$ varies from 1 to 5.
$\phi$	Reconstruction filter.

$\psi_n$	Nominal projection angle.
AP	Anteroposterior (in breast x-ray imaging, the direction perpendicular to the chest wall).
AP/SS	Descriptive acronym for a plane with extent along the anteroposterior (AP) and source-to-support (SS) directions.
$a_x, a_y$	Detector element dimensions in the $x$ and $y$ directions; if the $x$ and $y$ subscripts are removed, the detector element is square ( $a_x = a_y = a$ ).
$b_1, b_2$	Real numbers used to illustrate a sum-to-product trigonometric identity [Eq. (27)].
$C$	Amplitude of sine input taken to be $1/\varepsilon$ .
CC	Cranial-caudal.
COR	Center-of-rotation of x-ray tube motion.
CT	Computed tomography.
$d_n$	Distance between points G and O (Figure 2).
DBT	Digital breast tomosynthesis.
DM	Digital mammography.
$f$	Spatial frequency ( $f_0$ denotes the input frequency).
FBP	Filtered backprojection.
$g$	Gear ratio of detector.
$h$	Source-to-COR distance for rotating x-ray tube.
$i$	Imaginary unit given as $\sqrt{-1}$ .
$I_{xm}$	An integral defined by Eq. (81).
$I_{ym}(x)$	An integral defined by Eq. (76).

$l$	Distance between the COR and the midpoint of the chest wall side of the detector.
lp	Line pairs.
$\mathbf{m}$	A doublet with coordinates $(m_x, m_y)$ used for labeling detector elements.
$M$	Magnification.
MLO	Mediolateral oblique.
MRI	Magnetic resonance imaging.
MTF	Modulation transfer function.
$n$	Projection number.
$N$	Total number of projections.
OTF	Optical transfer function.
RA	Ramp filter.
SA	Spectrum apodization filter.
SBP	Simple backprojection.
SID	Source-to-image distance (commonly measured between the focal spot and the midpoint of the chest wall side of the detector in the central projection).
SNR	Signal-to-noise ratio.
SS	Source-to-support (defined to be synonymous with the $z$ direction).
$t_1, t_2$	Affine parameters of the x-ray transform.
TFT	Thin-film transistor.
$u_1, u_2$	Position in the plane of the rotated detector (parallel and perpendicular to the chest wall, respectively).
$w$	Parameter ranging between 0 and 1 in the equation of the x-ray beam between the focal spot and the incident point on the detector [Eq. (16)].

$w_n^\pm$	Value of $w$ at the entrance ( $w_n^+$ ) and exit ( $w_n^-$ ) points of the x-ray beam through the sine plate (Figure 1) for the $n^{\text{th}}$ projection.
$x$	Position parallel to the chest wall side of the breast support; rotation by the angle $\gamma_n$ about the $y$ axis yields $x'_n$ .
$x_0$	Translational shift in the input waveform along the $x$ direction.
$y$	Position perpendicular to the chest wall; it is equivalent to $y'_n$ .
$y_0$	Translational shift in the input waveform along the $y$ direction.
$z$	Position perpendicular to the plane of the breast support; rotation by the angle $\gamma_n$ about the $y$ axis yields $z'_n$ .
$z_0$	Central height of the input relative to the midpoint of the chest wall side of the detector.

765

770



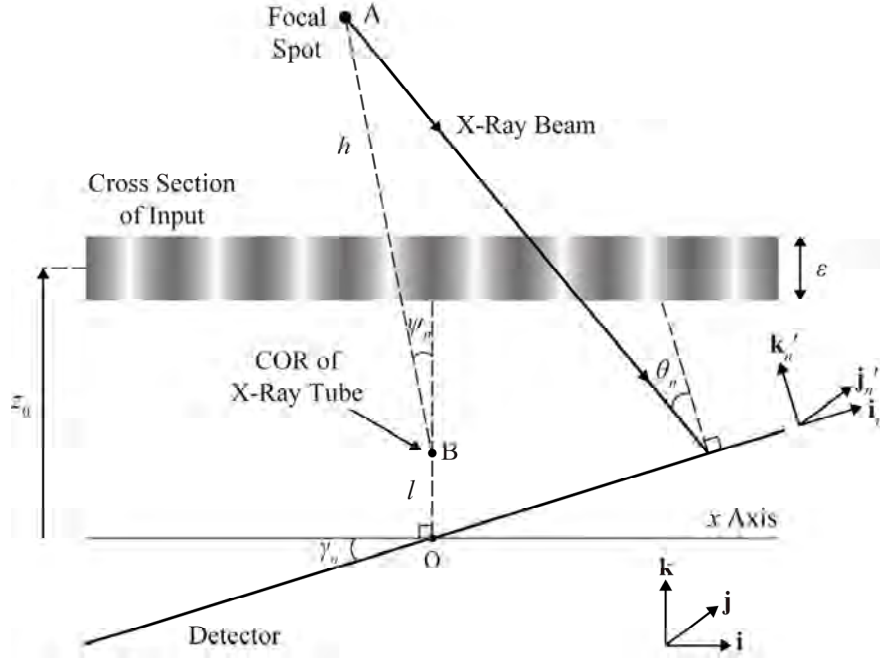


**Figure 1.** The 3D input object is a rectangular prism whose linear attenuation coefficient varies sinusoidally with position  $x$  parallel to the chest wall side of the breast support. A 2D cross section of the input object through the plane of the chest wall is shown (figure not to scale). In acquiring projection images, the x-ray tube rotates within the  $xz$  plane about point B, and the detector simultaneously rotates about the  $y$  axis. The primed unit vectors  $\mathbf{i}_n'$  and  $\mathbf{j}_n'$  define the coordinate axes of the plane of the detector for the  $n^{\text{th}}$  projection.

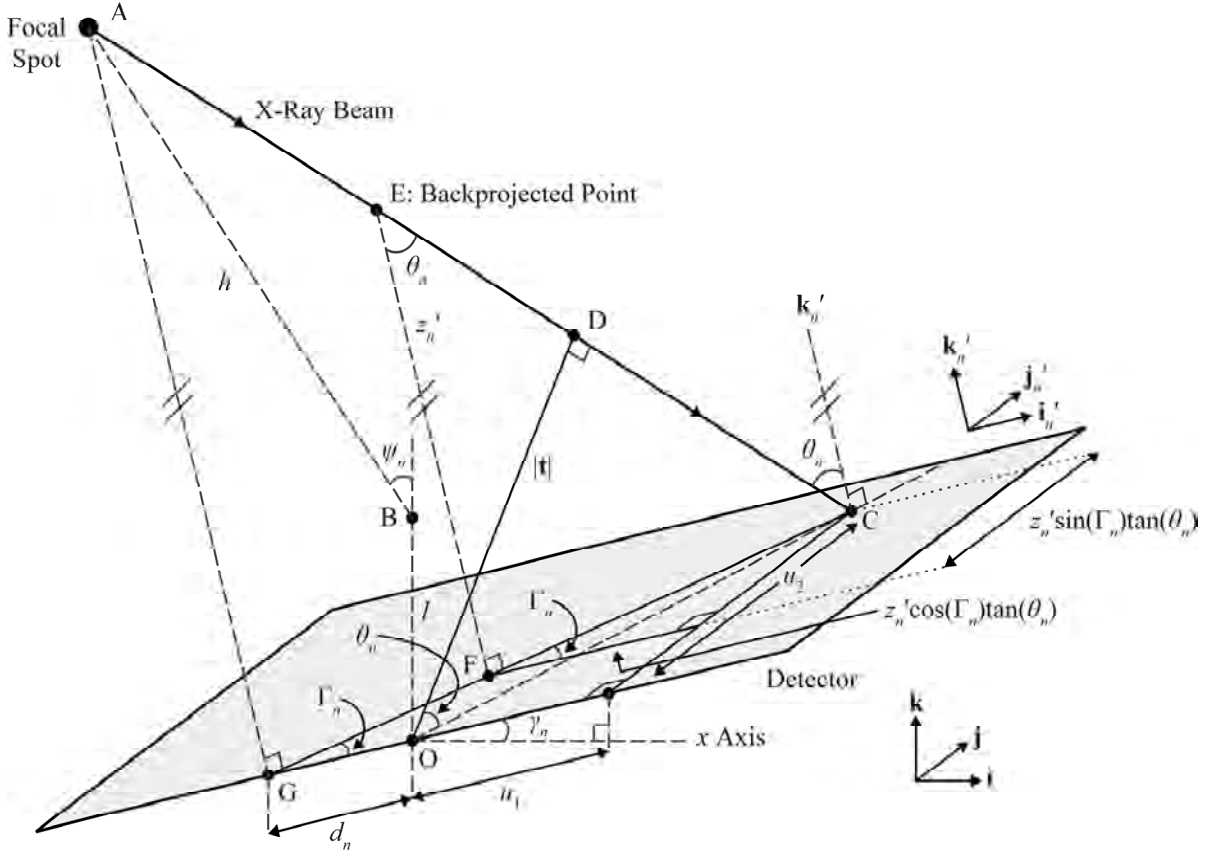


**Figure 2.** A schematic diagram of the DBT acquisition geometry is shown (figure not to scale).

The x-ray beam strikes point C at the angle  $\theta_n$  relative to the normal to the detector. In FBP reconstruction, signal at C is backprojected to an arbitrary point E along the incident ray. Within the plane of the detector, backprojection is directed toward point F along the angle  $\Gamma_n$  relative to the  $\mathbf{i}'_n$  axis.

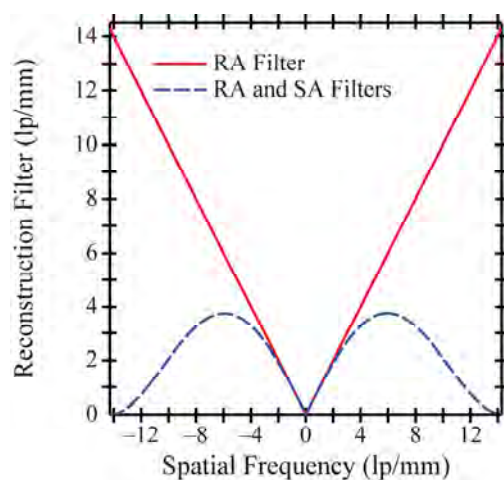


**Figure 3.** Reconstruction is performed with either the ramp (RA) filter alone or the RA and

805 spectrum apodization (SA) filters together. The SA filter is a Hanning window function.

810

815

820

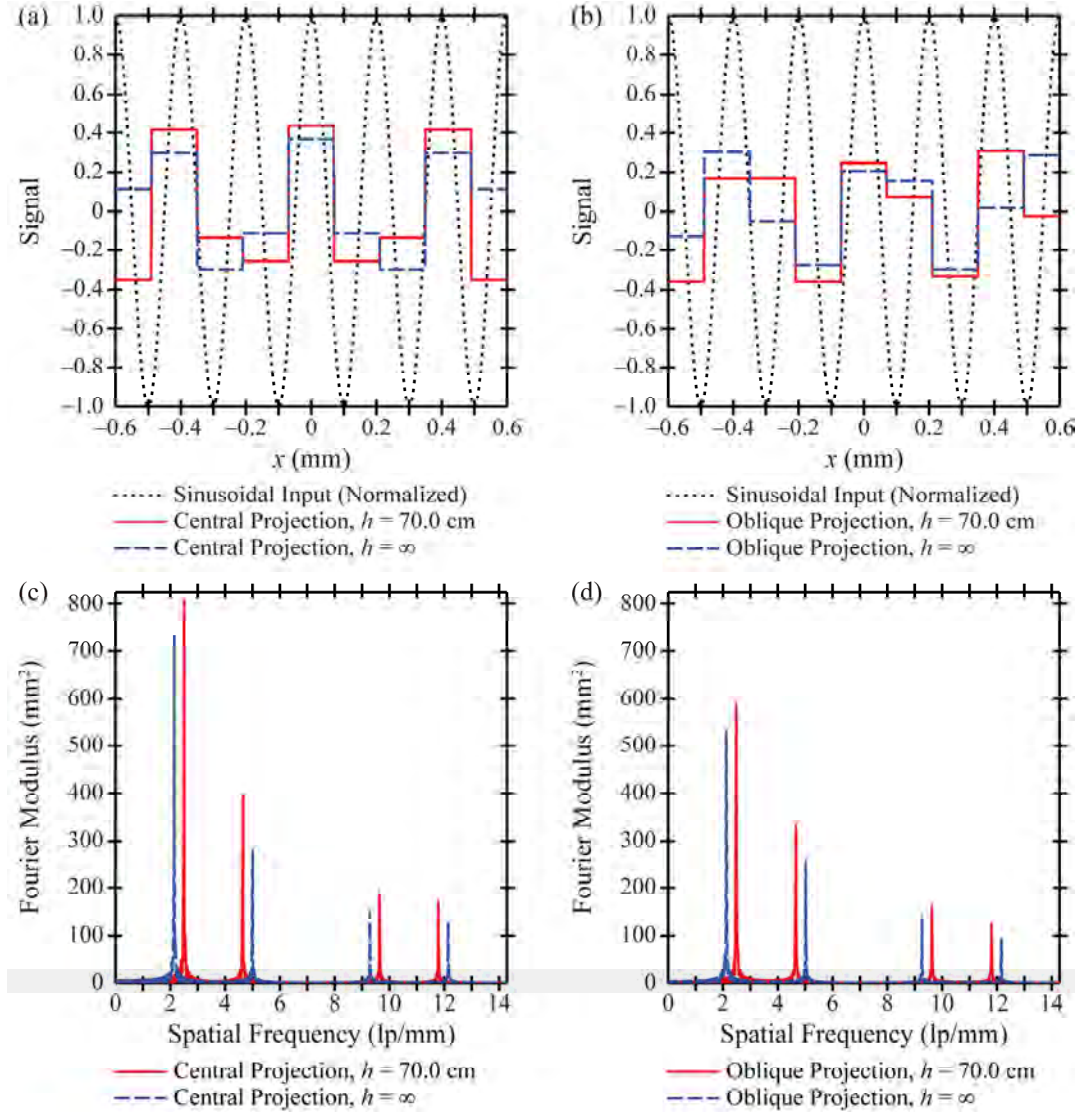


**Figure 4.** At a distance  $y$  of 30.0 mm from the chest wall, cross sections of signal in the central projection ( $n = 0$ ) and the most oblique projection ( $n = 7$ ) are plotted versus position  $x$ . In addition, Fourier transforms are shown versus frequency. The major Fourier peaks do not occur at the input frequency 5.00 lp/mm, illustrating the presence of aliasing. Reducing the source-to-COR distance ( $h$ ) magnifies the input frequency projected onto the detector.

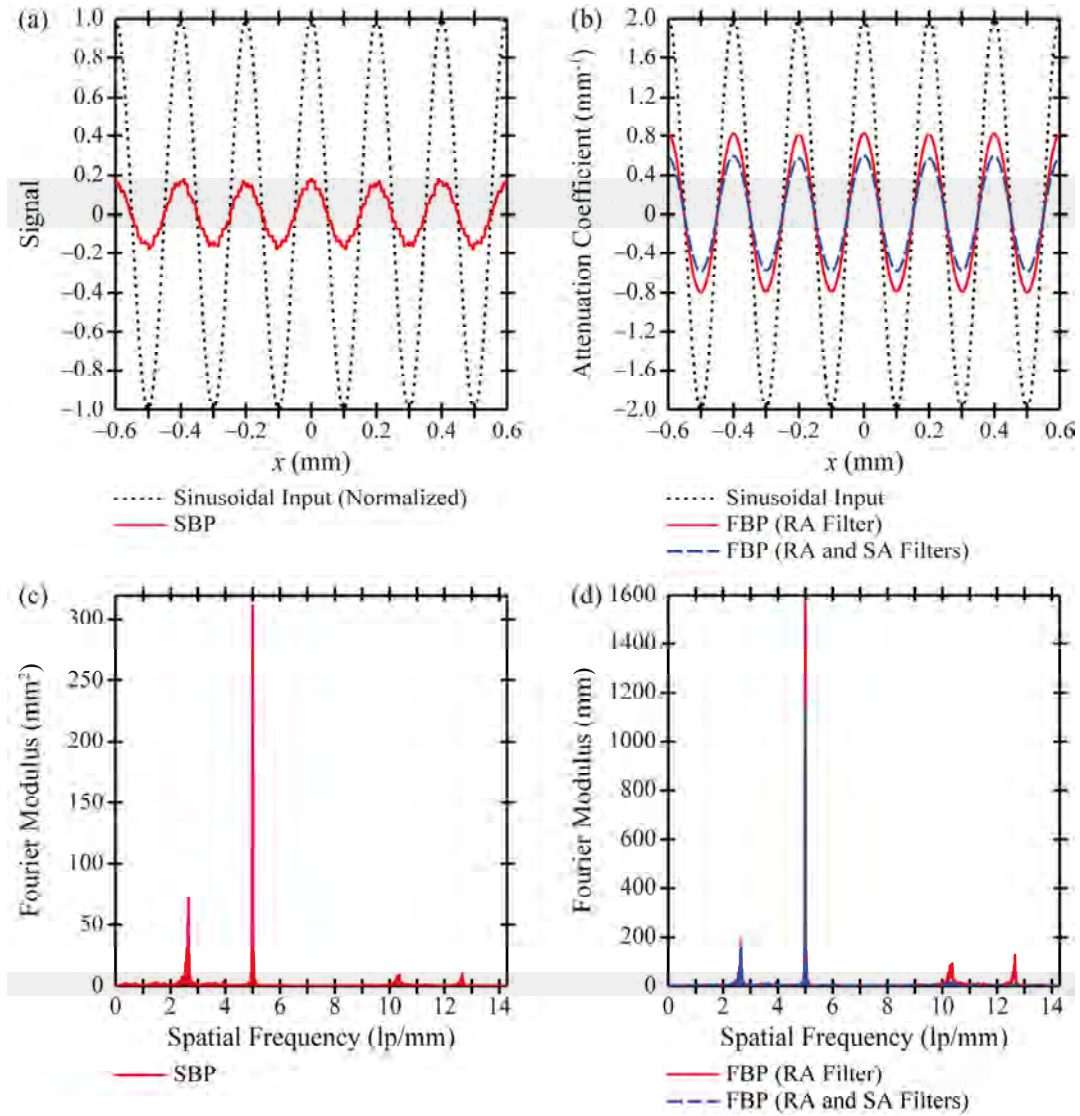
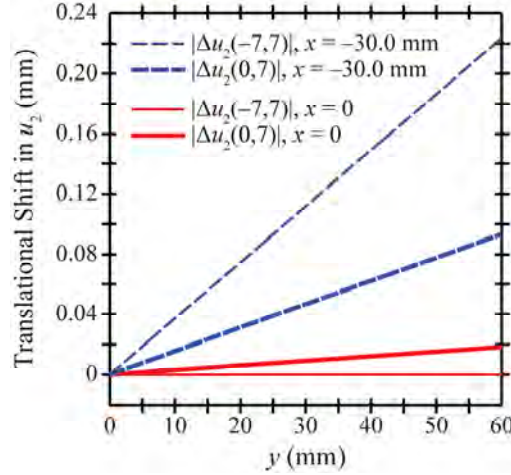


**Figure 5.** Unlike a single projection (Figure 4), simple backprojection (SBP) reconstruction can resolve a high frequency input oriented along the  $x$  direction. Applying filters to the reconstruction smoothens pixilation artifacts in the spatial domain and reduces low frequency spectral leakage in the Fourier domain. Reconstructing with the ramp (RA) filter alone has the benefit of greater modulation than reconstructing with the RA and spectrum apodization (SA) filters together. The drawback of reconstructing with the RA filter alone is increasing the amplitude of high frequency spectral leakage.



840 **Figure 6.** At a reconstruction depth ( $z$ ) of 50.0 mm, the magnitude of the translational shift in the  
 $u_2$  coordinate of the image [Eq. (90)] is plotted versus position  $y$  measured perpendicular to the  
chest wall. In the mid AP/SS plane ( $x = 0$ ), translational shifts are minimal comparing the central  
projection and an oblique projection ( $n_1 = 0, n_2 = 7$ ), and are zero comparing the two most oblique  
projections ( $n_1 = -7, n_2 = 7$ ). Increasing the magnitude of the distance  $x$  relative to the mid AP/SS  
845 plane yields a noticeable change in the translational shift.

850

855



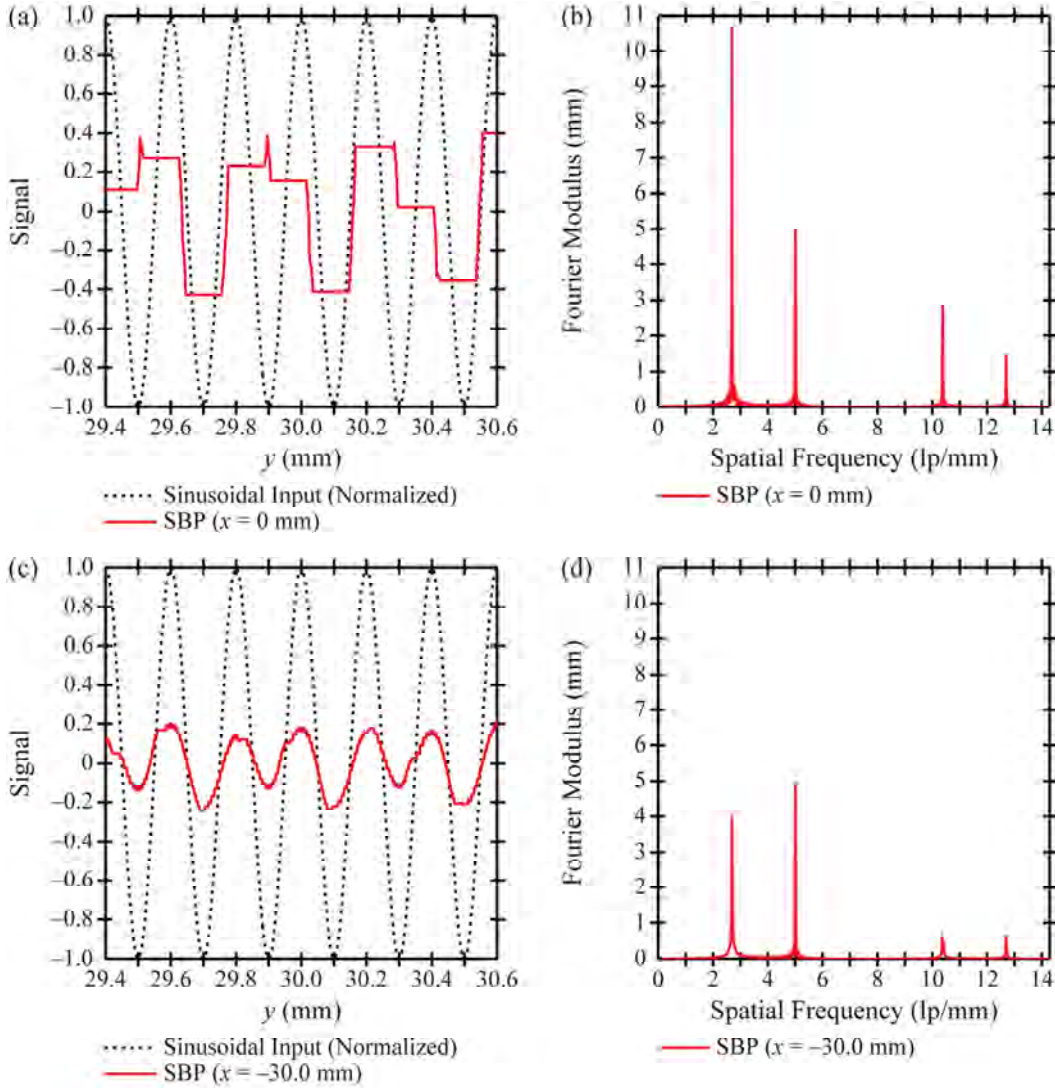


**Figure 7.** (a) Within the mid AP/SS plane ( $x = 0$ ), SBP reconstruction resembles a single projection over the region  $y \in [29.4 \text{ mm}, 30.6 \text{ mm}]$  for an input frequency oriented along the  $y$  direction

perpendicular to the chest wall. (b) The 1D Fourier transform of the SBP reconstruction is plotted versus frequency measured along the  $y$  direction. Within the mid AP/SS plane of a typical sized breast, the major Fourier peak occurs at a frequency lower than the input frequency, 5.00 lp/mm.

(c) With  $x = -30.0 \text{ mm}$ , super-resolution in an SBP reconstruction is indeed achievable over the region  $y \in [29.4 \text{ mm}, 30.6 \text{ mm}]$ . (d) For additional proof of super-resolution at  $x = -30.0 \text{ mm}$ , the

major peak of the corresponding Fourier transform occurs at the input frequency, 5.00 lp/mm.

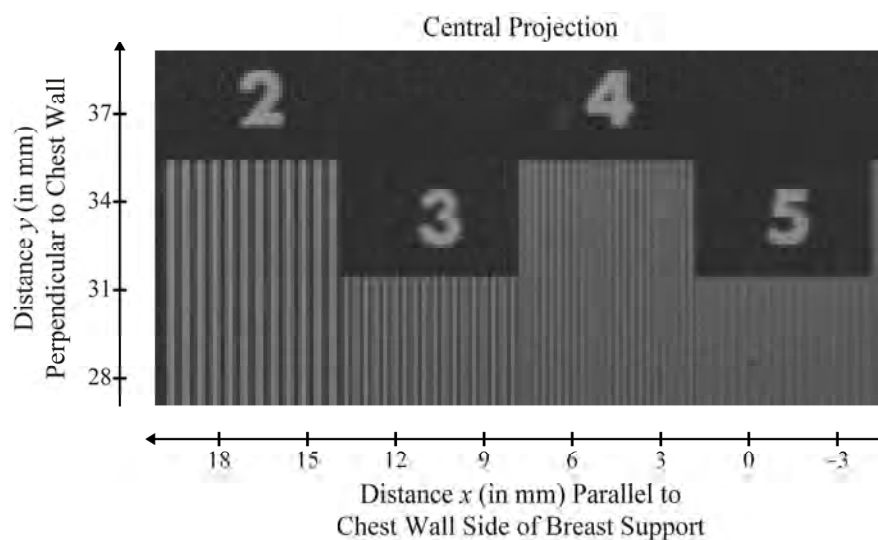
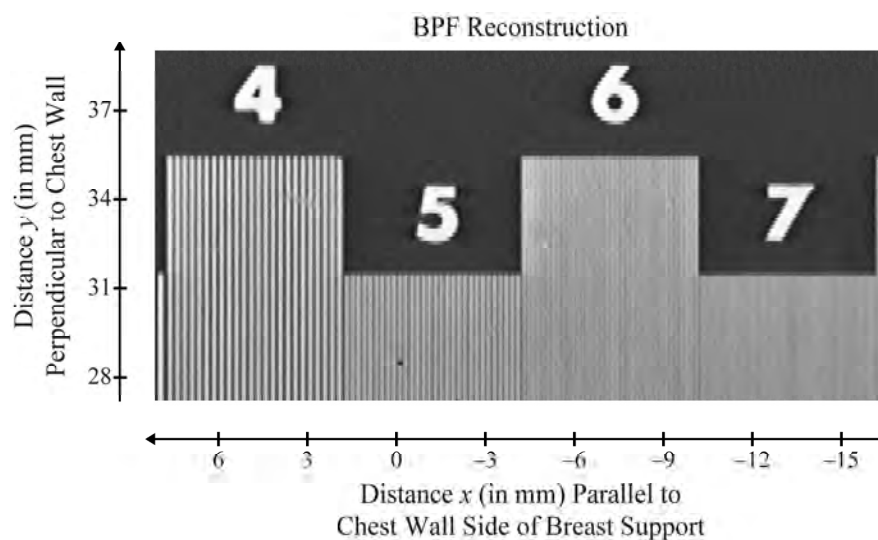


**Figure 8.** The central projection of a bar pattern phantom misrepresents frequencies higher than the detector alias frequency, 3.57 lp/mm for 140  $\mu$ m detector elements. For example, at 4.0 lp/mm, Moiré patterns are present. At 5.0 lp/mm, fewer than 30 line pairs are observed over a 6.0 mm length.





885 **Figure 9.** Unlike the central projection (Figure 8), BPF reconstruction can clearly resolve high  
frequencies along the  $x$  direction parallel to the chest wall side of the breast support. Frequencies  
up to 6.0 lp/mm are resolved with no Moiré patterns or other evidence of aliasing.

890

895

900

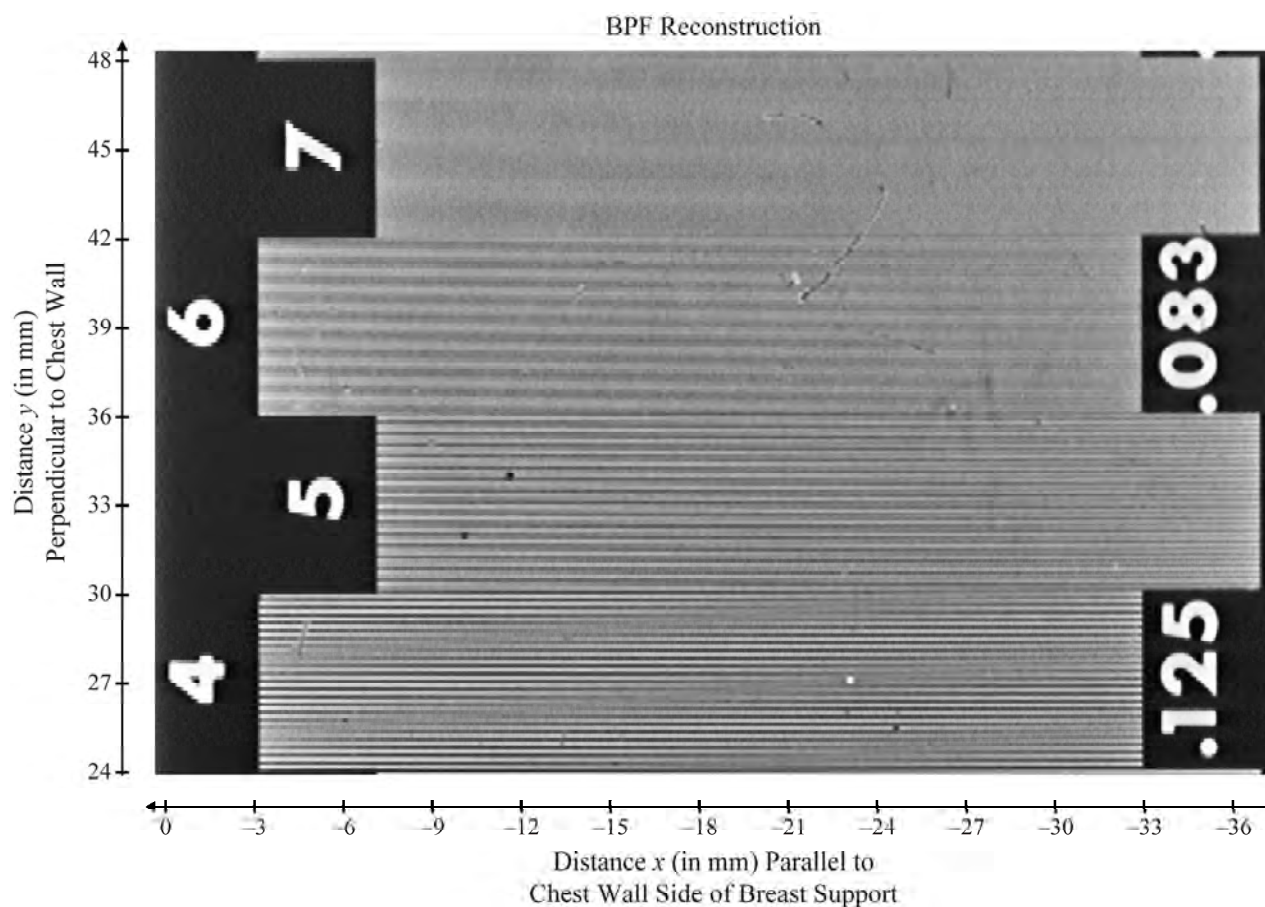


**Figure 10.** Super-resolution along the  $y$  direction is analyzed with bar patterns using a BPF reconstruction. The left edges of the even numerals (“4” and “6”) were aligned on the mid AP/SS plane ( $x = 0$ ), and the separation between 4.0 and 5.0 lp/mm was positioned  $y = 30$  mm from the chest wall. At the extreme left of the bar patterns, less line pairs are visible than expected, illustrating that super-resolution is not achievable near the plane  $x = 0$ . In addition, Moiré patterns at 4.0 lp/mm indicate that super-resolution is not possible too close to the chest wall ( $y = 0$ ). Super-resolution is evident only at positions sufficiently displaced from the planes  $x = 0$  and  $y = 0$ ; see the extreme right of the bar patterns at 5.0 and 6.0 lp/mm.

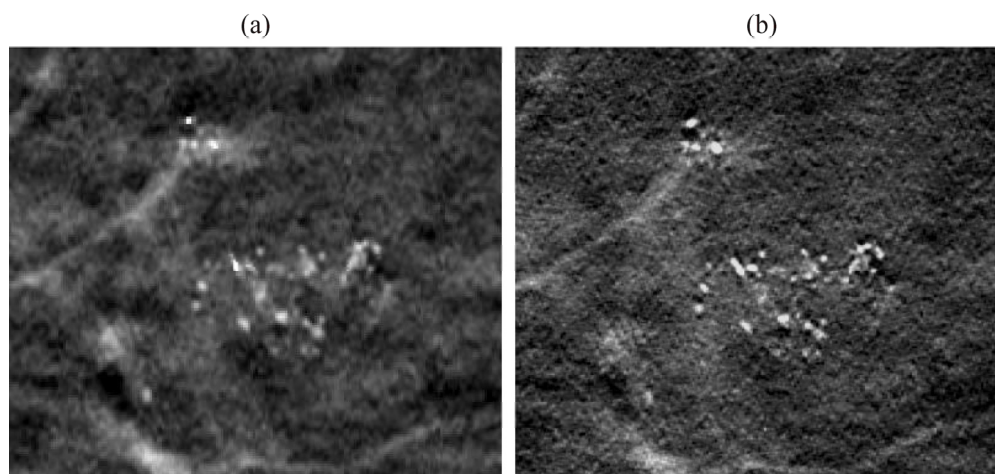


**Figure 11.** Clinical images of microcalcifications are shown. In (a), BPF reconstruction is

performed with pixels of length  $140\text{ }\mu\text{m}$ , and the result is bilinearly interpolated to produce a final  
image with pixels of length  $35\text{ }\mu\text{m}$  (hence, four-fold magnification). In (b), BPF reconstruction is  
performed with pixels of length  $35\text{ }\mu\text{m}$ . As a result of super-resolution, image (b) displays the  
structural morphology of the microcalcifications more clearly, and even shows a few small  
microcalcifications that cannot be discerned in (a).

## REFERENCES

- <sup>1</sup>Rafferty EA. Tomosynthesis: New weapon in breast cancer fight. *Decisions in Imaging Economics*. 2004;17(4).
- <sup>2</sup>Park SC, Park MK, Kang MG. Super-resolution Image Reconstruction: A Technical Overview. 935 *IEEE Signal Processing Magazine*. 2003;20(3):21-36.
- <sup>3</sup>Bushberg JT, Seibert JA, Edwin M. Leidholdt J, Boone JM. Chapter 10: Image Quality. In: John J-R, Snyder A, DeGeorge T, editors. *The Essential Physics of Medical Imaging*. 2 ed. Philadelphia, PA: Lippincott Williams & Wilkins; 2002. p. 255-91.
- <sup>4</sup>Acciavatti RJ, Maidment ADA. Investigating the Potential for Super-Resolution in Digital Breast 940 Tomosynthesis. In: Pelc NJ, Samei E, Nishikawa RM, editors. *SPIE*; 2011; Lake Buena Vista, FL: SPIE; 2011. p. 79615K-1 - K-12.
- <sup>5</sup>Barrett HH, Myers KJ. Chapter 3: Fourier Analysis. In: Saleh BEA, editor. *Foundations of Image Science*. New York, NY: John Wiley & Sons; 2004. p. 95-174.
- <sup>6</sup>Lee DL, Cheung LK, Rodricks B, Powell GF. Improved imaging performance of a 14 x 17-inch 945 Direct Radiography (TM) System using Se/TFT detector. *SPIE Conference on Physics of Medical Imaging*; 1998: SPIE; 1998. p. 14-23.
- <sup>7</sup>Jing T, Goodman CA, Drewery J, Cho G, Hong WS, Lee H, et al. Amorphous silicon pixel layers with cesium iodide converters for medical radiography. *IEEE Trans Nucl Sci*. 1994;41(4):903-9.
- <sup>8</sup>Cowen AR, Kengyelics SM, Davies AG. Solid-state, flat-panel, digital radiography detectors and 950 their physical imaging characteristics. *Clin Radiol*. 2008;63:487-98.
- <sup>9</sup>Nagarkar VV, Gupta TK, Miller SR, Klugerman Y, Squillante MR, Entine G. Structured CsI(Tl) scintillators for x-ray imaging applications. *IEEE Trans Nucl Sci*. 1998;45(3):492-6.
- <sup>10</sup>Stewart J. Chapter 7: Techniques of Integration. In: Pirtle B, Green S, editors. *Calculus: Early Transcendentals*. 5e ed. Belmont, CA: Brooks/Cole - Thomson Learning; 2003. p. 474-545.
- <sup>11</sup>Barrett HH, Myers KJ. Chapter 10: Energy Transport and Photons. In: Saleh BEA, editor. 955 *Foundations of Image Science*. New York, NY: John Wiley & Sons; 2004. p. 551-630.
- <sup>12</sup>Barrett HH, Myers KJ. Chapter 4: Series Expansions and Integral Transforms. In: Saleh BEA, editor. *Foundations of Image Science*. New York, NY: John Wiley & Sons; 2004. p. 175-214.
- <sup>13</sup>Zhao B, Zhao W. Three-dimensional linear system analysis for breast tomosynthesis. 960 *Medical Physics*. 2008;35(12):5219-32.
- <sup>14</sup>Mertelmeier T, Orman J, Haerer W, Dudam MK. Optimizing filtered backprojection reconstruction for a breast tomosynthesis prototype device. In: Flynn MJ, Hsieh J, editors. *Physics of Medical Imaging*; 2006; San Diego: SPIE; 2006.
- <sup>15</sup>Albert M, Maidment ADA. Linear response theory for detectors consisting of discrete arrays. 965 *Medical Physics*. 2000;27(10):2417-34.
- <sup>16</sup>Acciavatti RJ, Maidment ADA. An Analytical Model of NPS and DQE Comparing Photon Counting and Energy Integrating Detectors. In: Samei E, Pelc NJ, editors. *Physics of Medical Imaging*; 2010; San Diego, CA: SPIE; 2010. p. 76220I-1 - I-12.
- <sup>17</sup>Acciavatti RJ, Maidment ADA. A Comparative Analysis of OTF, NPS, and DQE in Energy 970 Integrating and Photon Counting Digital X-ray Detectors. *Medical Physics*. 2010;37(12):6480-95.
- <sup>18</sup>Carton A-K, Bakic P, Ullberg C, Maidment ADA. Development of a 3D high-resolution physical anthropomorphic breast phantom. In: Samei E, Pelc NJ, editors. *Medical Imaging 2010: Physics of Medical Imaging*; 2010; San Diego, CA: SPIE; 2010. p. 762206-1 - -8.
- <sup>19</sup>Carton A-K, Bakic P, Ullberg C, Derand H, Maidment ADA. Development of a physical 3D 975 anthropomorphic breast phantom. *Medical Physics*. 2011;38(2):891-6.
- <sup>20</sup>Wolbarst AB. Chapter 30: Resolution and Magnification. *Physics of Radiology*. 2nd ed. Madison, WI: Medical Physics Publishing; 2005. p. 333-40.

- <sup>21</sup>Albert M, Beideck DJ, Bakic PR, Maidment ADA. Aliasing effects in digital images of line-pair phantoms. *Medical Physics*. 2002;29(8):1716-8.
- 980 <sup>22</sup>Lanyi M. Chapter 7: Differential Diagnosis of Microcalcifications. *Diagnosis and Differential Diagnosis of Breast Calcifications*. Berlin: Springer-Verlag; 1988. p. 193-231.
- <sup>23</sup>Que W, Rowlands JA. X-ray imaging using amorphous selenium: Inherent spatial resolution. *Medical Physics*. 1995;22(4):365-74.
- 985 <sup>24</sup>Hajdok G, Cunningham IA. Penalty on the detective quantum efficiency from off-axis incident x rays. In: Yaffe MJ, Flynn MJ, editors. *Medical Imaging 2004: Physics of Medical Imaging*; 2004; San Diego: SPIE; 2004. p. 109-18.
- <sup>25</sup>Mainprize JG, Bloomquist AK, Kempston MP, Yaffe MJ. Resolution at oblique incidence angles of a flat panel imager for breast tomosynthesis. *Medical Physics*. 2006;33(9):3159-64.
- 990 <sup>26</sup>Acciavatti RJ, Maidment ADA. Calculation of OTF, NPS, and DQE for Oblique X-Ray Incidence on Turbid Granular Phosphors. *Lecture Notes in Computer Science*. 2010;6136:436-43.
- <sup>27</sup>Acciavatti RJ, Maidment ADA. Optimization of phosphor-based detector design for oblique x-ray incidence in digital breast tomosynthesis. *Medical Physics*. 2011;38(11):6188-202.
- <sup>28</sup>Johns PC, Yaffe MJ. X-ray Characterization of normal and neoplastic breast tissues. *Physics in Medicine and Biology*. 1987;32(6):675-95.
- 995 <sup>29</sup>Yaffe MJ. Chapter 5: Digital Mammography. In: Beutel J, Kundel HL, Metter RLV, editors. *Handbook of Medical Imaging Volume 1 Physics and Psychophysics*. Bellingham, WA: SPIE - The International Society for Optical Engineering; 2000. p. 329-72.
- <sup>30</sup>Bushberg JT, Seibert JA, Edwin M. Leidholdt J, Boone JM. Chapter 8: Mammography. In: John J-R, Snyder A, DeGeorge T, editors. *The Essential Physics of Medical Imaging*. 2 ed. Philadelphia, PA: Lippincott Williams & Wilkins; 2002. p. 191-229.
- 1000 <sup>31</sup>Berger MJ, Hubbell JH, Seltzer SM, Chang J, Coursey JS, Sukumar R, et al. XCOM: Photon Cross Sections Database. [cited 2011 November 10]; Available from: <http://physics.nist.gov/xcom>
- <sup>32</sup>Johns HE, Cunningham JR. Chapter 16: Diagnostic Radiology. *The Physics of Radiology*. 4th ed. Springfield, IL: Charles C Thomas; 1983. p. 557-669.
- 1005 <sup>33</sup>Ren B, Ruth C, Stein J, Smith A, Shaw I, Jing Z. Design and performance of the prototype full field breast tomosynthesis system with selenium based flat panel detector. In: Flynn MJ, editor. *SPIE*; 2005; San Diego, CA: SPIE; 2005. p. 550-61.
- <sup>34</sup>Bloomquist AK, Yaffe MJ, Mawdsley GE, Hunter DM. Lag and ghosting in a clinical flat-panel selenium digital mammography system. *Medical Physics*. 2006;33(8):2998-3005.
- 1010 <sup>35</sup>Siewerdsen JH, Jaffray DA. A ghost story: Spatio-temporal response characteristics of an indirect-detection flat-panel imager. *Medical Physics*. 1999;26(8):1624-41.
- <sup>36</sup>Zhao W, DeCrescenzo G, Kasap SO, Rowlands JA. Ghosting caused by bulk charge trapping in direct conversion flat-panel detectors using amorphous selenium. *Medical Physics*. 2005;32(2):488-500.
- 1015 <sup>37</sup>Barrett HH, Myers KJ. Chapter 12: Noise in Detectors. In: Saleh BEA, editor. *Foundations of Image Science*. New York, NY: John Wiley & Sons; 2004. p. 701-800.
- <sup>38</sup>Tucker DM, Barnes GT, Chakraborty DP. Semiempirical model for generating tungsten target x-ray spectra. *Medical Physics*. 1991;18(2):211-8.
- <sup>39</sup>Boone JM, Fewell TR, Jennings RJ. Molybdenum, rhodium, and tungsten anode spectral models using interpolating polynomials with application to mammography. *Medical Physics*. 1997;24(12):1863-74.
- 1020 <sup>40</sup>Blough MM, Waggener RG, Payne WH, Terry JA. Calculated mammographic spectra confirmed with attenuation curves for molybdenum, rhodium, and tungsten targets. *Medical Physics*. 1998;25(9):1605-12.

- 1025 <sup>41</sup>Lauritsch G, Harer WH. A theoretical framework for filtered backprojection in tomosynthesis. Imaging Processing; 1998; San Diego: SPIE; 1998. p. 1127-37.
- <sup>42</sup>Kunze H, Haerer W, Orman J, Mertelmeier T, Stierstorfer K. Filter determination for tomosynthesis aided by iterative reconstruction techniques. 9th International Meeting on Fully Three-Dimensional Image Reconstruction in Radiology and Nuclear Medicine; 2007 July 9-13; Lindau, Germany; 2007. p. 309-12.
- 1030 <sup>43</sup>Bakic PR, Zhang C, Maidment ADA. Development and characterization of an anthropomorphic breast software phantom based upon region-growing algorithm. Medical Physics. 2011;38(6):3165-76.
- <sup>44</sup>Stewart J. Chapter 15: Multiple Integrals. In: Pirtle B, Green S, editors. Calculus: Early Transcendentals. 5e ed. Belmont, CA: Brooks/Cole - Thomson Learning; 2003. p. 980-1053.
- 1035

[Jump to Content](#)

[Increase text size](#)[Decrease text size](#)

[Sign In](#)[View Cart](#)[Help](#)

# Medical Physics

The International Journal of Medical Physics Research and Practice

Volume/PageKeywordDOI Citation Advanced

Your Google Scholar search was "raymond acciavatti - experimental and theoretical"

raymond acciavatti - experimental and t

Peer-reviewed articles

[Home](#)[Browse](#)[About](#)[Authors](#)[Librarians](#)[Track](#)[Advertisers](#)[Scitation](#)[Special Publications](#)[MedPhys Home](#)[AAPM](#)

Your access to this publication is provided through the subscription of Univ of Pennsylvania Library.

Medical Physics / Volume 38 / Issue 6 / 2011 JOINT AAPM/COMP MEETING PROGRAM / IMAGING  
SCIENTIFIC SESSION: ROOM 301

Med. Phys. 38, 3746 (2011); doi:10.1118/1.3613097 (1 page)

# TU A 301 07: Experimental and Theoretical Validation of Breast Tomosynthesis Reconstructions along Oblique Planes

R Acciavatti and A Maidment  
University of Pennsylvania, Philadelphia, PA

[View Map](#)



**Abstract**

Full Text: [Download PDF](#) | [View Cart](#)

[Alerts](#)[Tools](#)[Share](#)

Purpose: Digital breast tomosynthesis (DBT) is a 3D imaging modality in which tomographic sections of the breast are generated from a limited range of x ray projections. Conventional practice is to perform reconstructions possessing pitches within the angular range of the DBT scan, since the Central Slice theorem states that Fourier space is sampled within double napped cones (DNCs) whose opening angle matches that angular range. This work investigates the possibility for both resolution and super resolution (i.e., sub pixel resolution) outside the angular range of the DNCs.Methods: Because the image of an object is translated in sub pixel detector element increments with each projection, our prior work has demonstrated that DBT is capable of super resolution. The previous study assumed a reconstruction plane parallel to the breast support; our current work analyzes super resolution in oblique reconstruction planes. Experimentally, a bar pattern phantom was imaged with a commercial DBT system using a goniometry stand, and reconstruction was performed in the oblique plane of the bar patterns. Clinical images of microcalcifications were similarly reconstructed in various oblique planes. Subsequently, an analytical framework for investigating super resolution in oblique reconstructions was developed by calculating the filtered backprojection (FBP) reconstruction of a high frequency sine input.Results: Bar pattern reconstructions showed visibility of frequencies both less than and greater than the alias frequency of the detector at pitches well outside the angular range of the DBT scan. Visibility of microcalcifications did not differ considerably using similar oblique reconstruction planes. For analytical proof of super resolution in oblique reconstruction planes, we demonstrated that FBP could properly resolve a high frequency sine input whose Fourier transform is non vanishing outside the DNCs of frequency space. Conclusions: This work provides a platform for investigating super resolution in oblique reconstruction planes whose pitches are outside the angular range of the DBT scan.

**PUBLICATION DATA**

[Alert Me When Cited](#)

**ISSN:**

[Alert Me When Corrected](#)

**Publisher:**

American Association of Physicists in Medicine



Permalink



<http://dx.doi.org/10.1118/1.3613097>

OpenURL



**Medical Physics is the scientific journal of the American Association of Physicists in Medicine**

William R. Hendee, Editor

Departments of Radiology, Radiation Oncology, Biophysics, Community and Public Health, Medical College of Wisconsin

One Physics Ellipse

College Park, Maryland 20740

301-209-3352

© 2011, American Association of Physicists in Medicine. Individual readers of this journal, and nonprofit libraries acting for them, are freely permitted to make fair use of the material in it, such as to copy an article for use in teaching or research. (For other kinds of copying see "Copying Fees.") Permission is granted to quote from this journal in scientific works with the customary acknowledgment of the source. To reprint a figure, table, or other excerpt requires, in addition, AAPM may require that permission also be obtained from one of the authors. Address inquiries and notices to Penny Slattery, Journal Manager, Medical Physics Journal, AAPM, One Physics Ellipse, College Park, MD 20740-3846; email: [journal@aapm.org](mailto:journal@aapm.org).



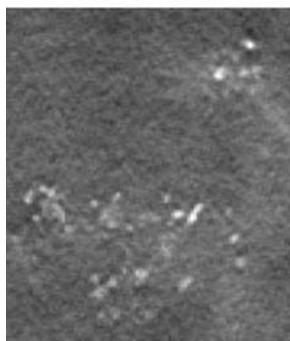
**Poster P35-22**

BC101145-3282

**AN ANALYSIS OF SUPER-RESOLUTION IN OBLIQUE RECONSTRUCTIONS FOR DIGITAL BREAST TOMOSYNTHESIS****Raymond Joseph Acciavatti and Andrew Douglas Arnold Maidment**

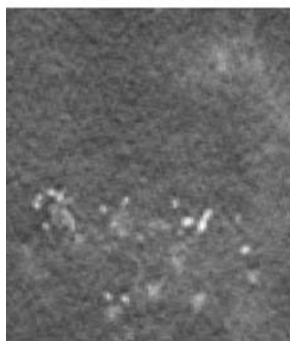
University of Pennsylvania

0° Pitch



Super-resolution reconstruction of microcalcifications along a plane parallel to the breast support

30° Pitch



Super-resolution reconstruction of microcalcifications along an oblique plane

In digital breast tomosynthesis (DBT), tomographic sections of the breast are generated from x-ray projections acquired over a limited range of tube angles. Because the image of an object is shifted in subpixel increments with increasing projection angle, we have previously shown that DBT is capable of super-resolution (i.e., subpixel resolution). This previous work assumed a reconstruction plane parallel to the breast support; it is now clear that super-resolution is also achievable along an oblique reconstruction plane. A theoretical framework for investigating super-resolution has been developed in which the reconstruction of a high-frequency sine input is calculated. With this model, we show that filtered backprojection can resolve the input over a range of angular pitches. The feasibility of this concept was verified with a commercial DBT system (Selenia Dimensions, Hologic, Bedford, Massachusetts) and a commercial prototype reconstruction solution (Briona, Real Time Tomography, Villanova, Pennsylvania). Using a goniometry stand, images of a bar pattern at oblique angles relative to the breast support were

acquired and successfully reconstructed. To demonstrate the clinical importance of these findings, reconstructions of microcalcifications were performed along oblique planes whose pixel sizes ( $28\text{ }\mu\text{m}$ ) are much smaller than the detector elements ( $140\text{ }\mu\text{m}$ ). As shown, the visibility of microcalcifications in the lower half of the figures is not compromised by using a  $30^\circ$  pitch. The upper right calcifications are not visible with the  $30^\circ$  pitch as they are out of the reconstruction plane; visualization is achieved by simply translating the plane of reconstruction. In conclusion, this work demonstrates the feasibility of super-resolution in oblique DBT reconstructions and has applications in the visualization of microcalcifications and other subtle signs of breast cancer.

---

*This work was supported by the U.S. Army Medical Research and Materiel Command under W81XWH-11-1-0100.*

# **Optimization of Continuous Tube Motion and Step-and-Shoot Motion in Digital Breast Tomosynthesis Systems with Patient Motion**

Raymond J. Acciavatti and Andrew D. A. Maidment

University of Pennsylvania, Department of Radiology, 3400 Spruce St., Philadelphia PA 19104

E-mail:racci@seas.upenn.edu and Andrew.Maidment@uphs.upenn.edu

## **ABSTRACT**

In digital breast tomosynthesis (DBT), a reconstruction of the breast is generated from projections acquired over a limited range of x-ray tube angles. There are two principal schemes for acquiring projections, continuous tube motion and step-and-shoot motion. Although continuous tube motion has the benefit of reducing patient motion by lowering scan time, it has the drawback of introducing blurring artifacts due to focal spot motion. The purpose of this work is to determine the optimal scan time which minimizes this trade-off. To this end, the filtered backprojection reconstruction of a sinusoidal input is calculated. At various frequencies, the optimal scan time is determined by the value which maximizes the modulation of the reconstruction. Although prior authors have studied the dependency of the modulation on focal spot motion, this work is unique in also modeling patient motion. It is shown that because continuous tube motion and patient motion have competing influences on whether scan time should be long or short, the modulation is maximized by an intermediate scan time. This optimal scan time decreases with object velocity and increases with exposure time. To optimize step-and-shoot motion, we calculate the scan time for which the modulation attains the maximum value achievable in a comparable system with continuous tube motion. This scan time provides a threshold below which the benefits of step-and-shoot motion are justified. In conclusion, this work optimizes scan time in DBT systems with patient motion and either continuous tube motion or step-and-shoot motion by maximizing the modulation of the reconstruction.

**Keywords:** Digital breast tomosynthesis (DBT), continuous tube motion, step-and-shoot motion, patient motion, image reconstruction, filtered backprojection, modulation, optimization.

## **1. INTRODUCTION**

Digital breast tomosynthesis (DBT) is a 3D imaging modality in which tomographic sections of the breast are generated from a limited range of x-ray projections. Preliminary studies indicate that DBT has increased sensitivity and specificity for early cancer detection relative to conventional 2D digital mammography.<sup>1</sup> There are two main schemes for acquiring projection images in DBT, step-and-shoot motion and continuous tube motion. Systems with continuous tube motion have the benefit of shorter scan time and thus less patient motion; the trade-off is increased blurring due to focal spot motion. Using a prototype DBT system (Hologic Inc., Bedford, MA), Ren *et al.* showed that blurring due to focal spot motion increases with height above the breast support. At a 4.0 cm height, the projected distance traveled by the focal spot during a single exposure is approximately half the detector element length.<sup>2</sup>

According to Zhao, focal spot motion degrades the modulation transfer function (MTF) of each projection by  $\text{sinc}(a_1 f_r)$ , where  $a_1$  is the projected distance traveled by the focal spot and  $f_r$  is radial frequency perpendicular to the ray of incidence. Because focal spot motion has no effect on noise power spectra (NPS), the degradation in detective quantum efficiency (DQE) is more pronounced than the degradation in MTF due to the dependency of DQE on the square of MTF. At the alias frequency of 5.9 line pairs per millimeter (lp/mm) in a prototype system, Zhao found that focal spot motion degrades MTF and DQE by 30% and 50%, respectively.<sup>3</sup>

In order to minimize the blurring due to focal spot motion in a system with continuous tube motion, Bissonnette *et al.* proposed lengthening the scan time. They demonstrated that a 39 s scan time effectively eliminated image quality degradation due to focal spot motion in a prototype Siemens Novation<sup>TM</sup> system.<sup>4</sup> Unfortunately, it is not practical to employ a long scan time as it permits greater patient motion.

Figure 1 illustrates the blurring due to patient motion in clinical images acquired with the Selenia Dimensions system (Hologic Inc., Bedford, MA) and reconstructed with a commercial prototype backprojection filtering algorithm (Briona, Real Time Tomography, Villanova, PA). A small region of interest (ROI) with two microcalcifications at the height 22.0 mm above the breast support is shown. This depth was found to minimize the motion of the microcalcifications in the 15 individual backprojections, and thus is the height above the breast support at which the microcalcifications are in focus. By comparing the positions of the microcalcifications relative to a fixed marker (×) among all backprojections at the 22.0 mm depth, the net displacements of the microcalcifications in the mediolateral direction (top-to-bottom in the figure) and the chest wall-to-nipple direction (left-to-right in the figure) are approximately 140  $\mu\text{m}$  and 280  $\mu\text{m}$ , respectively, corresponding to one- and two-times the length of a detector element. With a 3.7 s scan time, the microcalcification velocities are thus 38  $\mu\text{m/s}$  and 76  $\mu\text{m/s}$  in these two respective directions. The microcalcifications appear blurry and artificially enlarged in the reconstruction as a result of patient motion.

Although image quality degradation due to continuous tube motion has been modeled by many authors, no one has incorporated patient motion into the analysis. Because these two types of motion have competing influences on whether scan time should be very long or very short, one would expect image quality to be optimized by an intermediate scan time. For this reason, the purpose of this work is to determine the optimal scan time by maximizing the modulation of the reconstruction at various frequencies. To optimize step-and-shoot motion in a similar fashion, we calculate the scan time for which the modulation matches the maximum value achievable in a comparable system with continuous tube motion. This scan time provides a threshold below which the benefits of step-and-shoot motion are justified.

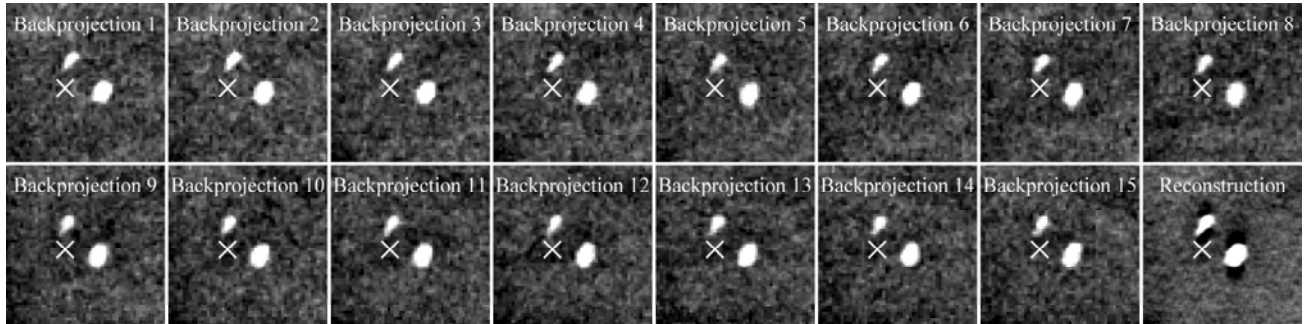


**Figure 1.** Backprojections of identical ROIs of clinical tomosynthesis images at a 22.0 mm height above the breast support are shown. This height was found to minimize the motion of the microcalcifications, ensuring that the microcalcifications are in focus in the corresponding reconstructed slice. The microcalcifications shift position relative to a fixed marker (×) in the 15 individual backprojections. Such patient motion causes blurring and artificial enlargement of the microcalcifications in the reconstruction.

## 2. METHODS

### 2.1 Acquisition Geometry for Continuous Tube Motion (CTM)

In order to calculate the scan time which optimizes the modulation of a DBT reconstruction at various frequencies, it is first necessary to model the acquisition geometry. We simulate a DBT system in which the detector rotates in synchrony with the x-ray tube during the acquisition of the projections. As diagrammed schematically in Figure 2, the x-ray tube rotates within the plane of the chest wall (*i.e.*, the  $xz$  plane) about the origin  $O$ , corresponding to midpoint of the chest wall side of the detector. In addition, the detector rotates about the  $y$  axis, with  $O$  acting as the pivot point. At the x-ray tube angle  $\psi$  relative to the  $z$  axis, the detector rotation angle ( $\gamma$ ) is found from the ratio  $\psi/g$ , where  $g$  is the gear ratio of the detector. Positive directionalities of  $\psi$  and  $\gamma$  are defined as those presented in Figure 2, and in the limit  $g \rightarrow \infty$ , a stationary detector can be recovered ( $\gamma \rightarrow 0$ ).

In a system with continuous tube motion at a constant angular velocity  $\omega$ , each projection is acquired over the exposure time  $\tau$  as the tube is swept over the angular extent  $\Psi = \omega\tau$ . For the  $n^{\text{th}}$  projection, the x-ray tube arc is centered about the angle  $\psi_n = n\Delta\psi$ , so that the x-ray tube angle varies between  $\psi = \psi_n + \Psi/2$  and  $\psi = \psi_n - \Psi/2$  during the exposure time  $\tau$ . In the literature,  $\psi_n$  is often termed the nominal projection angle and  $\Delta\psi$  the angular spacing between projections.<sup>5</sup> With an odd number of  $N$  total projections, the index  $n$  varies between  $-(N-1)/2$  and  $(N-1)/2$ , and the special case  $n = 0$  defines the central projection. Denoting the total scan time as  $T_s$ , the total angular range of the x-ray tube motion can be

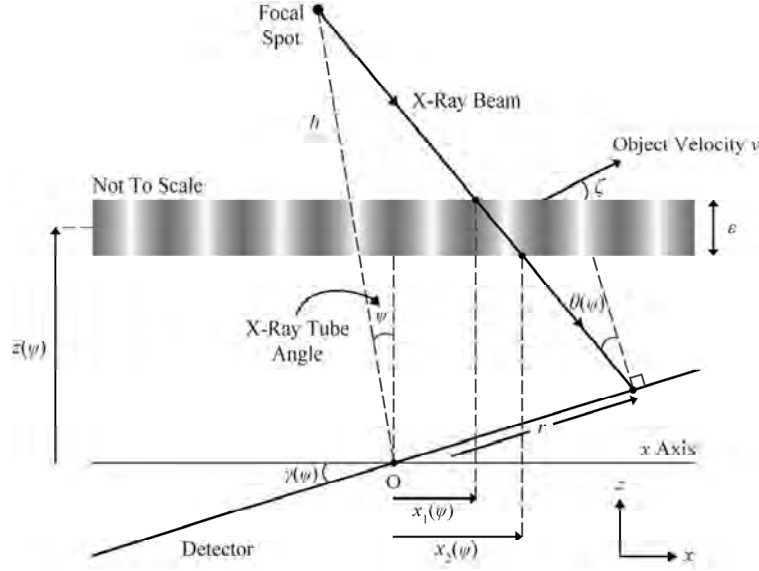


**Figure 2.** A diagram of the acquisition geometry is shown (not to scale). The attenuation coefficient of the input object varies sinusoidally along the  $x$  direction. To model patient motion, the input object has velocity  $v$  at the angle  $\zeta$  relative to the  $x$  direction.

written as  $\omega T_t$ , or equivalently, as the difference between the initial x-ray tube angle ( $\psi_i$ ) and the final x-ray tube angle ( $\psi_f$ ).

$$\omega T_t = \psi_i - \psi_f = \left( \frac{N-1}{2} \right) \Delta\psi + \frac{\Psi}{2} - \left[ -\left( \frac{N-1}{2} \right) \Delta\psi - \frac{\Psi}{2} \right] = (N-1) \Delta\psi + \Psi \quad (1)$$

Substituting  $\omega = \Psi/\tau$  in the left-hand side of Eq. (1), the angular sweep of the x-ray tube over the exposure time  $\tau$  can be expressed in terms of the total scan time  $T_t$  instead of the tube's angular velocity  $\omega$ .

$$\Psi = \left( \frac{N-1}{T_t - \tau} \right) \tau \Delta\psi \quad (2)$$

This formula for  $\Psi$  is useful as the total scan time is more directly measurable than the tube's angular velocity.

## 2.2 Detector Signal for Sinusoidal Input to CTM System

A framework for investigating tube motion and patient motion in DBT is now developed by calculating the modulation of the reconstruction of a sinusoidal input. Accordingly, suppose that a thin rectangular plate with its long axis parallel to the breast support possesses a linear attenuation coefficient  $\mu(x, z)$  which varies sinusoidally with position  $x$ . Although an actual input to a clinical breast imaging system would be 3D, a 2D construct is a useful tool for simulating measurements in the plane of the chest wall. The extension of this framework to measurements made perpendicular to the chest wall is reserved for future work.

As shown in Figure 2, the rectangular plate is positioned between  $z = \tilde{z}(\psi) - \varepsilon/2$  and  $z = \tilde{z}(\psi) + \varepsilon/2$ , where  $\tilde{z}(\psi)$  is the central height of the plate above the detector at the x-ray tube angle  $\psi$  and  $\varepsilon$  is the plate's thickness. The height  $\tilde{z}(\psi)$  is taken to be dependent upon the x-ray tube angle  $\psi$  in order to model the presence of patient motion. For an input frequency  $f_0$ , the attenuation coefficient may be written

$$\mu(x, z) = C \cdot \cos\left(2\pi f_0 [x - \tilde{x}(\psi)]\right) \cdot \text{rect}\left[\frac{z - \tilde{z}(\psi)}{\varepsilon}\right], \quad \text{rect}(u) \equiv \begin{cases} 1 & , |u| \leq 1/2 \\ 0 & , |u| > 1/2 \end{cases} \quad (3)$$

where  $C$  is the amplitude of the sinusoidal waveform and  $\tilde{x}(\psi)$  is its translational shift along the  $x$  direction. Provided that  $|z - z_0| \leq \varepsilon$ , the Fourier transform of Eq. (3) along the  $x$  direction is a linear sum of delta functions<sup>5</sup> which peak at the frequencies  $f = \pm f_0$ . Typically, only the positive frequency  $f = +f_0$  is of interest in an experimental measurement. Hence, although it is non-physical for a linear attenuation coefficient to vary between negative and positive values, formulating  $\mu(x, z)$  by Eq. (3) is helpful for a thought experiment in the reconstruction of a single input frequency.

In Figure 2, the displacements  $x_1(\psi)$  and  $x_2(\psi)$  determine the entrance and exit points of the x-ray beam through the sine plate for an arbitrary incident point on the detector at a distance  $r$  from O. Following our previous work,<sup>5</sup>  $x_1(\psi)$  and  $x_2(\psi)$  can be written as  $x_1(\psi) = \rho(\psi) \cdot r - \lambda^+(\psi)$  and  $x_2(\psi) = \rho(\psi) \cdot r - \lambda^-(\psi)$ , where  $\rho(\psi) \equiv \cos[\gamma(\psi)] + \sin[\gamma(\psi)]\tan[\theta(\psi) + \gamma(\psi)]$  and  $\lambda^\pm(\psi) \equiv [\tilde{z}(\psi) \pm \varepsilon/2] \cdot \tan[\theta(\psi) + \gamma(\psi)]$ . The expression for the incident angle relative to the normal to the detector also follows from our previous work

$$\theta(\psi) = -\gamma(\psi) + \arctan\left(\frac{h \sin \psi + r \cos[\gamma(\psi)]}{h \cos \psi - r \sin[\gamma(\psi)]}\right), \quad (4)$$

where  $h$  is the source-to-origin distance (Figure 2). Total attenuation  $\mathcal{A}\mu(\psi)$  recorded by the x-ray converter at the tube angle  $\psi$  may now be calculated by integrating the attenuation coefficient of the sine plate over the path length  $\mathcal{L}(\psi)$ .

$$\mathcal{A}\mu(\psi) = \int_{\mathcal{L}(\psi)} \mu ds = \int_{x_1(\psi)}^{x_2(\psi)} C \cdot \cos(2\pi f_0 [x - \tilde{x}(\psi)]) \cdot \csc[\theta(\psi) + \gamma(\psi)] dx \quad (5)$$

In order to calculate the total attenuation  $\mathcal{A}\mu(n)$  recorded by the x-ray converter for the  $n^{\text{th}}$  projection, one must integrate  $\mathcal{A}\mu(\psi)$  over the angular arc swept by the x-ray tube during the exposure time  $\tau$ .

$$\mathcal{A}\mu(n) = \int_{\psi_n - \Psi/2}^{\psi_n + \Psi/2} \int_{x_1(\psi)}^{x_2(\psi)} C \cdot \cos(2\pi f_0 [x - \tilde{x}(\psi)]) \cdot \csc[\theta(\psi) + \gamma(\psi)] dx d\psi \quad (6)$$

$$= \frac{C}{2\pi f_0} \int_{\psi_n - \Psi/2}^{\psi_n + \Psi/2} \csc[\theta(\psi) + \gamma(\psi)] \cdot \left[ \begin{array}{l} \sin(2\pi f_0 [\rho(\psi) \cdot r - \lambda^-(\psi) - \tilde{x}(\psi)]) \\ -\sin(2\pi f_0 [\rho(\psi) \cdot r - \lambda^+(\psi) - \tilde{x}(\psi)]) \end{array} \right] d\psi \quad (7)$$

Eq. (7) provides an expression for signal intensity versus position  $r$  along the detector, assuming that the detector is non-pixelated and possesses a modulation transfer function (MTF) of unity at all frequencies. An amorphous selenium (a-Se) photoconductor operated in drift mode is a good approximation for a detector with these properties.<sup>6</sup>

Total attenuation for the  $n^{\text{th}}$  projection can now be simplified using a sum-to-product trigonometric identity for real numbers  $\alpha$  and  $\beta$ ; namely,  $\sin\alpha - \sin\beta = 2\cos[(\alpha + \beta)/2]\sin[(\alpha - \beta)/2]$

$$\mathcal{A}\mu(n) = C\varepsilon \int_{\psi_n - \Psi/2}^{\psi_n + \Psi/2} \sec[\theta(\psi) + \gamma(\psi)] \text{sinc}[\varepsilon f_0 \tan[\theta(\psi) + \gamma(\psi)]] \cdot \cos[2\pi f_0 [\rho(\psi) \cdot r - \tilde{z}(\psi) \cdot \tan[\theta(\psi) + \gamma(\psi)] - \tilde{x}(\psi)]] d\psi, \quad (8)$$

where  $\text{sinc}(u) \equiv \sin(\pi u)/(\pi u)$ . Because it is difficult to perform the integration in Eq. (8) in closed form, it is necessary to use approximation techniques. One such method is the midpoint formula. For the  $n^{\text{th}}$  projection, the angular sweep of the x-ray tube can be divided into  $K$  intervals between  $\psi = \psi_n + \Psi/2$  and  $\psi = \psi_n - \Psi/2$ . The tube angle at the midpoint of the  $k^{\text{th}}$  interval is

$$\psi_{kn} = \psi_n - \frac{\Psi}{2} \left(1 - \frac{2k-1}{K}\right) = \left[n - \frac{\tau}{2} \left(\frac{N-1}{T_i - \tau}\right) \left(1 - \frac{2k-1}{K}\right)\right] \Delta\psi, \quad k \in \mathbb{N}. \quad (9)$$

Eq. (8) can now be evaluated by averaging the integrand over each of the  $K$  intervals in the limit of infinite  $K$

$$\mathcal{A}\mu(n) = \lim_{K \rightarrow \infty} \frac{C\varepsilon}{K} \sum_{k=1}^K \sec(\theta_{kn} + \gamma_{kn}) \text{sinc}[\varepsilon f_0 \tan(\theta_{kn} + \gamma_{kn})] \cos[2\pi f_0 [\rho_{kn} r - \tilde{z}_{kn} \tan(\theta_{kn} + \gamma_{kn}) - \tilde{x}_{kn}]], \quad (10)$$

where  $\theta_{kn}$ ,  $\gamma_{kn}$ , and  $\rho_{kn}$  are calculated by evaluating  $\theta(\psi)$ ,  $\gamma(\psi)$ , and  $\rho(\psi)$  at  $\psi = \psi_{kn}$ . In Eq. (10), the displacements  $\tilde{x}_{kn}$  and  $\tilde{z}_{kn}$  determine the position of the sine plate at the time point  $T_{kn}$ . The special case  $T_{kn} = 0$  is defined to occur at the x-ray tube angle  $\psi = 0$ , so that the scan time occurs between the time points  $-T_t/2$  and  $T_t/2$ .

$$T_{kn} = \frac{\psi_{kn}}{\omega} = \frac{\tau \psi_{kn}}{\Psi} = \left( \frac{T_t - \tau}{N - 1} \right) \frac{\psi_{kn}}{\Delta \psi}, \quad -\frac{T_t}{2} \leq T_{kn} \leq \frac{T_t}{2} \quad (11)$$

To model the presence of patient motion, the sine plate is taken to have constant velocity  $v$  at the angle  $\zeta$  relative to the  $x$  direction (Figure 2). The displacements  $\tilde{x}_{kn}$  and  $\tilde{z}_{kn}$  can be written in terms of the velocity components  $v_x$  and  $v_z$  as

$$\tilde{x}_{kn} = x_0 + T_{kn} v_x = x_0 + \left( \frac{T_t - \tau}{N - 1} \right) \frac{v \psi_{kn} \cos \zeta}{\Delta \psi}, \quad \tilde{z}_{kn} = z_0 + T_{kn} v_z = z_0 + \left( \frac{T_t - \tau}{N - 1} \right) \frac{v \psi_{kn} \sin \zeta}{\Delta \psi}, \quad (12)$$

where  $x_0$  and  $z_0$  are positions which determine the location of the sine plate at the x-ray tube angle  $\psi = 0$ .

In a digital detector, the  $a$ -Se x-ray converter is placed in electrical contact with a large area plate of amorphous silicon ( $a$ -Si) in which a thin-film transistor (TFT) array samples the total attenuation in pixels (*i.e.*, detector elements). Using Eq. (10), the logarithmically-transformed signal in the  $m^{\text{th}}$  detector element for the  $n^{\text{th}}$  projection is

$$\mathcal{D}\mu(m, n) = \int_{a(m-1/2)}^{a(m+1/2)} \mathcal{A}\mu(n) \cdot \frac{dr}{a}. \quad (13)$$

Detector elements are taken to be centered on  $r = ma$ , and the detector element containing O is the one corresponding to  $m = 0$ . Because the incident angle varies minimally within each detector element, the integration in Eq. (13) can be evaluated by approximating the incident angle  $\theta_{kn}$  with its value at the centroid of the detector element. Thus

$$\mathcal{D}\mu(m, n) = \lim_{K \rightarrow \infty} \sum_{k=1}^K \frac{C\varepsilon \sec(\theta_{kmn} + \gamma_{kn}) \cdot \text{sinc}[\varepsilon f_0 \tan(\theta_{kmn} + \gamma_{kn})]}{2\pi f_0 K \rho_{kmn}} \left[ \frac{\sin[2\pi f_0 (a \rho_{kmn} (m + 1/2) - \tilde{z}_{kn} \tan(\theta_{kmn} + \gamma_{kn}) - \tilde{x}_{kn})]}{-\sin[2\pi f_0 (a \rho_{kmn} (m - 1/2) - \tilde{z}_{kn} \tan(\theta_{kmn} + \gamma_{kn}) - \tilde{x}_{kn})]} \right] \quad (14)$$

where  $\theta_{kmn}$  and  $\rho_{kmn}$  are calculated by evaluating  $\theta_{kn}$  and  $\rho_{kn}$  at  $r = ma$ . Eq. (14) can be simplified further by using the sum-to-product trigonometric identity described previously.

$$\mathcal{D}\mu(m, n) = \lim_{K \rightarrow \infty} \frac{C\varepsilon}{K} \sum_{k=1}^K \sec(\theta_{kmn} + \gamma_{kn}) \cdot \text{sinc}[\varepsilon f_0 \tan(\theta_{kmn} + \gamma_{kn})] \cdot \text{sinc}[a \rho_{kmn} f_0] \cdot \cos[2\pi f_0 [ma \rho_{kmn} - \tilde{z}_{kn} \tan(\theta_{kmn} + \gamma_{kn}) - \tilde{x}_{kn}]] \quad (15)$$

### 2.3 Detector Signal for Step-and-Shoot Motion (SSM)

In a similar fashion, detector signal for a system with step-and-shoot motion can be calculated. All expressions between Eqs. (4) and (8) continue to hold, so that the total attenuation recorded by the x-ray converter for the  $n^{\text{th}}$  projection is

$$\mathcal{A}\mu(n) = C\varepsilon \sec(\theta_n + \gamma_n) \text{sinc}[\varepsilon f_0 \tan(\theta_n + \gamma_n)] \int_{T_n - \tau/2}^{T_n + \tau/2} \cos[2\pi f_0 [\rho_n r - \tilde{z}(T) \tan(\theta_n + \gamma_n) - \tilde{x}(T)]] \frac{dT}{\tau}. \quad (16)$$

Because the x-ray tube angle  $\psi$  remains constant during a single projection in a system with step-and-shoot motion, it is acceptable to simplify Eq. (8) by evaluating  $\theta(\psi)$ ,  $\gamma(\psi)$ , and  $\rho(\psi)$  at the nominal projection angle  $\psi = \psi_n$  as denoted by the parameters  $\theta_n$ ,  $\gamma_n$ , and  $\rho_n$ , respectively. Although the object coordinates  $\tilde{x}(\psi)$  and  $\tilde{z}(\psi)$  are dependent upon the x-ray tube angle  $\psi$  in a system with continuous tube motion, the same coordinates are now dependent upon time  $T$ . Consequently, the integral over  $\psi$  in Eq. (8) can be replaced by an integral over  $T$  to take into account the presence of

patient motion. The integration limits in Eq. (16) are thus the initial and final time points at which the tube emits x rays during a single projection, where  $T_n$  is the central time point of the projection of duration  $\tau$  and  $\Delta T$  is the time difference between consecutive projections. It can be shown that  $T_n = n(\tau + \Delta T)$  and  $\Delta T = (T_i - N\tau)/(N - 1)$ . Substituting the object coordinates  $\tilde{x}(T) = x_0 + vT \cos \zeta$  and  $\tilde{z}(T) = z_0 + vT \sin \zeta$  into Eq. (16) yields

$$\mathcal{A}\mu(n) = C\varepsilon \sec(\theta_n + \gamma_n) \text{sinc}[\varepsilon f_0 \tan(\theta_n + \gamma_n)] \text{sinc}\left[f_0 \tau v [\cos \zeta + \sin(\zeta) \tan(\theta_n + \gamma_n)]\right] \cdot \cos\left[2\pi f_0 [\rho_n r - (x_0 + vT_n \cos \zeta) - (z_0 + vT_n \sin \zeta) \tan(\theta_n + \gamma_n)]\right]. \quad (17)$$

By integrating  $\mathcal{A}\mu(n)$  over the detector element length  $a$  [Eq. (13)], the logarithmically-transformed signal in the  $m^{\text{th}}$  detector element for the  $n^{\text{th}}$  projection can be determined

$$\mathcal{D}\mu(m, n) = C\varepsilon \sec(\theta_{mn} + \gamma_n) \text{sinc}[\varepsilon f_0 \tan(\theta_{mn} + \gamma_n)] \text{sinc}\left[f_0 \tau v [\cos \zeta + \sin(\zeta) \tan(\theta_{mn} + \gamma_n)]\right] \text{sinc}[f_0 a \rho_{mn}] \cdot \cos\left[2\pi f_0 [ma \rho_{mn} - (x_0 + vT_n \cos \zeta) - (z_0 + vT_n \sin \zeta) \tan(\theta_{mn} + \gamma_n)]\right], \quad (18)$$

where  $\theta_{mn}$  and  $\rho_{mn}$  are calculated by evaluating  $\theta_n$  and  $\rho_n$  at  $r = ma$ .

#### 2.4 Filtered Backprojection (FBP) Reconstruction

The attenuation coefficient can now be reconstructed using filtered backprojection (FBP). From our previous work,<sup>5</sup> the FBP reconstruction for an infinitesimally fine (*i.e.*, non-pixelated) reconstruction grid is determined from the expression

$$\mu_{\text{FBP}}(x, z) = \frac{1}{N} \sum_m \sum_n \mathcal{D}\mu(m, n) \cdot \left[ \phi(t) * \text{rect}\left(\frac{t \sec \theta_{mn} - ma}{a}\right) \right]_{t=x \cos(\gamma_n + \theta_{mn}) + z \sin(\gamma_n + \theta_{mn})}, \quad (19)$$

where  $\mu_{\text{FBP}}$  is the reconstructed attenuation coefficient and  $*$  is the convolution operator. The reconstruction filter  $\phi(t)$  follows from linear systems theory for DBT. A ramp (RA) filter, given by  $|f|$  in the Fourier domain, is first applied to reduce the low frequency detector response. Since noise tends to occur at high frequencies, a spectrum apodization (SA) filter is also used; following Zhao's approach,<sup>3</sup> we apply a Hanning window function as the SA filter. In the Fourier domain, the filters are truncated at the frequencies  $f = \pm \zeta$ , and the net filter is the product of the RA and SA filters. As shown in our previous work,<sup>5</sup> the net filter can be calculated in closed form using the inverse Fourier transform.

### 3. RESULTS

Reconstructions are now simulated for a Selenia Dimensions system with 15 projections acquired at an angular spacing ( $\Delta\psi$ ) of  $1.07^\circ$ , assuming  $C = 1.0 \text{ mm}^{-1}$ ,  $h = 70.0 \text{ cm}$ ,  $\varepsilon = 0.50 \text{ mm}$ , and  $a = 140 \text{ }\mu\text{m}$ . At the x-ray tube angle  $\psi = 0$ , the centroid of the sine plate is taken to coincide with the midpoint of the chest wall side of a  $50.0 \text{ mm}$  thick breast. With the breast support positioned  $25.0 \text{ mm}$  above the origin of the detector, the  $x_0$  and  $z_0$  coordinates of the input object are therefore  $0$  and  $50.0 \text{ mm}$ , respectively.

#### 3.1 Effect of Continuous Tube Motion on Modulation

The effect of continuous tube motion on modulation is analyzed in Figure 3(a) by first simulating a system with no patient motion. For a  $30.0 \text{ ms}$  exposure time, corresponding to the mean value of  $\tau$  for the Selenia Dimensions system, reconstructions of the frequency  $2.0 \text{ lp/mm}$  are calculated. As expected, the modulation increases with scan time. For example, with scan times of  $2.0$ ,  $3.0$ , and  $4.0 \text{ s}$ , the modulation attains the values  $0.59$ ,  $0.70$ , and  $0.74$ , respectively. This trend arises because the tube's angular sweep  $\Psi$  during a single projection decreases with scan time [Eq. (2)].

For the same DBT system, the modulation in the reconstruction is also studied as a function of the input frequency  $f_0$  [Figure 3(c)]. At low frequencies, the modulation increases linearly from zero, following the ramp filter. At higher frequencies, the spectrum apodization filter and the MTF of the detector sampling process reduce the modulation, countering the ramp filter; hence, there is an intermediate frequency at which the modulation is maximized. This frequency dependence of the modulation matches Zhao's formulation of in-plane MTF in DBT reconstructions,<sup>3</sup> providing a built-in check on the validity of Figure 3(c). Like Zhao, we plot the modulation over a frequency range



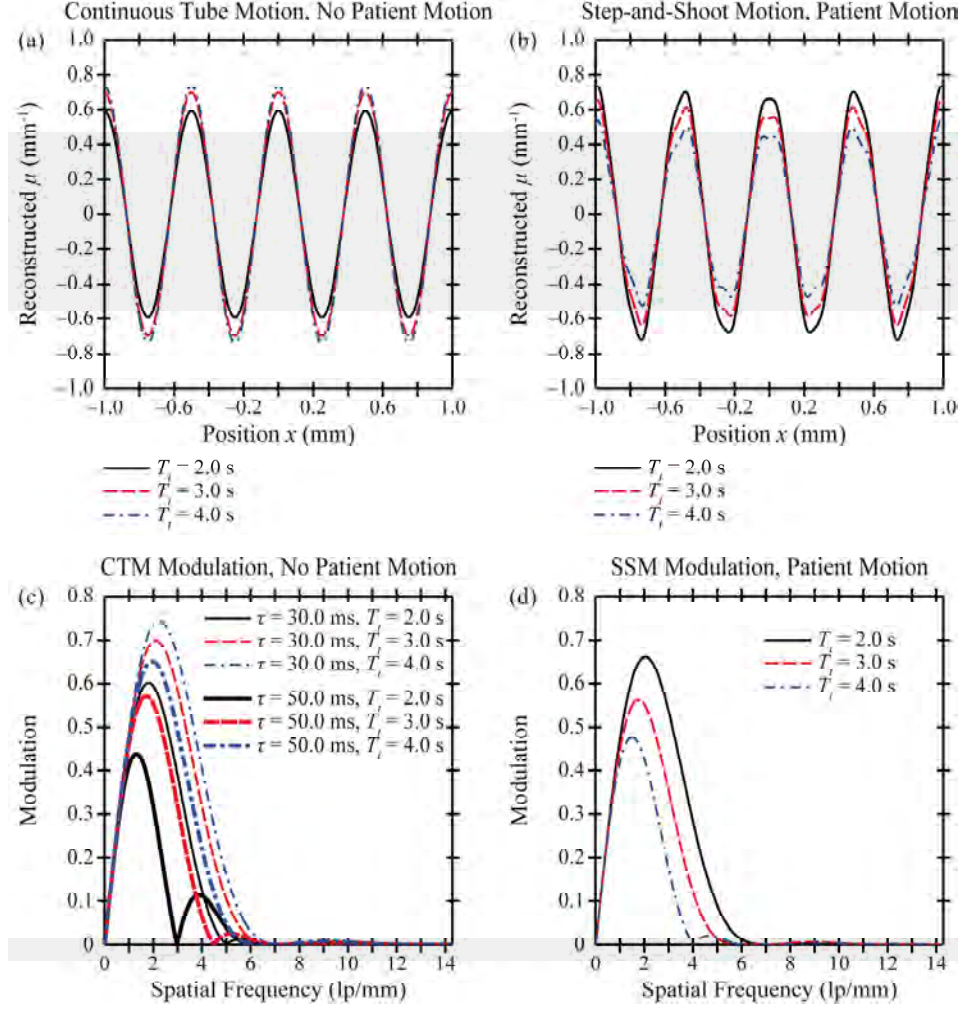


**Figure 3.** Although modulation increases with scan time in a system with continuous tube motion and no patient motion, the opposite trend holds in a system with step-and-shoot motion and patient motion.

spanning at least one zero of the MTF of the sampling process in the detector.<sup>7</sup> The filter truncation frequency ( $\xi$ ) of  $2a^{-1}$  (14.3 lp/mm) is simulated, corresponding to the second zero of the detector sampling MTF [ $\text{sinc}(af)$ ]. Figure 3(c) shows that increasing the scan time increases the modulation of the reconstruction, and thus generalizes the trend presented in Figure 3(a) to all frequencies. By contrast, increasing the exposure time decreases the modulation of the reconstruction.

In addition, Figure 3(c) demonstrates that the modulation of the reconstruction may possess zeros at frequencies different from those of the detector sampling MTF, whose first and second zero are  $a^{-1}$  (7.1 lp/mm) and  $2a^{-1}$  (14.3 lp/mm). Increasing the exposure time decreases these additional zeros, while increasing the scan time increases the zeros. For a 50.0 ms exposure time, the first zero not equivalent to  $a^{-1}$  or  $2a^{-1}$  is 3.0, 4.5, and 6.0 lp/mm for 2.0, 3.0, and 4.0 s scan times (5.0, 7.6, and 10.1 lp/mm for a 30.0 ms exposure time). The appendix shows that the formula for these zeros follows from the calculation of the MTF of focal spot motion. These zeros place an important limit on the resolution of the system.

### 3.2 Effect of Patient Motion on Modulation

In Figure 3(b), the effect of patient motion on modulation is investigated by considering a system with step-and-shoot motion. With an exposure time of 30.0 ms and an object velocity of 60.0  $\mu\text{m/s}$  oriented along the  $x$  direction, Figure 3(b) demonstrates that modulation decreases with scan time. The object velocity considered in Figure 3(b) is comparable to the value observed in Figure 1 showing clinical images of microcalcifications. The modulation attains the values 0.69,

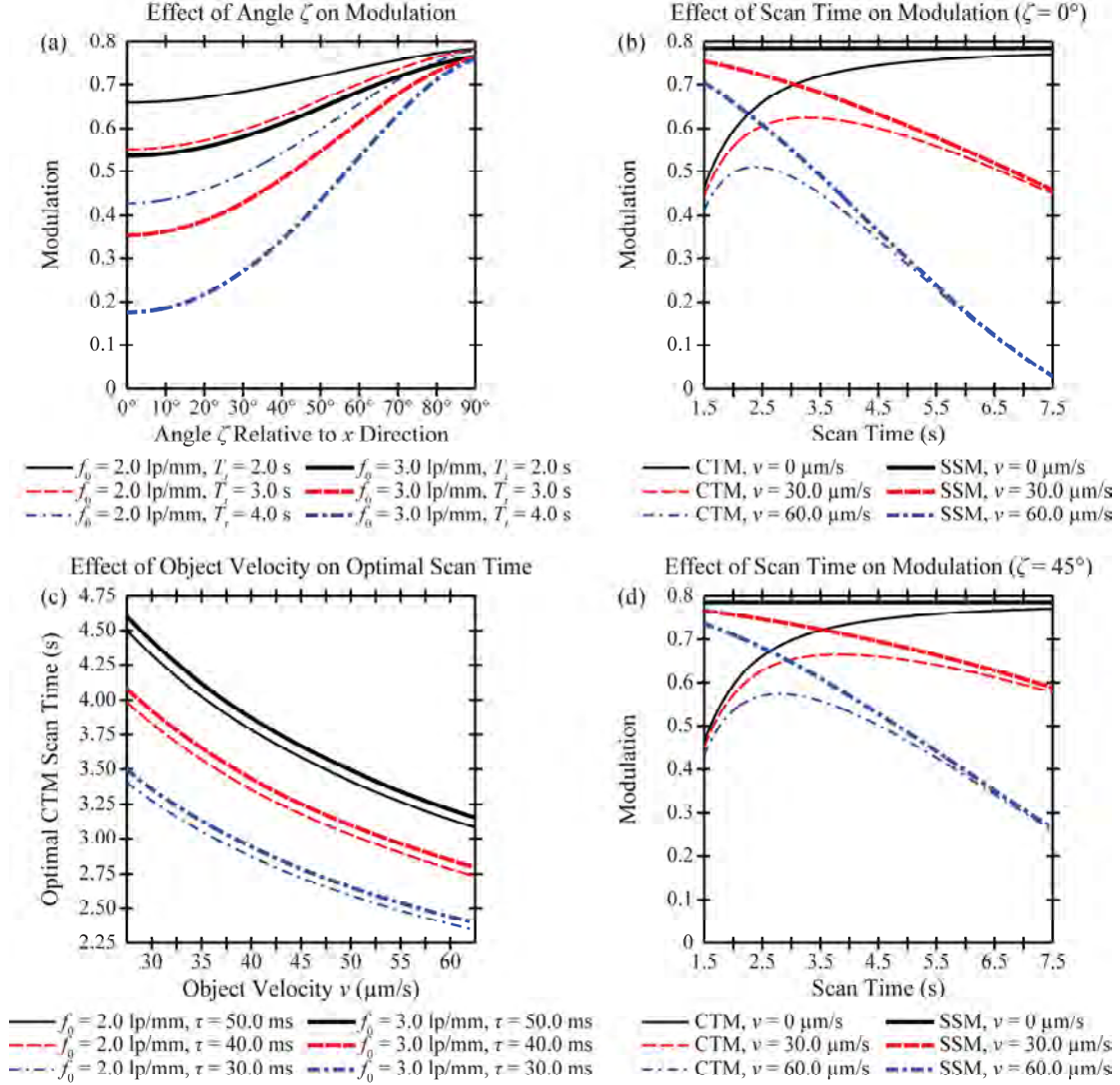


**Figure 4.** (a) By increasing the angle  $\zeta$  of patient motion relative to the  $x$  direction, the modulation of the reconstruction increases. (b) With continuous tube motion (CTM) and patient motion occurring simultaneously, modulation is optimized by an intermediate scan time. By contrast, modulation is maximized by a short scan time with step-and-shoot motion (SSM). (c) The dependency of the optimal CTM scan time on object velocity ( $v$ ), exposure time ( $\tau$ ), and frequency ( $f_0$ ) is investigated. (d) The optimal CTM scan time is larger with patient motion oriented at a  $45^\circ$  angle relative to the  $x$  direction than a  $0^\circ$  angle [Figure 4(b)].

0.61, and 0.52 for 2.0, 3.0, and 4.0 s scan times, respectively. This dependency of modulation on scan time is expected since the net displacement of the object in the  $x$  direction, given by  $vT_i\cos\zeta$ , increases with scan time.

In Figure 3(d), modulation is plotted versus  $f_0$  for a 30.0 ms exposure time. Figure 3(d) shows that the modulation decreases with scan time over all frequencies, thus generalizing the trend shown in Figure 3(c). Unlike a system with continuous tube motion and no patient motion, modulation varies minimally with exposure time in a system with step-and-shoot motion and patient motion. This finding arises because the object displacement between projections is significantly greater than the corresponding motion during the exposure time of an individual projection.

It is also demonstrated in Figure 3(d) that the frequency corresponding to the first zero of the modulation may be less than that of the detector sampling MTF. This zero follows from the point spread function (PSF) of patient motion, which is a rectangle function whose width is the object displacement during the scan time. Accordingly, the MTF of patient

motion is  $\text{sinc}(vT_f \cos \zeta)$ , and the first zero is  $(vT_f)^{-1} \text{sec} \zeta$ . With scan times of 2.0, 3.0, and 4.0 s, the zeros of the MTF of patient motion are 8.3, 5.6, and 4.2 lp/mm, respectively.

In the same system, Figure 4(a) studies the dependence of modulation on the directionality of patient motion. At any fixed frequency, the modulation increases with the angle  $\zeta$  relative to the  $x$  direction. In addition, the difference in modulation comparing any two scan times is minimized as  $\zeta$  increases. Modulation is virtually independent of scan time if the patient motion is oriented along the  $z$  direction ( $\zeta = 90^\circ$ ).

### 3.3 Optimization of Scan Time

With both continuous tube motion and patient motion occurring simultaneously, there is a trade-off in the benefits of long and short scan time, and hence modulation is maximized by an intermediate scan time [Figure 4(b)]. For example, with object velocities ( $v$ ) of 30.0 and 60.0  $\mu\text{m/s}$  oriented along the  $x$  direction, the optimal scan times for continuous tube motion are 3.3 and 2.4 s, respectively, assuming an input frequency of 2.0 lp/mm and an exposure time of 30.0 ms. Figure 4(c) demonstrates that this optimal scan time decreases with object velocity ( $v$ ) and increases with exposure time ( $\tau$ ). Exposure times between 30.0 ms (the mean value of the Selenia Dimensions system) and 50.0 ms (the maximum value of the system) are considered. Figure 4(c) also shows that the optimal scan time is frequency dependent.

For any fixed scan time, step-and-shoot motion (SSM) yields greater modulation than continuous tube motion (CTM). To optimize a step-and-shoot system, one may calculate the scan time giving the same modulation as the highest achievable with continuous tube motion [Figure 4(b)]. This scan time provides a threshold below which the use of step-and-shoot motion is justified. For example, with 30.0  $\mu\text{m/s}$  patient motion, an SSM scan time of 4.7 s yields the same modulation as the optimal CTM scan time of 3.3 s. With 60.0  $\mu\text{m/s}$  patient motion, the analogous SSM and CTM scan times are 3.3 and 2.4 s.

The dependence of the optimal CTM scan time on the directionality of patient motion is investigated in Figure 4(d) by considering patient motion along a  $45^\circ$  angle relative to the  $x$  direction. The optimal scan time for continuous tube motion is larger in Figure 4(d) than in Figure 4(b) with  $\zeta = 0^\circ$ . For example, with an object velocity ( $v$ ) of 30.0  $\mu\text{m/s}$ , the optimal CTM scan times for  $\zeta = 0^\circ$  and  $45^\circ$  are 3.3 and 3.8 s, respectively (2.4 and 2.8 s for  $v = 60.0 \mu\text{m/s}$ ). In addition, with  $\zeta = 45^\circ$ , there is a broader range of scan times for which the modulation is within the limit of resolution of the system, which is often taken to be 0.05. For example, with an object velocity of 60.0  $\mu\text{m/s}$  and a scan time of 7.5 s, the modulation with  $\zeta = 45^\circ$  is 0.26 (resolvable), yet the modulation with  $\zeta = 0^\circ$  is 0.03 (not resolvable).

## 4. DISCUSSION AND CONCLUSION

To our knowledge, this work is the first to model both continuous tube motion and patient motion in DBT, and as a result, to develop a technique which optimizes scan time. Continuous tube motion and patient motion have competing influences on scan time; we show that the modulation of the reconstruction is optimized by an intermediate scan time.

In Figure 4, it is demonstrated that continuous tube motion and step-and-shoot motion have nearly identical modulation in systems with very long scan time. For example, with a 2.0 lp/mm input and a 30.0 ms exposure time, one can show that the relative difference in modulation between the two systems does not exceed 1.0% for scan times of 10 s or more. This result holds regardless of the object velocity studied in Figure 4. For this reason, there is effectively no difference in image quality between the two systems if both operate at the same, very long scan time; patient motion is a much more significant cause of image quality degradation than continuous tube motion at these scan times.

To minimize patient motion in DBT, the system should have a short scan time comparable to 2D digital mammography. In systems with continuous tube motion, the drawback of lowering the scan time is substantially reducing the modulation relative to an analogous step-and-shoot system (Figure 4). Since systems with step-and-shoot motion tend to have longer scan times than those with continuous tube motion due to mechanical considerations, Figure 4 demonstrates that it is still possible to operate a system with continuous tube motion at a scan time yielding superior image quality relative to a step-and-shoot system. An additional benefit of continuous tube motion might include eliminating microphonic vibrations during the exposure time of each projection.

In conventional 2D digital mammography, it has been demonstrated that the scan time should be less than 2.0 s to minimize patient motion. Currently, no such guideline for DBT has been developed. In order to optimize scan time in systems with continuous tube motion, our simulations considered object velocities between 30.0 and 60.0  $\mu\text{m/s}$ . These velocities were chosen to be comparable to values seen in clinical images of microcalcifications presented in Figure 1. Although Figure 1 illustrates motion of microcalcifications in one clinical data set, the case is not necessarily representative of the most significant extent of patient motion, and thus additional cases should be considered in developing guidelines for scan time in DBT.

In systems with continuous tube motion, this paper demonstrates that the modulation of the reconstruction may be zero at frequencies smaller than the zeros of the MTF of detector sampling. This finding has important implications on the visibility of high frequencies in DBT, which was the subject of our prior work.<sup>5</sup> In performing reconstructions on a grid whose pixel size is much smaller than the detector elements, we have previously demonstrated that DBT is capable of super-resolution. Although the alias frequency of the Selenia Dimensions detector is 3.6 lp/mm, reconstructions of bar patterns have clearly shown higher frequencies due to super-resolution. In this paper, Figure 3(c) demonstrates that the ability to achieve super-resolution is influenced by focal spot motion, as the zeros of the modulation in a system with continuous tube motion vary with exposure time. A formula for these zeros is derived in the Appendix. Using high contrast bar patterns,<sup>5</sup> Figure 1 in our previous work demonstrated visibility of 6.0 lp/mm in the Selenia Dimensions system with a 3.7 s scan time and a 30.2 ms exposure time. For these settings, it follows from the Appendix that the modulation possesses a zero at 9.4 lp/mm. It is worth noting that if the same measurements were taken with the system's maximum exposure time of 50.0 ms, the limiting resolution of focal spot motion would be 5.6 lp/mm, and one would not expect the same 6.0 lp/mm bar patterns to be successfully resolved.

There has been recent interest in acquiring DBT images with less compression than conventional 2D mammography.<sup>8</sup> The purpose of the reduced compression is to spread out tissues and thus improve resolution in the  $z$  direction perpendicular to the breast support. This work argues against reduced compression, since it inherently leads to greater patient motion and would be expected to degrade the modulation of the reconstruction. In systems with long scan times, the need for full compression is particularly evident because the net object displacement should increase with scan time.

Some of the limitations of this study and directions for future modeling are now noted. Future work should more carefully model the MTF degradation due to non-normal x-ray incidence<sup>9,10</sup> as well as the finite size of the focal spot.<sup>11</sup> In addition, the presence of noise at various radiation dose levels could be simulated. Although this work implicitly assumes a high contrast input frequency whose visibility is independent of dose, future studies should demonstrate how the optimization of scan time is influenced by noise<sup>12</sup> at various dose levels for low contrast input frequencies. Because the attenuation coefficient of the input object is energy dependent, polyenergetic x-ray spectra should also be simulated. Furthermore, motion in the chest wall-to-nipple direction ( $y$ ) should be simulated in addition to the  $x$  and  $z$  directions (Figure 2). Finally, while this work considers a constant object velocity, there are instances in which the velocity is expected to be time-dependent. For example, the velocity may be sinusoidal with time in order to simulate the pulsatile motion of structures lying along blood vessels.

## 5. ACKNOWLEDGEMENT

The authors thank Baorui Ren (Hologic Inc., Bedford, MA) for useful background information on the acquisition geometry of the Selenia Dimensions DBT system. The project described was supported by a predoctoral training Grant No. W81XWH-11-1-0100 through the Department of Defense Breast Cancer Research Program. The content is solely the responsibility of the authors and does not necessarily represent the official views of the funding agency.

## 6. APPENDIX

This appendix calculates the MTF of the focal spot in a system with continuous x-ray tube motion by analyzing rays emanating from different focal spot positions during a single projection. For the  $n^{\text{th}}$  projection, rays are first drawn between the point  $(0, z_0)$  and the two endpoints of the tube arc. Subsequently, following Eq. (19), rays are backprojected toward the nominal projection angle  $\psi = \psi_n$ . The length  $b_n$  between backprojected rays at the height  $z = z_0$  in the reconstruction yields a rectangle function corresponding to the PSF of tube motion. The MTF of focal spot motion is

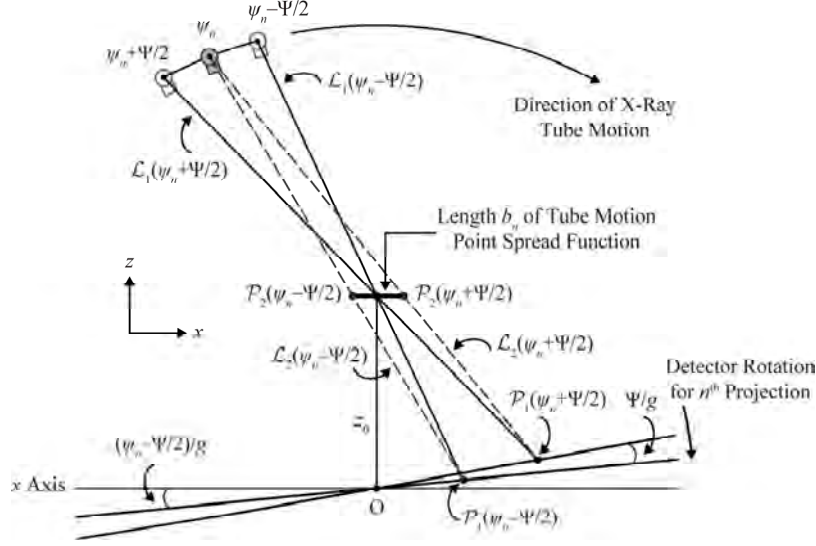


**Figure 5.** The point spread function (PSF) of focal spot motion is found by ray tracing.

then calculated from the Fourier transform of the PSF. To implement this approach, it is first necessary to determine the lines  $\mathcal{L}_1(\psi_n + \Psi/2)$  and  $\mathcal{L}_1(\psi_n - \Psi/2)$  between the point  $(0, z_0)$  and the endpoints of the x-ray tube arc at  $\psi = \psi_n + \Psi/2$  and  $\psi = \psi_n - \Psi/2$ . Since the focal spot coordinates are given by  $x = -h \sin(\psi_n \pm \Psi/2)$  and  $z = h \cos(\psi_n \pm \Psi/2)$ , the rays through the point  $(0, z_0)$  lie along the lines

$$\mathcal{L}_1(\psi_n \pm \Psi/2) = \{(x, z) : z = -[\cot(\psi_n \pm \Psi/2) - (z_0/h) \csc(\psi_n \pm \Psi/2)]x + z_0\}. \quad (\text{A1})$$

The lines  $\mathcal{L}_1(\psi_n + \Psi/2)$  and  $\mathcal{L}_1(\psi_n - \Psi/2)$  strike the detector at the points  $\mathcal{P}_1(\psi_n + \Psi/2)$  and  $\mathcal{P}_1(\psi_n - \Psi/2)$ , respectively

$$\mathcal{P}_1(\psi_n \pm \Psi/2) = \mathcal{L}_D[(\psi_n \pm \Psi/2)/g] \cap \mathcal{L}_1(\psi_n \pm \Psi/2), \quad \mathcal{L}_D[(\psi_n \pm \Psi/2)/g] = \{(x, z) : z = x \tan[(\psi_n \pm \Psi/2)/g]\} \quad (\text{A2})$$

where  $\mathcal{L}_D(\psi_n + \Psi/2)$  and  $\mathcal{L}_D(\psi_n - \Psi/2)$  are lines along the length of the detector at the x-ray tube angles  $\psi = \psi_n + \Psi/2$  and  $\psi = \psi_n - \Psi/2$ . Combining Eq. (A1) and (A2) gives

$$\mathcal{P}_1(\psi_n \pm \Psi/2) = (x, z) : x = z_0 \chi_n^\pm \tan(\psi_n \pm \Psi/2), \quad z = z_0 \chi_n^\pm \tan[(\psi_n \pm \Psi/2)/g] \tan(\psi_n \pm \Psi/2), \quad (\text{A3})$$

where

$$\chi_n^\pm = [1 + \tan[(\psi_n \pm \Psi/2)/g] \tan(\psi_n \pm \Psi/2) - (z_0/h) \sec(\psi_n \pm \Psi/2)]^{-1}. \quad (\text{A4})$$

Signal at the detector positions  $\mathcal{P}_1(\psi_n + \Psi/2)$  and  $\mathcal{P}_1(\psi_n - \Psi/2)$  is in turn backprojected to the focal spot at the x-ray tube angle  $\psi = \psi_n$ , forming the lines  $\mathcal{L}_2(\psi_n + \Psi/2)$  and  $\mathcal{L}_2(\psi_n - \Psi/2)$ .

$$\mathcal{L}_2(\psi_n \pm \Psi/2) = \left\{ (x, z) : z = \frac{-[h \cos \psi_n - z_0 \chi_n^\pm \tan[(\psi_n \pm \Psi/2)/g] \tan(\psi_n \pm \Psi/2)][x + h \sin \psi_n]}{h \sin \psi_n + z_0 \chi_n^\pm \tan(\psi_n \pm \Psi/2)} + h \cos \psi_n \right\} \quad (\text{A5})$$

At the reconstruction depth  $z = z_0$ , the lines  $\mathcal{L}_2(\psi_n + \Psi/2)$  and  $\mathcal{L}_2(\psi_n - \Psi/2)$  intercept the two points  $\mathcal{P}_2(\psi_n + \Psi/2)$  and  $\mathcal{P}_2(\psi_n - \Psi/2)$ .

$$\mathcal{P}_2(\psi_n \pm \Psi/2) = \mathcal{L}_2(\psi_n \pm \Psi/2) \cap \{(x, z) : z = z_0\} \quad (\text{A6})$$

$$= (x, z) : x = \frac{\left[ h \sin \psi_n + z_0 \chi_n^\pm \tan(\psi_n \pm \Psi/2) \right] \left[ h \cos \psi_n - z_0 \right]}{h \cos \psi_n - z_0 \chi_n^\pm \tan[(\psi_n \pm \Psi/2)/g] \tan(\psi_n \pm \Psi/2)} - h \sin \psi_n, \quad z = z_0 \quad (\text{A7})$$

A rectangle function of length  $b_n$  is created between  $\mathcal{P}_2(\psi_n + \Psi/2)$  and  $\mathcal{P}_2(\psi_n - \Psi/2)$ , thereby forming the effective PSF of the focal spot at the reconstruction depth  $z = z_0$  (Figure 5). Using MATLAB, one can show that  $b_n$  does not vary significantly with projection number  $n$  for the Selenia Dimensions system. Consequently, the special case  $n = 0$  is a useful approximation for the effective width of the PSF of focal spot motion in all projections.

$$b_0 = \frac{2z_0 \left(1 - \frac{z_0}{h}\right) \tan\left(\frac{\Psi}{2}\right)}{1 + \tan\left(\frac{\Psi}{2g}\right) \tan\left(\frac{\Psi}{2}\right) - \frac{z_0}{h} \left[ \sec\left(\frac{\Psi}{2}\right) + \tan\left(\frac{\Psi}{2g}\right) \tan\left(\frac{\Psi}{2}\right) \right]} \cong \frac{2z_0 \left(1 - \frac{z_0}{h}\right) \tan\left(\frac{\Psi}{2}\right)}{1 - \frac{z_0}{h} \sec\left(\frac{\Psi}{2}\right)} = \frac{2z_0 \left(1 - \frac{z_0}{h}\right) \tan\left[\left(\frac{N-1}{T_t - \tau}\right) \frac{\tau \Delta \psi}{2}\right]}{1 - \frac{z_0}{h} \sec\left[\left(\frac{N-1}{T_t - \tau}\right) \frac{\tau \Delta \psi}{2}\right]} \quad (\text{A8})$$

Since  $\Psi/2$  is well under  $1^\circ$  for typical acquisition geometries, one can use the approximation  $\tan[\Psi/(2g)] \tan(\Psi/2) \ll 1$  to derive this result. With the PSF of focal spot motion given by  $\text{rect}(x/b_0)$ , the MTF of focal spot motion is thus  $\text{sinc}(b_0 f)$ . The zeros of this MTF are integer multiples of  $1/b_0$ . This formula perfectly calculates the zeros of the modulation of the reconstruction in Figure 3(c) for a system with continuous tube motion and no patient motion.

## 7. REFERENCES

- <sup>1</sup>Rafferty EA. Tomosynthesis: New Weapon in Breast Cancer Fight. *Decisions in Imaging Economics*. 2004 April 2004;17(4).
- <sup>2</sup>Ren B, Ruth C, Stein J, Smith A, Shaw I, Jing Z. Design and performance of the prototype full field breast tomosynthesis system with selenium based flat panel detector. In: Flynn MJ, editor. *SPIE*; 2005; San Diego, CA: SPIE; 2005. p. 550-61.
- <sup>3</sup>Zhao B, Zhao W. Three-dimensional linear system analysis for breast tomosynthesis. *Medical Physics*. 2008;35(12):5219-32.
- <sup>4</sup>Bissonnette M, Hansroul M, Masson E, Savard S, Cadieux S, Warmoes P, et al. Digital breast tomosynthesis using an amorphous selenium flat panel detector. In: Flynn MJ, editor. *SPIE*; 2005; (SPIE, Bellingham, WA, 2005); 2005. p. 529-40.
- <sup>5</sup>Acciavatti RJ, Maidment ADA. Investigating the Potential for Super-Resolution in Digital Breast Tomosynthesis. In: Pelc NJ, Samei E, Nishikawa RM, editors. *SPIE*; 2011; Lake Buena Vista, FL: SPIE; 2011. p. 79615K-1 - K-12.
- <sup>6</sup>Lee DL, Cheung LK, Rodricks B, Powell GF. Improved imaging performance of a 14 x 17-inch Direct Radiography (TM) System using Se/TFT detector. *SPIE Conference on Physics of Medical Imaging*; 1998: SPIE; 1998. p. 14-23.
- <sup>7</sup>Albert M, Maidment ADA. Linear response theory for detectors consisting of discrete arrays. *Medical Physics*. 2000;27(10):2417-34.
- <sup>8</sup>Fornvik D, Andersson I, Svahn T, Timberg P, Zackrisson S, Tingberg A. The Effect of Reduced Breast Compression in Breast Tomosynthesis: Human Observer Study Using Clinical Cases. *Radiation Protection Dosimetry*. 2010;139(1-3):118-23.
- <sup>9</sup>Que W, Rowlands JA. X-ray imaging using amorphous selenium: Inherent spatial resolution. *Medical Physics*. 1995;22(4):365-74.
- <sup>10</sup>Hajdok G, Cunningham IA. Penalty on the detective quantum efficiency from off-axis incident x rays. In: Yaffe MJ, Flynn MJ, editors. *Medical Imaging 2004: Physics of Medical Imaging*; 2004; San Diego: SPIE; 2004. p. 109-18.
- <sup>11</sup>Johns HE, Cunningham JR. Chapter 16: Diagnostic Radiology. *The Physics of Radiology*. 4th ed. Springfield, IL: Charles C Thomas; 1983. p. 557-669.
- <sup>12</sup>Barrett HH, Myers KJ. Chapter 12: Noise in Detectors. In: Saleh BEA, editor. *Foundations of Image Science*. New York, NY: John Wiley & Sons; 2004. p. 701-800.